Monthly Notices of the ROYAL ASTRONOMICAL SOCIETY

MNRAS **450,** 815–845 (2015) doi:10.1093/mnras/stv420

Iron and *s*-elements abundance variations in NGC 5286: comparison with 'anomalous' globular clusters and Milky Way satellites

A. F. Marino,[1★] A. P. Milone,[1] A. I. Karakas,[1] L. Casagrande,[1] D. Yong,[1] L. Shingles,[1] G. Da Costa,[1] J. E. Norris,[1] P. B. Stetson,[2] K. Lind,[3] M. Asplund,[1] R. Collet,[1] H. Jerjen,[1] L. Sbordone,[4,5] A. Aparicio[6] and S. Cassisi[7]

[1] *Research School of Astronomy & Astrophysics, Australian National University, Mt Stromlo Observatory, via Cotter Rd, Weston, ACT 2611, Australia*
[2] *Herzberg Institute of Astrophysics, National Research Council Canada, 5071 West Saanich Road, Victoria, BC V9E 2E7, Canada*
[3] *Department of Physics and Astronomy, Division of Astronomy and Space Physics, Uppsala University, Box 515, SE-75120 Uppsala, Sweden*
[4] *Department of Electrical Engineering, Center for Astro-Engineering, Pontificia Universidad Católica de Chile, Av. Vicuña Mackenna 4860, 782-0436 Macul, Santiago, Chile*
[5] *The Milky Way Millennium Nucleus, Av. Vicuña Mackenna 4860, 782-0436 Macul, Santiago, Chile*
[6] *Instituto de Astrofísica de Canarias C/ Vía Láctea, s/n E-38205 La Laguna, Tenerife, Spain*
[7] *INAF-Osservatorio Astronomico di Teramo, via M. Maggini, I-64100 Teramo, Italy*

Accepted 2015 February 24. Received 2015 February 24; in original form 2014 November 6

ABSTRACT

We present a high-resolution spectroscopic analysis of 62 red giants in the Milky Way globular cluster (GC) NGC 5286. We have determined abundances of representative light proton-capture, α, Fe-peak and neutron-capture element groups, and combined them with photometry of multiple sequences observed along the colour–magnitude diagram. Our principal results are: (i) a broad, bimodal distribution in *s*-process element abundance ratios, with two main groups, the *s*-poor and *s*-rich groups; (ii) substantial star-to-star Fe variations, with the *s*-rich stars having higher Fe, e.g. $\langle[\mathrm{Fe/H}]\rangle_{s\text{-rich}} - \langle[\mathrm{Fe/H}]\rangle_{s\text{-poor}} \sim 0.2$ dex; and (iii) the presence of O–Na–Al (anti)correlations in both stellar groups. We have defined a new photometric index, $c_{BVI} = (B - V) - (V - I)$, to maximize the separation in the colour–magnitude diagram between the two stellar groups with different Fe and *s*-element content, and this index is not significantly affected by variations in light elements (such as the O–Na anticorrelation). The variations in the overall metallicity present in NGC 5286 add this object to the class of *anomalous* GCs. Furthermore, the chemical abundance pattern of NGC 5286 resembles that observed in some of the *anomalous* GCs, e.g. M 22, NGC 1851, M 2, and the more extreme ω Centauri, that also show internal variations in *s*-elements, and in light elements within stars with different Fe and *s*-elements content. In view of the common variations in *s*-elements, we propose the term *s*-Fe-*anomalous* GCs to describe this sub-class of objects. The similarities in chemical abundance ratios between these objects strongly suggest similar formation and evolution histories, possibly associated with an origin in tidally disrupted dwarf satellites.

Key words: stars: abundances – globular clusters: general – globular clusters: individual: NGC 5286.

1 INTRODUCTION

In recent years, an increasing number of observations have shattered the paradigm of globular clusters (GCs) as simple stellar population systems. When the first high-resolution spectroscopic data became available, it was immediately recognized that GCs host stars with different composition in proton (p) capture elements (see reviews by Kraft 1994; Gratton, Sneden & Carretta 2004). Later on, the advent of 8m-class telescopes with multi-object spectrographs enabled a substantial increase in statistics, from which it has become clear that stars with *non-field-like* abundances constitute a significant fraction of their parent clusters and they were observed along the whole colour–magnitude diagram (CMD; e.g. Cannon et al. 1998; Gratton et al. 2001; Marino et al. 2008; Carretta et al. 2009).

The most acknowledged scenario is that the chemical variations in p-capture elements are due to the presence of multiple stellar generations in GCs, with some being enriched in the products of

★ E-mail: amarino@mso.anu.edu.au

Published by Oxford University Press on behalf of the Royal Astronomical Society

high-temperature H-burning, such as Na and N. However, internal star-to-star variations in *p*-capture elements may be due to early disc accretion, rather than to the presence of multiple stellar generations (Bastian et al. 2013). In any case, this phenomenon to date, seems to be a typical feature of Galactic GCs. These features are also visible in the form of multiple sequences, mostly in the ultraviolet bands, on the GCs' CMDs, from the main sequence (MS) up to the red giant branch (RGB; e.g. Marino et al. 2008; Milone et al. 2012b).

For a long time, variations in the overall metallicity, here considered primarily as Fe, and/or in neutron (*n*) capture elements were considered a strict peculiarity of the most massive cluster ω Centauri (e.g. Norris & Da Costa 1995; Johnson & Pilachowski 2010; Marino et al. 2011a). For this reason, this object was associated with the nuclear remnant of a dwarf galaxy rather than with a real GC (e.g. Bekki & Freeman 2003; Bekki & Norris 2006). More recently, other objects with internal variations in metallicity have been identified, including M 22 (Da Costa et al. 2009; Marino et al. 2009). Interestingly, a clear bimodality in *slow* (*s*) *n*-capture elements was found in this GC, with *s*-CNO-enriched stars having a higher overall metallicity (Marino et al. 2009, 2011b; Alves-Brito et al. 2012; Roederer et al. 2011). Following the discovery of metallicity variations in M 22, the number of clusters known to have variations in metallicity has increased substantially, and now includes M 54 (Carretta et al. 2010b), Terzan 5 (Ferraro et al. 2009), M 2 (Yong et al. 2014), for which high-resolution spectroscopy is available, and NGC 5824 (Da Costa, Held & Saviane 2014), whose metallicities have been inferred from the Ca triplet analysis in low-resolution data. Among these GCs, chemical variations in *s*-process elements have been studied and confirmed, besides ω Centauri and M 22, in M 2 (Yong et al. 2014); while we are aware of C+N+O variations only in ω Centauri and M 22. A possible small metallicity spread, at the level of a few hundredths of dex, has been proposed also for NGC 1851 (Carretta et al. 2010a; Gratton et al. 2013; Marino et al. 2014), which also shows internal variations in the *s*-elements (Yong & Grundahl 2008; Villanova, Geisler & Piotto 2010) and in the overall C+N+O content (Yong et al. 2014). Although the presence of Fe variations in NGC 1851 needs further confirmation, enough evidence exists for it to be classified as a GC with chemical *anomalies* with respect to the bulk of Galactic GCs, such as the *s*-elements and C+N+O variations, that have been seen also in ω Centauri and M 22, but are not typically observed in Milky Way clusters. We therefore include NGC 1851 in the list of clusters with chemical *anomalies* with respect to the bulk of Galactic GCs.[1]

All these findings show that metallicity variations, which were thought to be an exclusive feature of ω Centauri, is actually a more widespread phenomenon in GCs. The degree of the observed metallicity variations varies from cluster to cluster, with ω Centauri and NGC 1851 being the extremes with the widest and lowest Fe spreads, respectively. It is tempting to speculate that these objects able to retain fast supernovae ejecta, were much more massive at their birth, and possibly nuclei of disrupted dwarf galaxies, as suggested for ω Centauri.

On the photometric side, these GCs show some *peculiarities*, not observed in the other clusters. The CMD of ω Centauri is the most complex ever observed for a GC, with multiple sequences along all the evolutionary stages, from the MS to a well-extended multimodal horizontal branch (HB), through a complex multiple sub-giant branch (SGB, e.g. Bellini et al. 2010). However, while the presence of multiple MSs and RGBs in UV bands, as well as in some cases extended HBs, are in general good proxies for variations in light elements (including He for the HB; see Milone et al. 2014), multiple SGBs are observed in many of the clusters with Fe variations, in all photometric bands (e.g. Milone et al. 2008; Piotto et al. 2012). Theoretically, multiple SGBs may reflect differences in the overall metallicity and/or C+N+O and/or age (Cassisi et al. 2008; Marino et al. 2011b, 2012). Two notable examples in this respect are the double SGBs of NGC 1851 (Milone et al. 2008) and M22 (e.g. Marino et al. 2009, 2012; Piotto et al. 2012). Like M 22, NGC 1851 has a bimodal distribution in the *s*-process elements (Yong & Grundahl 2008; Carretta et al. 2010a; Villanova et al. 2010), and some evidence of variations in the total CNO have been provided by Yong et al. (2009, 2014). Complex SGB morphologies are present also in M 54 and M 2, with the latter exhibiting a triple SGB (Piotto et al. 2012; Milone et al. 2015).

To date metallicity variations are observed in eight Galactic GCs, over the ∼30 GCs where Fe abundances are available for relatively large samples of stars. Note that the true fraction of these objects in the Milky Way is likely lower as many recent spectroscopic observations are biased because they were aimed at the study of these objects previously identified from photometry. Despite the number of the GCs with variations in Fe is expected to increase, these objects still constitute a minor component with respect to monometallic GCs. The chemical properties of these objects can be regarded as *anomalies* with respect to the bulk of GCs in the Milky Way, indeed we refer to these objects as *anomalous* GCs. The term *anomalous* will be primarily used to indicate the objects with internal metallicity variation, which on different levels is shared by all these objects.

In this study, we further explore the properties of *anomalous* GCs, the plausibility to identify a further class of objects where Fe variations are accompanied by variations in *s*-elements, and the possibility that a split SGB in a GC constitutes a proxy for its chemical *anomaly*, e.g. internal variations in overall metallicity, heavy elements including slow *n*-capture elements (*s*-elements), and C+N+O. Our aims are to trace how frequent these *anomalous* objects occur in the Milky Way, and to try to disclose their possible formation and early evolution. A fundamental step to this goal is to understand if they constitute a separate class of objects from typical Galactic GCs, originated in a different way; or they simply form as typical *normal* GCs and their chemical anomalies are due to more advanced stages of evolution. The *s*-process enrichment due to low-mass AGB needs some hundreds Myrs to occur; and at the time this enrichment starts to be effective, the Fe-enriched material from supernovae, previously expelled from the cluster, may fall-back into the GC potential well and contribute to the formation of a new stellar generation (e.g. D'Antona et al. 2011 for ω Centauri).

In this paper, we focus on the chemical abundances for a poorly studied GC: NGC 5286. *HST* photometry has demonstrated that this GC shows a split SGB, similar to those observed in NGC 1851 and M 22. In this case, however, the stellar component on the fainter SGB constitutes only ∼14 per cent of the total mass of the cluster, which is significantly lower than in M 22 and NGC 1851 (fainter SGB stars in these GCs account for the ∼38 per cent and ∼35 per cent, respectively; Piotto et al. 2012), but larger than in M 2, where its two faint SGB components account for ∼3 per cent and ∼1 per cent of all the SGB stars (Milone et al. 2015).

[1] We note that iron variations have been found in NGC 3201 by Simmerer et al. (2013), but such evidence is not present in Carretta et al. (2010a) nor in Muñoz, Geisler & Villanova (2013). Specifically, Muñoz et al. (2013) did not detect any spread in the *s*-elements, as that found in other GCs with Fe variations. At the moment, we do not include this object in our list of *anomalous* GCs.

2 DATA

With a mass of $M = 10^{5.65}$ $M_{\odot}$ (McLaughlin & van der Marel 2005), and an absolute visual magnitude of $M_V = -8.74$, as listed in the Harris catalogue (Harris 1996, updated as in 2010), NGC 5286 is a relatively massive GC (as a comparison, M 22 has $M_V = -8.50$, NGC 1851 $M_V = -8.33$ and M 2 $M_V = -9.03$). This GC lies at a distance of 8.9 kpc from the Galactic Centre and 11.7 kpc from the Sun, and it is affected by relatively high foreground reddening, with a mean value of $E(B - V) = 0.24$ (Harris 2010). NGC 5286 shows a blue HB, more than a dozen RR Lyrae variables (e.g. Clement et al. 2001), whose periods are consistent with an Oosterhoff II type (Zorotovic et al. 2010). In this section, we consider in turn the photometric and spectroscopic data that we have employed in this study.

2.1 The photometric data set: multiple populations along the SGB/RGB of NGC 5286

We used photometric data from the Wide Field Imager (WFI) of the Max Planck 2.2m telescope at La Silla collected through the *U* filter under the SUrvey of Multiple pOpulations in GCs (SUMO; programme 088.A-9012-A, PI. A. F. Marino). These *U* images consist of 14 × 850 s+3 × 300 s collected on 2012 February. Additionally, we have used *B*, *V*, and *I* photometry from the archive maintained by P. B. Stetson (Stetson 2000). A journal of all the observations is shown in Table 1. In Fig. 1, we plot a *V* versus $(B - I)$ CMD and the location of stars in an ∼21 arcmin ×21 arcmin field of view around NGC 5286; our spectroscopic UVES and GIRAFFE targets have been marked in black and orange, respectively.

BVI photometry has been used to determine atmospheric parameters, as discussed in Section 3. As the *U* filter is very efficient to identify multiple stellar populations along the RGB (Marino et al. 2008), we used *U* data from our SUMO programme to investigate the connection between multiple sequences in the CMD and the chemical composition. The photometric and astrometric reduction of WFI data has been carried out by using the software and the procedure described by Anderson et al. (2006). To calibrate the magnitudes in the *U* Johnson, we have matched our photometry with the catalogue of photometric secondary standards by Stetson (2000) and derived calibration equation by using least-squares fitting of straight lines of stellar magnitudes and colours.

Very accurate photometry is crucial to identify different sequences along the CMD for the analysis of multiple stellar populations. To this aim, we have followed the recipe by Milone et al. (2009, Section 2.1) and selected a sample of stars with small astrometric and photometric errors, which are well fitted by the point spread function, and relatively isolated. Our photometry has been also corrected for differential reddening as in Milone et al. (2012a).

For NGC 5286, the analysis of the CMD is affected by strong contamination from background/foreground field stars clearly visible in Fig. 1. Milone et al. (2012a, see their fig. 12) have shown that the average proper motion of this GC differs from the motion of most of the field stars. Therefore, we have used proper motions to separate most of the field stars from cluster members. Briefly, we have estimated the displacement between the stellar positions measured from WFI data and those in the catalogue by Stetson (2000) by using the method described in Anderson & King (2003; see also Bedin et al. 2006; Anderson & van der Marel 2010). Results of our proper motions analysis are illustrated in Fig. 2: the left-hand panel shows the *V* versus $(B - I)$ CMD of all the stars with radial distance from the cluster centre smaller than 4.3 arcmin that pass our photometric criteria of selection; the right-hand panels display the vector-point diagrams (VPDs) of the stellar displacement for stars in five luminosity intervals. Since we have calculated relative proper motions with respect to a sample of cluster members, the bulk of stars around the origin of the VPD is mostly made of NGC 5286 stars, while field objects have clearly different motion. The red circles have been drawn by eye and are used to separate probable cluster members (black points) from the most evident field stars (grey crosses).

The probable cluster members, selected by proper motions, have been plotted in the *V* versus $(B - I)$ and *U* versus $(U - V)$ CMDs with black dots in Fig. 2, while field stars with grey dots. Our *U* versus $(U - V)$ CMD shows a complex SGB *evolving* into a spread/double RGB. For a clearer visualization of the two SGBs and RGBs in the *U* versus $(U - V)$ CMD refer to Fig. 13, that provides the first evidence for a double RGB in the U–$(U - V)$ CMD for NGC 5286. This intriguing double RGB feature has only been found in a handful of objects observed in the SUMO programme. In the next section, we describe the investigation of the chemical composition of these two sequences using FLAMES data. We also note that on this diagram the AGB sequence is clearly separated from the RGB.

2.2 The spectroscopic data set

Our spectroscopic data consist of FLAMES/GIRAFFE and FLAMES/UVES spectra (Pasquini et al. 2002) observed under the programme 091.D-0578(A) (PI: A. F. Marino). The high-resolution HR13 GIRAFFE setup was employed, which covers a spectral range of ∼300 Å from ∼6 122 Å to ∼6402 Å, and provides a resolving power $R \equiv \lambda/\Delta\lambda \sim 22{,}000$. The higher resolution fibres available for UVES provided spectra with a larger wavelength coverage from ∼4800 Å to ∼6800 Å, with a resolution of ∼45 000.

In total, we gathered spectra for 87 GIRAFFE plus seven UVES stars, represented in Fig. 1. Our targets have been carefully selected to sample both RGBs of NGC 5286 that we have found from the analysis of the CMD, as discussed in Section 2.1. Most of the targets are RGB stars of NGC 5286 with $14 \lesssim V \lesssim 16.5$, with some AGB and field stars, and were observed in the same FLAMES plate in 11 different exposures of 46 min. The UVES targets span a smaller range in magnitude, around $V \sim 15$ mag. The typical S/N of the fully reduced and combined GIRAFFE spectra ranges from ∼80 to ∼200 at the central wavelength, depending on the brightness of the stars; the UVES final spectra have an S/N around ∼70 per pixel at the Na doublet at ∼6160 Å; the most luminous UVES star (#859U) has S/N ∼ 150 at the same wavelength.

Table 1. Description of the photometric images used in this work.

Telescope	Detector	U	B	V	I	Date
CTIO 0.9m	RCA	–	8	8	–	1987 Jan 21–24
CTIO 0.9m	$Tek2K_3$	–	–	10	10	1996 Apr 16–19
CTIO 0.9m	$Tek2K_3$	–	24	27	–	1998 May–2004 Jun 26
CTIO 0.9m	$Tek2K_3$	–	2	2	2	1999 Jun 13
CTIO 0.9m	$Tek2K_3$	–	1	1	1	2001 Mar 25
MPI/ESO 2.2m	WFI	–	4	4	10	2002 Feb 20
ESO NTT 3.6m	SUSI	–	–	4	0	2003 May 30
CTIO 0.9m	$Tek2K_3$	–	–	2	–	2007 Jun 22
SOAR 4.1m	SOI	–	65	63	61	2008 Feb 12–18
MPI/ESO 2.2m[a]	WFI	17	–	–	–	2012 Feb 26

Note. [a]SUMO project: programme 088.A9012(A).

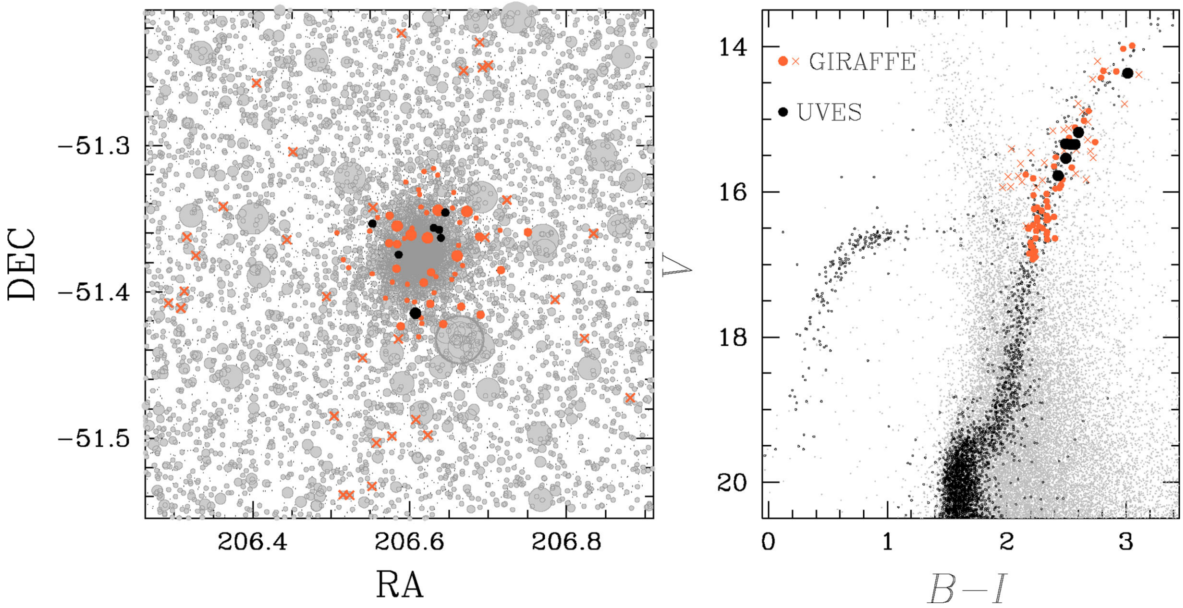

Figure 1. Left-hand panel: location of the spectroscopic targets in RA and DEC. The NGC 5286 spectroscopic targets have been plotted in orange (GIRAFFE) and black (UVES). For GIRAFFE stars, we used different symbols for bona fide cluster stars (dots) and field stars (crosses). Right-hand panel: V–($B-I$) CMD of NGC 5286 proper-motions members (black) and field stars (grey). The position of the spectroscopic GIRAFFE and UVES targets on the CMD is shown by using the same symbols as on the left-hand panel.

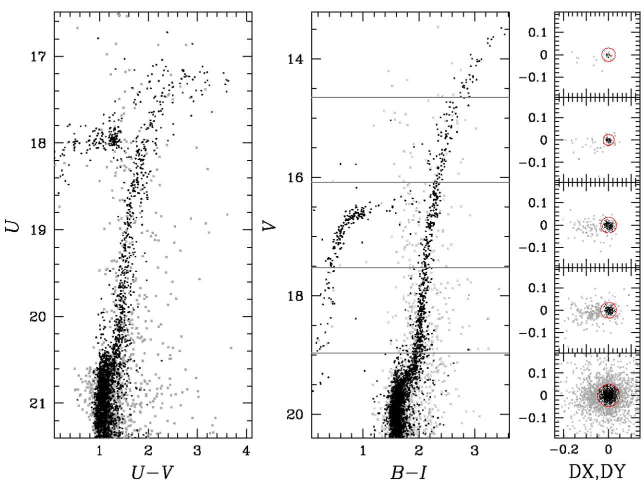

Figure 2. U versus ($U-V$) (left-hand panel) and V versus ($B-I$) CMD (middle panel) of stars in the field of view of NGC 5286 corrected for differential reddening. Right panels show the VPDs of stellar displacement in the five intervals of V magnitude indicated by the horizontal lines in the middle-panel CMD. The red circles separate probable cluster members and field stars, which have been represented with black dots and grey crosses, respectively, in all the panels of this figure.

Data reduction involving bias-subtraction, flat-field correction, wavelength-calibration, sky-subtraction, has been done by using the dedicated pipelines.[2] Radial velocities (RVs) were derived using the IRAF@FXCOR task, which cross-correlates the object spectrum with a template. For the template, we used a synthetic spectrum obtained through the 2014 March version of MOOG (Sneden 1973). This spectrum was computed with a stellar model atmosphere interpolated from the Castelli & Kurucz (2004) grid, adopting parameters ($T_{\rm eff}$, log g, $\xi_{\rm t}$, [Fe/H]) = (4500 K, 2.5, 2.0 km s^{-1}, −1.80). Observed RVs were then corrected to the heliocentric system. Heliocentric RVs were used as a membership criterion for our GIRAFFE targets, together with the proper motion selection (see Section 2.1). First, we selected the stars having velocities in the range between 40 and 100 km s^{-1}, that is where the major peak in the RV distribution appears; then we considered the stars within 2×σ (where σ has been estimated as the 68.27th percentile of the RV distribution) around the median value of this selected sample as probable cluster members. At the end, our GIRAFFE sample of probable NGC 5286 stars is composed by 55 stars, whose median RV is 61.5 ± 1.1 km s^{-1}(rms = 7.8 km s^{-1}), which is in reasonable agreement with the value reported in the Harris catalogue, 57.4 ± 1.5 km s^{-1} (rms = 8.1 km s^{-1}). The seven stars observed with UVES have mean RV 65.6 ± 1.3 km s^{-1} (rms = 3.1 km s^{-1}) and were all considered members of NGC 5286. Among the bona fide GC stars, two GIRAFFE targets lie on the AGB sequence visible on the U–($U-V$) CMD. Coordinates, basic BV photometry and RVs for the all the stars observed with GIRAFFE and UVES are listed in Table 2. Only cluster members, selected on the basis of proper motions and RVs have been included in the following analysis.

3 MODEL ATMOSPHERES

Given the different resolution and spectral coverage of our GIRAFFE and UVES data, we decided to estimate stellar atmospheric parameters using different techniques. For the GIRAFFE spectra, given the relatively low number of Fe lines, we rely on the photometric information to derive effective temperatures ($T_{\rm eff}$), surface gravities (log g), and microturbulent velocities ($\xi_{\rm t}$). On the other hand, for UVES data we derive atmospheric parameters by using a standard fully spectroscopic approach, independent of the photometry. Details on the estimate of stellar parameters for both sets of spectra are presented below.

[2] See http://girbld-rs.sourceforge.net.

Table 2. Coordinates, basic photometric data and RVs for the stars in the field of view of NGC 5286. The status of probable cluster members is listed in the last column. We list both the original magnitudes ($BVI_{\rm ori}$) and those corrected for differential reddening ($BVI_{\rm cor}$).

ID	RA (J2000)	DEC (J2000)	$B_{\rm ori}$	$V_{\rm ori}$	$I_{\rm ori}$	$B_{\rm cor}$	$V_{\rm cor}$	$I_{\rm cor}$	RV (km s^{-1})	
					UVES					
N5286-1219U	13:46:31.38	−51:21:22.8	16.532	15.347	13.959	16.495	15.319	13.943	66.99	member
N5286-1439U	13:46:34.90	−51:20:45.6	16.917	15.781	14.485	16.977	15.827	14.512	70.18	member
N5286-859U	13:46:25.75	−51:24:53.0	15.850	14.369	12.836	15.801	14.331	12.814	60.76	member
N5286-1309U	13:46:32.99	−51:21:27.4	16.482	15.338	13.988	16.526	15.372	14.008	62.91	member
N5286-579U	13:46:20.65	−51:22:28.8	16.511	15.348	13.975	16.548	15.376	13.992	64.94	member
N5286-1339U	13:46:33.58	−51:21:47.3	16.716	15.539	14.221	16.751	15.566	14.237	66.82	member
N5286-177U	13:46:12.62	−51:21:12.6	16.373	15.183	13.771	16.364	15.177	13.767	66.44	member
					GIRAFFE					
N5286-667G	13:46:22.38	−51:21:48.6	17.849	16.853	15.644	17.875	16.873	15.656	66.92	member
N5286-527G	13:46:20.17	−51:21:18.3	15.802	14.351	12.769	15.702	14.274	12.724	66.03	member
N5286-1117G	13:46:29.51	−51:21:47.3	15.739	14.429	12.948	15.767	14.450	12.961	66.33	member
N5286-757G	13:46:24.45	−51:21:40.5	15.464	14.031	12.486	15.474	14.039	12.491	64.24	member
N5286-697G	13:46:22.81	−51:19:30.4	17.222	16.218	14.967	17.303	16.280	15.004	64.19	member
N5286-779G	13:46:24.76	−51:21:23.7	17.750	16.657	15.411	17.714	16.630	15.395	64.90	member
N5286-399G	13:46:17.89	−51:20:52.8	17.084	15.957	14.677	17.067	15.944	14.669	65.99	member
N5286-989G	13:46:27.47	−51:20:31.9	17.947	16.928	15.731	18.033	16.994	15.770	69.79	member
N5286-189G	13:46:12.85	−51:20:33.2	15.562	14.203	12.798	15.523	14.173	12.780	− 30.47	field
N5286-1297G	13:46:32.73	−51:20:39.6	15.443	13.988	12.392	15.477	14.014	12.407	53.48	member
N5286-1767G	13:46:51.63	−51:21:29.0	17.640	16.637	15.397	17.693	16.678	15.421	59.91	member
N5286-1269G	13:46:32.59	−51:19:12.8	17.526	16.480	15.253	17.651	16.576	15.309	60.64	member
N5286-939G	13:46:26.78	−51:19:48.8	17.561	16.541	15.315	17.706	16.652	15.380	67.52	member
N5286-1197G	13:46:31.29	−51:18:56.6	17.675	16.699	15.474	17.755	16.760	15.510	58.44	member
N5286-1057G	13:46:28.42	−51:19:04.1	17.032	16.048	14.808	17.131	16.124	14.853	70.26	member
N5286-5101G	13:46:21.47	−51:13:24.5	16.903	15.862	14.774	–	–	–	− 13.87	field
N5286-5361G	13:46:47.08	−51:21:46.5	16.353	15.038	13.670	16.406	15.079	13.694	− 80.06	field
N5286-5381G	13:46:48.10	−51:14:42.9	16.134	14.899	13.496	–	–	–	− 14.66	field
N5286-1547G	13:46:37.49	−51:19:55.8	17.084	16.030	14.749	17.215	16.131	14.808	70.48	member
N5286-1077G	13:46:29.15	−51:20:45.6	17.370	16.356	15.115	17.423	16.397	15.139	73.63	member
N5286-5351G	13:46:46.24	−51:14:48.7	16.036	14.784	13.439	–	–	–	12.27	field
N5286-5321G	13:46:45.45	−51:13:46.5	16.781	15.443	14.078	–	–	–	− 8.54	field
N5286-5271G	13:46:40.51	−51:14:56.7	17.097	15.833	14.431	–	–	–	− 42.63	field
N5286-5441G	13:46:51.91	−51:23:06.8	16.801	15.817	14.581	16.795	15.812	14.578	58.93	member
N5286-1607G	13:46:39.34	−51:21:09.5	17.494	16.510	15.312	17.594	16.587	15.357	49.77	member
N5286-969G	13:46:27.12	−51:20:00.5	17.779	16.763	15.560	17.917	16.869	15.622	54.50	member
N5286-5481G	13:46:53.75	−51:20:14.3	16.371	15.147	13.774	16.448	15.206	13.809	8.90	field
N5286-1729G	13:46:44.30	−51:20:58.5	17.306	16.207	14.962	17.495	16.352	15.047	63.07	member
N5286-1687G	13:46:41.45	−51:20:42.5	15.664	14.335	12.853	15.852	14.479	12.937	69.04	member
N5286-5541G	13:47:00.17	−51:21:33.6	16.136	14.888	13.449	16.152	14.901	13.456	56.74	member
N5286-1737G	13:46:45.20	−51:21:44.7	16.409	15.258	13.886	16.476	15.309	13.916	58.42	member
N5286-1537G	13:46:37.10	−51:20:34.7	17.240	16.234	15.010	17.401	16.357	15.082	71.15	member
N5286-5631G	13:47:08.45	−51:24:19.6	16.963	15.748	14.384	–	–	–	− 23.20	field
N5286-5191G	13:46:30.30	−51:24:29.8	16.710	15.763	14.550	16.715	15.767	14.552	49.95	member
N5286-1567G	13:46:38.52	−51:22:31.8	15.716	14.343	12.799	15.753	14.371	12.816	69.87	member
N5286-1147G	13:46:30.56	−51:23:12.2	16.297	15.113	13.725	16.361	15.162	13.754	73.95	member
N5286-5741G	13:47:20.28	−51:21:36.9	16.899	15.930	14.868	–	–	–	9.23	field
N5286-1659G	13:46:40.20	−51:22:55.4	17.464	16.391	15.132	17.459	16.387	15.130	59.41	member
N5286-1047G	13:46:28.31	−51:23:37.5	16.620	15.525	14.209	16.638	15.539	14.217	49.05	member
N5286-1557G	13:46:37.83	−51:23:16.6	17.861	16.866	15.642	17.905	16.900	15.662	57.97	member
N5286-1227G	13:46:31.48	−51:24:02.4	17.475	16.492	15.287	17.576	16.570	15.333	59.51	member
N5286-1599G	13:46:38.96	−51:22:05.6	17.407	16.326	15.072	17.416	16.333	15.076	63.15	member
N5286-1369G	13:46:34.30	−51:25:19.5	16.876	15.665	14.331	16.873	15.663	14.330	68.30	member
N5286-5861G	13:47:31.49	−51:28:20.0	16.637	15.599	14.322	–	–	–	− 24.01	field
N5286-1529G	13:46:36.88	−51:23:30.1	17.927	16.897	15.687	17.977	16.935	15.709	64.49	member
N5286-947G	13:46:26.79	−51:25:50.4	17.436	16.388	15.093	17.420	16.376	15.086	53.75	member
N5286-1237G	13:46:32.06	−51:23:23.0	17.452	16.460	15.230	17.517	16.510	15.259	63.43	member
N5286-827G	13:46:25.50	−51:24:25.3	17.820	16.853	15.632	17.885	16.903	15.661	61.60	member
N5286-1017G	13:46:27.72	−51:25:18.1	17.415	16.400	15.161	17.403	16.391	15.156	57.18	member
N5286-1747G	13:46:45.70	−51:24:56.6	16.951	15.833	14.483	16.790	15.710	14.411	60.59	member
N5286-996G	13:46:27.52	−51:25:04.1	17.181	16.129	14.848	17.167	16.118	14.842	64.46	member
N5286-1649G	13:46:39.79	−51:24:36.4	16.273	15.020	13.625	16.130	14.911	13.561	59.05	member
N5286-5021G	13:46:18.65	−51:29:54.6	16.336	15.406	14.295	–	–	–	16.00	field
N5286-5151G	13:46:25.95	−51:29:14.5	16.979	15.940	14.729	–	–	–	− 21.11	field

Table 2 – *continued*

ID	RA (J2000)	DEC (J2000)	B_{ori}	V_{ori}	I_{ori}	B_{cor}	V_{cor}	I_{cor}	RV (km s^{-1})	
N5286-5181G	13:46:29.58	−51:29:52.3	16.899	15.843	14.601	–	–	–	− 5.34	field
N5286-4911G	13:46:09.55	−51:26:42.9	16.636	15.420	14.052	16.343	15.195	13.920	− 19.57	field
N5286-587G	13:46:21.29	−51:25:24.9	16.599	15.316	13.858	16.354	15.127	13.748	51.23	member
N5286-4861G	13:46:05.64	−51:32:20.8	16.545	15.611	14.429	–	–	–	24.10	field
N5286-559G	13:46:20.52	−51:25:55.9	17.469	16.472	15.310	17.248	16.302	15.211	− 25.53	field
N5286-4941G	13:46:12.46	−51:31:57.9	16.907	15.866	14.456	–	–	–	335.72	field
N5286-29G	13:46:05.34	−51:23:00.6	17.739	16.640	15.334	17.642	16.565	15.290	59.30	member
N5286-437G	13:46:18.73	−51:23:36.2	17.538	16.503	15.236	17.468	16.449	15.205	57.07	member
N5286-17G	13:46:03.77	−51:22:41.2	17.420	16.370	15.070	17.339	16.308	15.034	60.02	member
N5286-4961G	13:46:13.81	−51:30:11.3	15.636	14.335	12.810	–	–	–	− 56.40	field
N5286-719G	13:46:23.29	−51:23:41.6	17.467	16.345	15.069	17.449	16.331	15.061	57.67	member
N5286-4831G	13:46:03.63	−51:32:19.4	16.519	15.466	14.317	–	–	–	39.38	member
N5286-169G	13:46:12.54	−51:23:16.0	17.654	16.587	15.318	17.645	16.580	15.314	50.96	member
N5286-4811G	13:46:00.98	−51:29:06.1	16.183	14.793	13.194	–	–	–	234.39	field
N5286-07G	13:46:01.77	−51:21:34.8	17.286	16.262	14.992	17.286	16.262	14.992	61.53	member
N5286-289G	13:46:16.63	−51:24:16.0	17.635	16.555	15.298	17.525	16.471	15.249	52.09	member
N5286-4791G	13:45:58.57	−51:24:12.4	16.572	15.286	13.895	16.421	15.170	13.827	− 20.38	field
N5286-379G	13:46:17.74	−51:22:00.7	17.058	15.911	14.604	17.045	15.901	14.598	70.88	member
N5286-509G	13:46:19.99	−51:23:03.2	17.088	15.948	14.647	17.101	15.958	14.653	53.47	member
N5286-4241G	13:45:14.10	−51:24:40.0	15.729	14.449	13.010	–	–	–	− 11.84	field
N5286-157G	13:46:11.80	−51:21:31.0	17.813	16.820	15.576	17.772	16.788	15.558	75.22	member
N5286-4641G	13:45:46.42	−51:21:52.5	16.322	15.149	13.842	–	–	–	− 72.41	field
N5286-707G	13:46:23.20	−51:24:21.4	17.734	16.752	15.528	17.731	16.750	15.527	60.30	member
N5286-537G	13:46:20.17	−51:22:02.9	16.735	15.648	14.338	16.774	15.678	14.356	63.69	member
N5286-4421G	13:45:26.94	−51:20:30.5	16.625	15.439	14.141	–	–	–	− 23.47	field
N5286-4281G	13:45:15.88	−51:21:45.7	15.848	14.390	12.740	–	–	–	28.69	field
N5286-207G	13:46:14.17	−51:20:57.3	17.821	16.821	15.599	17.809	16.812	15.594	63.73	member
N5286-4311G	13:45:18.63	−51:22:31.0	16.857	15.940	14.894	–	–	–	− 41.65	field
N5286-4251G	13:45:15.04	−51:23:58.3	16.311	15.160	13.923	–	–	–	− 19.88	field
N5286-4201G	13:45:10.19	−51:24:27.4	16.349	15.120	13.828	–	–	–	37.50	field
N5286-4551G	13:45:37.15	−51:15:26.9	16.714	15.794	14.703	–	–	–	− 2.77	field
N5286-4681G	13:45:48.28	−51:18:16.0	16.840	15.530	14.114	–	–	–	− 38.99	field

3.1 GIRAFFE spectra

We couple our *BVI* photometry (see Section 2.1) with JHK_S from Two Micron All-Sky Survey (2MASS) and run the Infrared Flux Method (IRFM) described in Casagrande et al. (2010). This implementation of the IRFM has been recently validated also for giants, by direct comparison with interferometric angular diameters (Casagrande et al. 2014). For all stars, we assume the cluster metallicity [Fe/H] = −1.69 (Harris 2010), while adopting preliminary estimates for log *g* from isochrones taken from the Dartmouth Stellar Evolution Database (Dotter et al. 2008), which is appropriate since the IRFM depends very mildly on those parameters. To investigate the impact of the metallicity and gravity on the temperature values, we run the IRFM on all the stars by assuming [Fe/H] = −1.49 and [Fe/H] = −1.89, which corresponds to a metallicity of ±0.2 dex around the adopted value of [Fe/H] = −1.69. The two sets of temperatures are almost identical, and differ on average by ∼2 K. We emphasize that a variation of 0.4 dex in [Fe/H] is more than twice larger than the mean metallicity difference measured in NGC 5286, and conclude that the effect of the adopted metallicity is expected to be negligible on the results of this paper (see Section 4). Similarly, a difference in log *g* by 0.5 dex only marginally affects the derived T_{eff} values, as corresponds to a mean variation for this parameter of ∼3 K.

As discussed in Section 2.1, all our photometry is corrected for differential reddening. This correction is important for GCs like NGC 5286 that have a high mean reddening; indeed our correction suggests relatively high deviations from the absolute $E(B-V)$ value, with maximum variations being ∼0.1 mag. For the sake of deriving the correct effective temperatures, we must also account for the absolute value of reddening, which we assume to be $E(B-V) = 0.24$ from Harris (2010). In our implementation of the IRFM, the effective temperature of each star is obtained by averaging the values obtained from each infrared band; their standard deviation also provides an estimate of the internal accuracy of our results, which for this data set is of order 40 K, indirectly confirming the quality of our differential reddening corrections.

However, this estimate for the photometric T_{eff} could be derived only for a sample of our stars (39/55), that have good 2MASS photometry. For the remaining stars, we determined T_{eff} values from the T_{eff}–$(V-I)$ relation obtained by using the sample for which the photometric T_{eff} values could be derived. The use of the $(V-I)$ colour for this purpose is justified by the fact that it is insensitive to variations in light elements, and we have verified that stars of the two different RGBs of NGC 5286 overlap in the T_{eff}–$(V-I)$ relation. To ensure homogeneity, we used the T_{eff} derived by the T_{eff}–$(V-I)$ relation for all our stars. The spread around this colour–T_{eff} relation is 44 K, similar to the internal error associated with the photometric T_{eff}. We assumed that the internal uncertainty affecting our temperatures is ∼50 K. As a test to our scale of temperatures, we compared our adopted values with those derived from the projection of the targets on to the best-fitting α-enhanced isochrone (Dotter et al. 2008). The mean difference between the two sets of temperature is $\Delta T_{eff\,iso-adopted} = -40 \pm 12$ K.

Surface gravities were obtained from the apparent *V* magnitudes, corrected for differential reddening, the T_{eff} from above, bolometric corrections from Alonso, Arribas & Martínez-Roger (1999), and an apparent distance modulus of $(m - M)_V = 16.08$ (Harris 2010). We assume masses taken from isochrones of 0.81 $M_{\odot}$. Internal uncertainties associated with these log g determinations are formally small: internal errors in $T_{\rm eff}$ values of ±50 K and of ±0.05 unit in mass, affect the log g values by ±0.02 and ±0.03 dex, respectively. The internal photometric uncertainty associated with our V mag modifies our surface gravities by ∼0.01 dex. All these effects, added in quadrature, contribute to an internal error in log $g \lesssim 0.05$ dex.

For microturbulent velocities, we adopted the latest version of the relation used in the *Gaia*-ESO survey (GES; Gilmore et al. 2012; Bergemann et al., in preparation), which depends on $T_{\rm eff}$, log g and metallicity.[3] Temperatures and gravities were already set from above, while for metallicity we adopted [A/H] = −1.75 as first guess, and then the [Fe/H] abundance derived from Fe lines (as explained below). The dispersion of the recommended $\xi_{\rm t}$ values for the GES UVES spectra around the adopted relation is about 0.20 km s^{-1}, which is a reasonable internal uncertainty to be associated with our adopted values. The dispersion in [Fe/H] obtained for various RGB groups (see Section 5) has been considered as an estimate for the internal error in the metallicity used in the stellar atmosphere model.

3.2 UVES spectra

The high resolution and the large spectral coverage of UVES spectra allowed us to derive $T_{\rm eff}$, log g and $\xi_{\rm t}$ solely from spectroscopy. We determine $T_{\rm eff}$ by imposing the excitation potential (EP) equilibrium of the Fe I lines and gravity with the ionization equilibrium between Fe I and Fe II lines. For log g, we account for non-local thermodynamic equilibrium effects (NLTE) by imposing Fe II abundances slightly higher (by 0.05–0.07 dex) than the Fe I ones (Bergemann et al. 2012; Lind, Bergemann & Asplund 2012). For this analysis, microturbulent velocities, $\xi_{\rm t}$ were set to minimize any dependence on Fe I abundances as a function of equivalent widths (EWs).

In order to have an estimate of the internal errors associated with our spectroscopic atmospheric parameters, we have compared our $T_{\rm eff}$/log g values with those derived from the projection of the UVES targets on the best-fitting isochrone (as in Section 3.1). We obtain: $\Delta T_{\rm eff} = T_{\rm eff(Felines)} - T_{\rm eff(isochrone)} = -83 \pm 15$ K (rms = 36 K), and $\Delta \log g = \log g_{\rm (Felines)} - \log g_{\rm (isochrone)} = -0.29 \pm 0.07$ (rms = 0.16). Comparing with the $T_{\rm eff}$ values derived from the IRFM, we obtain a larger systematic, that is $\Delta T_{\rm eff} = T_{\rm eff(Felines)} - T_{\rm eff(IRFM)} = -132 \pm 12$ K (rms = 28 K), reflecting the fact that $T_{\rm eff}$ from the IRFM are ∼40 K higher than those derived from the best-fitting isochrone. Regarding the most reliable $T_{\rm eff}$ scale, both spectroscopic and photometric scales are likely affected by systematics. These systematics are due to the used Fe lines, adopted log *gf*, residual NLTE effects in the case of the spectroscopic $T_{\rm eff}$ scale, and mostly due to the adopted absolute reddening in the case of the photometric $T_{\rm eff}$ values. A systematic difference in $T_{\rm eff}$ by ∼100 K can be easily obtained by varying the mean reddening by ∼0.03 mag. In any case, our comparisons suggest that even if the spectroscopic $T_{\rm eff}$/log$g$ scales are systematically lower, the internal errors in these parameters are expected to be relatively small, comparable with the rms of the average differences, e.g. about 30–40 K and 0.16 dex, in temperature and gravity, respectively.

As a further check on internal errors associated with our spectroscopic $T_{\rm eff}$ we calculated, for each star, the errors on the slopes of the best least-squares fit in the relations between abundance versus EP The average of the errors corresponds to the typical error on the slope. Then, we fixed the other parameters and varied the temperature until the slope of the line that best fits the relation between abundances and EP became equal to the respective mean error. This difference in temperature can be considered a rough estimate of the error in temperature itself. The value we found is 50 K.

The same procedure applied for $T_{\rm eff}$ was also applied for $\xi_{\rm t}$, but using the relation between abundance and the reduced EWs. We obtained a mean error of 0.11 km s^{-1}.

As explained above, surface gravities for the UVES data have been obtained by imposing the ionization equilibrium between Fe I and Fe II lines (accounting for NLTE effects). The measures of Fe I and Fe II have averaged uncertainties of ⟨σ(Fe I)⟩ and ⟨σ(Fe II)⟩ (where σ(Fe I,II) is the dispersion of the iron abundances derived by the various spectral lines in each spectrum given by MOOG, divided by $\sqrt{N_{\rm lines} - 1}$). Hence, in order to have an estimate of the error associated with the adopted log$g$ values, we have varied the gravity of our stars such that the ionization equilibrium is satisfied between Fe I−⟨σ(Fe I)⟩ and Fe II+⟨< σ(Fe II)⟩, including the additional difference due to NLTE effects. The obtained mean error is $\Delta \log g = 0.14 \pm 0.02$. This error agrees with that estimated from the comparison with photometric values (0.16), hence we adopted an error of 0.16 for our adopted log$g$ values.

4 CHEMICAL ABUNDANCES ANALYSIS

Chemical abundances were derived from a local thermodynamic equilibrium (LTE) analysis by using the 2014 March version of the spectral analysis code MOOG (Sneden 1973), and the alpha-enhanced Kurucz model atmospheres of Castelli & Kurucz (2004), whose parameters have been obtained as described in Section 3. We used the abundances by Asplund et al. (2009) as reference solar abundances.

A list of our analysed spectral lines, with excitational potentials (EPs) and the adopted total oscillator strengths (log *gf*) is provided in Table 3. At the higher resolution of UVES we computed an EW-based analysis, with EWs estimated from Gaussian fitting of well isolated lines (Table 3), computed by using a home-made routine (see Marino et al. 2008). The exceptions from the EW analysis are discussed below. For GIRAFFE, given the lower resolution, we synthesized all spectral features. When required and atomic data are available from the literature, we considered hyperfine and/or isotopic splitting in our analysis (last column of Table 3). We comment in the following on the transitions that we used for UVES and GIRAFFE, depending on the spectral coverage, resolution and S/N of the two different data sets.

Iron: iron abundances were derived from the EWs of a number of isolated spectral lines for UVES data. Typically, we used a number of ∼30–35 lines for Fe I, and of ∼10 for Fe II. From GIRAFFE data, we synthesize a typical number of ∼20 Fe I lines.

Proton-capture elements: for UVES data, we determined Na abundances from spectral synthesis of the two Na I doublets at ∼5680 Å and ∼6150 Å; while in the smaller spectral range available for GIRAFFE we used only the doublet at ∼6150 Å. NLTE corrections from Lind et al. (2011) have been applied to all our Na spectral lines. Oxygen abundances were inferred from the synthesis of the forbidden [O I] line at 6300 Å both for UVES and GIRAFFE data. Telluric O_2 and H_2O spectral absorptions often affect the O line at 6300 Å. Indeed, for our NGC 5286 targets the analysed O transition is contaminated by O_2 lines. We have removed tellurics

[3] http://great.ast.cam.ac.uk/GESwiki/GesWg/GesWg11/Microturbulence

Table 3. Line list for the program stars. For the UVES targets we list the measured EWs. For GIRAFFE, we synthesized the same lines used for UVES, in the common spectral range 6120–6400 Å; a few lines have been used only for GIRAFFE.

Wavelength (Å)	Species	L.E.P. (eV)	log *gf*	1219U (mÅ)	1439U (mÅ)	859U (mÅ)	1309U (mÅ)	579U (mÅ)	1339U (mÅ)	177U (mÅ)	Ref. for log *gf*
6300.304	8.0	0.000	−9.819	syn	syn	syn	syn	–	syn	syn	1
5682.633	11.0	2.102	−0.710	syn	syn	syn	syn	syn	syn	syn	2
5688.205	11.0	2.104	−0.450	syn	syn	syn	syn	syn	syn	syn	2
6154.226	11.0	2.102	−1.550	–	–	syn	syn	–	syn	–	2
6160.747	11.0	2.104	−1.250	syn	syn	syn	syn	syn	syn	syn	2
5528.405	12.0	4.346	−0.498	143.5	147.2	184.8	128.8	136.8	168.0	145.9	3
5711.088	12.0	4.346	−1.810	50.2	56.2	84.4	44.4	46.0	66.5	49.3	3
6318.717	12.0	5.108	−1.973	–	11.4	17.3	–	–	15.7	–	3
6696.023	13.0	3.140	−1.340	syn	syn	56.4	36.8	20.2	28.9	–	2
6698.673	13.0	3.140	−1.640	syn	syn	34.2	18.4	–	18.6	–	2
5690.425	14.0	4.930	−1.870	12.1	–	27.5	14.5	–	17.6	11.0	4
5701.104	14.0	4.930	−2.050	–	–	18.4	9.6	–	18.1	9.7	4
6125.030	14.0	5.620	−1.570	–	11.5	15.6	–	–	16.9	–	3
6142.490	14.0	5.620	−1.430	–	–	8.2	–	–	–	–	3
6145.020	14.0	5.620	−1.490	–	–	–	11.2	–	–	8.5	3
6155.140	14.0	5.620	−0.860	19.6	22.5	35.2	25.0	25.7	34.3	20.2	3
6237.319	14.0	5.614	−1.080	14.2	23.9	–	–	–	24.0	13.7	3
6243.815	14.0	5.616	−1.260	–	–	–	15.1	10.8	19.2	7.6	3
6244.466	14.0	5.616	−1.290	–	–	29.6	11.3	–	16.1	–	3
6414.990	14.0	5.870	−1.030	–	–	–	10.0	–	–	–	3
5261.704	20.0	2.521	−0.579	54.3	60.8	95.8	59.8	65.7	79.1	56.7	5, 6
5512.980	20.0	2.933	−0.464	35.2	39.5	72.3	39.3	35.2	53.5	34.4	5
5588.749	20.0	2.526	0.358	107.7	116.8	140.6	106.9	102.6	115.2	106.1	5
5590.114	20.0	2.521	−0.571	61.2	58.7	91.1	64.9	56.8	73.8	54.9	5, 6
6122.217	20.0	1.886	−0.410	128.0	131.1	170.1	129.7	127.0	139.7	126.9	1
6162.173	20.0	1.899	0.100	143.8	141.2	193.4	136.2	135.8	155.1	138.3	1
6166.439	20.0	2.521	−0.900	28.7	32.1	66.0	34.2	36.1	43.2	27.3	4
6169.042	20.0	2.523	−0.550	51.0	59.3	90.9	53.2	48.7	65.1	47.3	4
6169.563	20.0	2.526	−0.270	69.2	73.4	109.4	68.8	61.9	85.6	66.3	4
6439.075	20.0	2.526	0.390	121.7	120.2	161.1	121.7	118.6	134.1	120.7	5
6471.662	20.0	2.526	−0.686	58.2	60.2	–	65.6	–	76.5	56.3	5, 6
6493.781	20.0	2.521	−0.109	–	97.8	–	94.8	–	–	–	5
6499.650	20.0	2.523	−0.818	54.4	57.0	95.7	52.4	49.4	65.7	49.9	5, 6
5239.813	21.1	1.455	−0.770	59.7	57.6	90.9	71.4	59.3	75.4	59.9	4
5526.790	21.1	1.768	0.020	85.7	85.9	104.5	80.1	80.9	85.9	80.8	4
5552.224	21.1	1.455	−2.119	–	–	13.2	–	–	–	–	5
6245.637	21.1	1.507	−0.980	38.9	–	64.4	43.6	33.4	41.0	38.2	1
6279.753	21.1	1.500	−1.210	–	26.5	–	–	–	29.2	–	1
6320.851	21.1	1.500	−1.770	–	–	15.0	–	–	–	–	1
6604.601	21.1	1.357	−1.310	28.4	37.5	63.4	39.1	36.5	42.6	34.5	4
4820.411	22.0	1.502	−0.439	–	–	114.7	–	–	–	–	4
4926.148	22.0	0.818	−2.170	–	–	25.1	–	–	–	–	4
4981.731	22.0	0.848	0.504	114.1	119.7	167.3	–	114.1	119.9	108.6	4
5009.650	22.0	0.020	−2.259	29.7	30.2	89.2	36.9	24.9	45.6	30.0	1
5024.844	22.0	0.818	−0.602	68.8	67.4	120.9	–	79.4	85.0	74.5	4
5039.960	22.0	0.020	−1.130	89.9	98.1	146.8	90.7	104.5	109.6	93.8	1
5043.590	22.0	0.840	−1.733	–	–	56.0	15.1	–	21.7	12.4	4
5062.100	22.0	2.160	−0.464	–	–	19.5	–	–	–	–	4
5145.460	22.0	1.460	−0.574	21.4	20.8	56.6	28.7	28.5	31.0	23.4	4
5219.702	22.0	0.021	−2.292	30.3	–	93.9	26.4	29.3	42.9	28.6	1
5223.630	22.0	2.090	−0.558	–	–	14.0	–	–	–	–	1
5295.775	22.0	1.067	−1.633	–	–	33.1	–	11.8	–	–	4
5426.250	22.0	0.021	−3.006	–	18.6	44.3	–	–	14.4	–	1
5460.499	22.0	0.048	−2.804	–	–	56.1	–	11.7	–	–	5
5471.193	22.0	1.443	−1.390	–	–	23.4	–	–	–	–	4
5490.150	22.0	1.460	−0.933	–	–	43.5	10.7	11.1	–	11.3	4
5648.565	22.0	2.495	−0.250	–	–	10.7	–	–	–	–	4
5689.460	22.0	2.300	−0.469	–	–	16.2	–	–	–	–	1
5702.660	22.0	2.290	−0.570	–	–	9.9	–	–	7.1	–	3
5720.440	22.0	2.290	−0.900	–	–	8.6	–	–	–	–	4
5903.315	22.0	1.067	−2.145	–	–	18.6	–	–	–	–	4
5937.809	22.0	1.067	−1.890	–	–	24.4	–	–	–	–	4

Table 3 – *continued*

Wavelength (Å)	Species	L.E.P. (eV)	log *gf*	1219U (mÅ)	1439U (mÅ)	859U (mÅ)	1309U (mÅ)	579U (mÅ)	1339U (mÅ)	177U (mÅ)	Ref. for log *gf*
5978.541	22.0	1.873	−0.496	11.2	–	45.3	14.1	–	17.7	12.7	4
6064.626	22.0	1.046	−1.944	–	–	27.6	–	–	–	–	4
6091.171	22.0	2.267	−0.423	–	–	23.8	–	–	–	–	4
6126.216	22.0	1.067	−1.424	15.9	–	58.6	14.5	18.2	23.7	11.9	4
6258.102	22.0	1.443	−0.355	33.3	32.8	87.6	37.7	33.2	47.8	32.6	1
6312.236	22.0	1.460	−1.552	–	11.4	13.6	–	–	–	–	4
6554.220	22.0	1.440	−1.219	7.7	–	41.9	7.2	7.1	15.2	–	4
4865.610	22.1	1.120	−2.810	69.7	57.0	82.5	63.2	69.1	74.0	60.9	3
4874.010	22.1	3.100	−0.950	30.2	42.6	43.9	33.5	–	34.9	29.3	3
4911.200	22.1	3.120	−0.510	40.7	–	57.4	40.0	36.9	47.4	35.7	3
5185.910	22.1	1.890	−1.500	85.5	74.4	101.8	91.1	82.0	88.1	80.9	3
5211.530	22.1	2.590	−1.165	35.4	31.4	42.1	–	30.7	46.1	31.8	4
5336.786	22.1	1.582	−1.630	92.5	93.7	–	101.2	100.5	–	97.0	3
5418.767	22.1	1.582	−2.110	63.0	64.5	89.0	67.7	58.9	68.9	66.8	3
6606.949	22.1	2.061	−2.900	14.4	8.4	–	–	–	–	–	3
5668.361	23.0	1.081	−1.030	–	–	14.6	–	–	–	–	4
5670.853	23.0	1.081	−0.420	–	–	36.2	–	–	–	14.3	4
5737.059	23.0	1.064	−0.740	–	–	20.5	–	–	–	–	4
6039.722	23.0	1.064	−0.650	–	–	26.6	–	–	–	–	4
6090.214	23.0	1.081	−0.062	14.1	25.4	60.5	13.3	–	–	14.8	4
6111.645	23.0	1.043	−0.715	–	–	25.7	–	–	–	–	4
6119.523	23.0	1.064	−0.320	9.2	–	43.1	–	–	–	–	4
6135.361	23.0	1.051	−0.746	–	–	21.9	–	–	–	–	4
6251.827	23.0	0.287	−1.340	–	–	49.4	–	–	–	–	4
4936.336	24.0	3.113	−0.340	–	–	26.4	–	–	–	–	4
5296.691	24.0	0.983	−1.410	63.9	66.5	124.4	71.8	69.5	79.8	70.0	4
5348.315	24.0	1.004	−1.290	79.4	77.6	125.2	80.8	74.9	93.1	75.0	4
6330.091	24.0	0.941	−2.910	12.4	–	48.5	–	–	16.4	–	4
5394.677	25.0	0.000	−3.503	36.5	34.0	136.2	33.5	33.2	47.4	35.5	4
5420.355	25.0	2.143	−1.460	–	23.6	52.7	–	–	30.3	–	4
5432.546	25.0	0.000	−3.795	17.7	21.1	99.8	18.9	–	31.7	24.8	4
5537.760	25.0	2.187	−2.017	–	–	27.8	–	–	–	–	1
6013.513	25.0	3.072	−0.252	16.7	–	41.0	–	–	16.4	13.4	4
6021.819	25.0	3.075	0.035	24.6	26.7	65.1	26.3	28.3	38.6	26.1	4
4994.130	26.0	0.920	−3.080	122.4	125.1	177.8	112.6	138.4	133.7	136.6	4
5217.390	26.0	3.210	−1.162	83.9	81.3	103.0	77.7	73.3	84.2	81.4	4
5364.870	26.0	4.450	0.228	61.0	73.5	90.4	65.1	65.5	82.0	71.9	4
5367.470	26.0	4.420	0.443	77.9	82.4	98.3	73.0	76.3	80.4	71.9	4
5383.370	26.0	4.310	0.645	89.9	90.0	122.2	97.7	94.5	96.3	93.9	4
5398.280	26.0	4.450	−0.710	24.9	27.8	48.6	30.4	21.8	31.9	25.9	4
5415.200	26.0	4.390	0.642	79.7	87.2	110.8	88.8	80.3	93.3	82.8	4
5445.040	26.0	4.390	−0.020	60.3	63.4	84.3	61.1	58.0	72.7	61.2	1
5466.400	26.0	4.370	−0.630	32.8	38.3	61.5	36.4	33.7	42.6	27.4	1
5569.620	26.0	3.420	−0.486	94.5	97.6	134.1	98.4	89.0	101.0	93.1	4
5638.260	26.0	4.220	−0.840	25.3	31.7	55.6	30.3	30.7	37.4	30.9	4
5859.580	26.0	4.550	−0.419	15.5	25.9	–	–	–	32.8	15.0	5
5862.360	26.0	4.550	−0.051	25.2	39.4	53.2	32.9	29.5	32.0	–	1
5905.670	26.0	4.650	−0.770	12.3	21.1	24.9	16.7	–	10.8	18.0	4
5930.180	26.0	4.650	−0.230	–	41.2	64.3	32.4	–	42.5	–	1
6024.060	26.0	4.550	−0.120	48.5	48.9	–	54.6	52.0	60.6	46.8	1
6027.050	26.0	4.080	−1.089	22.2	–	46.3	23.1	21.8	28.8	24.4	4
6056.010	26.0	4.730	−0.460	20.5	–	39.2	23.7	20.5	26.0	16.5	1
6065.480	26.0	2.610	−1.530	101.4	92.3	149.2	101.5	102.7	105.8	102.3	1
6151.617	26.0	2.174	−3.299	29.7	28.0	72.6	37.8	24.3	38.7	32.4	4
6165.360	26.0	4.140	−1.550	–	–	25.4	9.7	–	12.9	6.5	1
6173.340	26.0	2.220	−2.880	51.0	50.5	96.9	52.7	51.1	63.8	51.1	4
6187.990	26.0	3.940	−1.720	9.0	12.0	29.0	–	–	–	–	1
6200.320	26.0	2.607	−2.437	47.0	43.3	96.4	56.7	45.8	64.3	50.4	4
6219.280	26.0	2.196	−2.433	79.0	76.0	126.1	81.8	76.4	89.3	78.5	4
6226.740	26.0	3.880	−2.220	–	–	12.8	–	–	–	–	1
6246.320	26.0	3.600	−0.960	68.1	72.7	106.2	75.2	61.9	77.8	66.7	1
6252.560	26.0	2.400	−1.687	–	101.4	152.9	109.3	99.2	112.9	108.7	4
6322.690	26.0	2.586	−2.426	54.2	–	100.7	57.3	57.6	65.1	57.4	4

Table 3 – *continued*

Wavelength (Å)	Species	L.E.P. (eV)	log *gf*	1219U (mÅ)	1439U (mÅ)	859U (mÅ)	1309U (mÅ)	579U (mÅ)	1339U (mÅ)	177U (mÅ)	Ref. for log *gf*
6335.330	26.0	2.196	−2.230	85.6	85.9	126.4	84.0	86.6	91.2	88.9	1
6336.820	26.0	3.684	−1.050	55.4	59.5	96.6	65.8	59.2	70.3	56.9	1
6393.600	26.0	2.431	−1.620	108.5	111.5	160.0	113.5	107.0	118.4	114.7	1
6411.650	26.0	3.650	−0.718	76.4	75.3	113.7	75.8	73.7	81.4	80.3	4
6430.850	26.0	2.180	−2.006	104.6	104.1	156.4	105.1	101.6	109.7	105.4	4
6593.870	26.0	2.430	−2.422	50.8	54.8	83.7	52.4	51.8	58.4	51.3	4
6750.150	26.0	2.420	−2.621	–	–	–	–	58.3	–	–	4
4993.360	26.1	2.810	−3.620	28.6	–	35.4	29.3	–	35.6	31.7	7
5234.620	26.1	3.220	−2.180	78.3	79.9	82.9	83.5	78.3	77.3	78.1	7
5264.810	26.1	3.230	−3.130	31.6	32.1	32.9	32.0	32.0	33.6	33.5	7
5325.560	26.1	3.220	−3.160	26.6	36.3	34.6	29.2	37.6	36.4	30.5	7
5414.070	26.1	3.220	−3.580	–	20.9	14.5	13.6	17.7	17.0	10.3	7
5425.250	26.1	3.200	−3.220	26.2	21.2	32.1	31.7	29.9	23.0	22.0	7
6084.110	26.1	3.200	−3.791	10.0	–	20.3	12.6	9.8	11.3	–	7
6149.240	26.1	3.890	−2.690	18.9	17.1	24.1	21.4	–	–	14.5	7
6247.560	26.1	3.890	−2.300	34.6	35.2	35.8	35.2	32.0	38.4	35.1	7
6432.680	26.1	2.890	−3.570	27.5	23.4	33.8	27.2	24.0	30.9	27.1	7
6456.380	26.1	3.900	−2.050	37.3	35.7	–	42.5	39.9	39.1	34.4	7
4813.467	27.0	3.216	0.050	–	25.4	34.2	21.2	–	18.4	15.0	1
5342.695	27.0	4.021	0.690	7.5	–	13.2	9.6	–	–	–	1
5352.045	27.0	3.576	0.060	–	–	14.7	–	–	–	–	4
5530.774	27.0	1.710	−2.060	–	–	30.1	–	–	–	–	4
5590.720	27.0	2.042	−1.870	–	–	19.7	–	–	–	–	4
5647.234	27.0	2.280	−1.560	3.8	–	18.5	–	–	10.0	–	4
6188.996	27.0	1.710	−2.460	–	–	24.2	14.6	–	–	–	4
6454.990	27.0	3.632	−0.250	–	–	9.2	–	–	–	–	4
5010.934	28.0	3.635	−0.870	–	–	29.3	–	–	17.1	–	5
5435.855	28.0	1.986	−2.590	24.7	–	62.4	30.5	24.5	33.1	22.5	5
5578.711	28.0	1.676	−2.640	36.8	33.5	80.6	36.0	31.3	46.3	33.8	5
5593.733	28.0	3.898	−0.840	–	15.8	18.8	–	–	11.0	9.3	5
6086.276	28.0	4.266	−0.530	–	–	19.2	–	–	11.7	–	5
6108.107	28.0	1.676	−2.450	46.6	45.1	90.8	43.1	45.1	54.9	43.5	5
6111.066	28.0	4.088	−0.870	–	–	15.9	–	–	–	–	5
6175.360	28.0	4.090	−0.530	10.0	10.2	20.5	11.0	–	15.1	9.8	8
6176.807	28.0	4.088	−0.260	17.2	20.3	30.1	17.7	17.3	21.9	15.5	5
6177.236	28.0	1.826	−3.500	–	–	19.5	–	–	–	–	5
6186.710	28.0	4.110	−0.960	–	–	8.6	–	–	–	–	8
6327.593	28.0	1.676	−3.150	22.6	17.5	66.8	25.1	24.4	–	22.6	5
6482.796	28.0	1.935	−2.630	21.1	30.6	57.4	25.0	25.5	30.5	23.7	5
6643.629	28.0	1.676	−2.300	77.9	70.1	129.7	74.2	75.4	90.2	77.1	5
6767.768	28.0	1.826	−2.170	63.4	59.7	110.1	70.7	63.1	73.2	67.0	5
6772.313	28.0	3.658	−0.980	–	–	22.2	11.1	–	–	8.5	5
5105.537	29.0	1.389	−1.516	syn	syn	syn	syn	syn	syn	syn	9, HFS
5218.196	29.0	3.814	0.476	–	–	syn	–	–	syn	–	9, HFS
4810.528	30.0	4.078	−0.137	51.0	56.9	69.8	54.1	65.0	68.0	51.8	5
5087.416	39.1	1.084	−0.170	56.5	85.0	94.7	55.0	56.8	87.5	56.2	10
5200.406	39.1	0.992	−0.570	48.2	84.5	–	50.3	51.5	79.7	40.4	10
5402.774	39.1	1.839	−0.510	–	36.8	34.2	18.6	–	35.4	9.6	1
5544.611	39.1	1.738	−1.090	–	18.6	18.9	–	–	20.5	–	10
5112.270	40.1	1.665	−0.590	syn	syn	syn	syn	syn	syn	syn	11
5853.668	56.1	0.604	−1.010	59.3	88.1	–	–	–	–	–	12, HFS
6141.713	56.1	0.704	−0.070	134.1	169.7	231.6	136.6	133.8	203.4	137.2	13, HFS
6496.897	56.1	0.604	−0.377	131.2	164.3	–	133.1	131.3	188.8	131.3	14, HFS
4920.980	57.1	0.126	−0.580	syn	syn	syn	syn	syn	syn	syn	15
4921.780	57.1	0.244	−0.450	syn	syn	syn	syn	syn	syn	syn	15
6262.290	57.1	0.403	−1.220	–	syn	syn	syn	–	syn	–	15, HFS
6390.477	57.1	0.321	−1.410	–	syn	syn	syn	syn	syn	syn	15, HFS
6774.268	57.1	0.126	−1.820	–	syn	syn	–	–	syn	–	1
5274.229	58.1	1.044	0.150	13.9	24.2	51.3	11.2	–	51.0	16.1	5
5330.556	58.1	0.869	−0.460	–	–	31.8	–	–	25.8	–	5
5219.045	59.1	0.795	−0.050	–	–	syn	–	–	–	–	16, HFS
5259.728	59.1	0.633	0.120	–	–	syn	–	–	syn	–	16, 17
5322.772	59.1	0.482	−0.120	syn	syn	syn	–	–	syn	syn	16, 18

Table 3 – *continued*

Wavelength (Å)	Species	L.E.P. (eV)	log *gf*	1219U (mÅ)	1439U (mÅ)	859U (mÅ)	1309U (mÅ)	579U (mÅ)	1339U (mÅ)	177U (mÅ)	Ref. for log *gf*
5416.374	60.1	0.859	−0.980	–	–	17.7	–	–	–	–	5
5740.858	60.1	1.160	−0.530	–	–	21.2	–	–	–	–	5
4947.020	60.1	0.559	−1.130	–	–	24.4	–	–	–	–	5
5319.815	60.1	0.550	−0.140	29.7	43.4	87.5	39.9	31.6	68.4	29.6	5
5276.869	60.1	0.859	−0.668	–	–	30.1	–	–	20.9	–	5
5431.516	60.1	1.121	−0.470	–	–	22.3	–	–	17.8	–	5
6437.640	63.1	1.319	−0.320	–	–	syn	–	syn	–	–	19, HFS
6645.064	63.1	1.380	0.120	syn	–	syn	syn	syn	syn	syn	19, HFS
				GIRAFFE additional synthesized lines							
6161.297	20.0	2.521	−1.030								4
6157.728	26.0	4.073	−1.260								1
6309.920	21.1	1.469	−1.570								1
6180.203	26.0	2.725	−2.780								1
6229.226	26.0	2.843	−2.970								1
6265.132	26.0	2.174	−2.550								1
6270.223	26.0	2.856	−2.710								1
6297.793	26.0	2.221	−2.740								1
6344.148	26.0	2.431	−2.923								1

Notes. References: (1) Kurucz compendium; (2) Fuhr & Wiese (2009); (3) Yong et al. (2014); (4) NIST; (5) *Gaia*-ESO linelist (Heiter et al., in prep.); (6) Yong et al. (2013); (7) Meléndez & Barbuy (2009); (8) Johnson & Pilachowski (2010); (9) Bielski (1975), Kurucz & Bell (1995); (10) Hannaford et al. (1982); (11) Biemont et al. (1981); (12) Gallagher (1967), Sneden, Pilachowski & Kraft (2000); (13) Gallagher (1967), Burris et al. (2000); (14) Gallagher (1967), Sneden et al. (1996); (15) Lawler, Bonvallet & Sneden (2001a); (16) Sneden et al. (2009); (17) Ivarsson, Litzen & Wahlgren (2001); (18) Li et al. (2007); (19) Lawler et al. (2001b).

by using the software MOLECFIT[4] provided by ESO (Smette et al. 2015; Kausch et al. 2014). But, even with such a subtraction procedure, we caution that residual telluric feature contamination might be of concern for the analysis of the 6300.3 [O I] line. Magnesium and aluminium abundances were possible only for the UVES data. Aluminium was determined from the synthesis of the doublet at 6696 Å. Spectral synthesis of the analysed Al transitions allow us to account for possible blending caused by CN molecules, that are substantial in the case of the star #859U, which is the coolest in our UVES sample. Magnesium has been inferred from EWs of the transitions at ∼5528, 5711, and 6318 Å.

α elements: for UVES spectra, we determined abundances from EWs of Si, Mg (see above), Ca, and Ti (I and II). All these α elements, except Mg, could be inferred also for the smaller GIRAFFE spectral range, where we measured abundances for a subsample of lines using spectral synthesis.

Iron-peak elements: from UVES spectra, we determined abundances for Sc, V, Cr, Ni, Zn using EWs. Abundances for Cu were inferred by synthesizing the Cu I lines at 5105, 5218 Å. Both hyperfine and isotopic splitting were included in the Cu analysis, with well-studied spectral line component structure from the Kurucz (2009) compendium.[5] Solar system isotopic fractions were assumed in the computations: f(^{63}Cu) = 0.69 and f(^{65}Cu) = 0.31. For Zn we analysed the Zn I line at 4810 Å, for which we determined EWs. This line has no significant hyperfine or isotopic substructures, and was treated as a single absorber. From GIRAFFE spectra we inferred only Ni and Sc using spectral synthesis.

Neutron-capture elements: we derived Y, Zr, La, Ce, Pr, Nd, Eu, and Ba from the UVES spectra, and Ba and La from the GIRAFFE spectra. An EWs-analysis was performed for Y, Ce, Nd, and Ba, and spectral synthesis for the other elements for which hyperfine and/or isotopic splitting and/or blending features needed to be taken into account. Specifically, we have employed spectrum syntheses to derive the La and Eu abundances, because the spectral features of both La II and Eu II have significant hyperfine substructure, and the Eu II lines also have isotopic splitting. Because barium lines suffer from both hyperfine and isotopic substructures, and in the case of the 6141 Å line blending by Fe, we used the blended-line EW analysis option available in MOOG. Zirconium abundances are available for all the seven stars observed with UVES from the Zr II line at 5112 Å.

Some examples of our spectral synthesis are plotted in Fig. 3 for two stars observed with UVES (859U and 1309U), and two stars observed with GIRAFFE (1567G and 1649G). The represented spectra are shown around some *n*-capture features (La and Nd) for 859U and 1649G, the Cu line at ∼5105 Å for the star 1309U and around the forbidden O line for 1567G. A list of all the derived chemical abundances and adopted atmospheric parameters is provided in Tables 4 and 5 for GIRAFFE and UVES, respectively.

Internal uncertainties in chemical abundances due to the adopted model atmospheres were estimated by varying the stellar parameters, one at a time, by the amounts derived in Section 3. The internal uncertainty associated with the photometric surface gravities are formally small, so we conservatively adopt an error of 0.2 dex. Thus, we vary $T_{\rm eff}$/log*g*/[Fe/H]/$\xi_{\rm t}$ = ±50 K/±0.16 dex/±0.05 dex/±0.11 km s^{-1} for UVES, and ±50 K/±0.20 dex/±0.05 dex/±0.20 km s^{-1} for GIRAFFE. Variations in chemical abundances due to variations in atmospheric parameters are listed in Tables 6 and 7.

In addition to the contribution introduced by internal errors in atmospheric parameters, we estimated the contribution due to the limits of our spectra, e.g. due to the finite S/N, fit quality, which affect the measurements of EWs and the spectral synthesis. The contribution due to EWs, used in the case of UVES data, has been calculated by varying the EWs of spectral lines by ±4.5 mÅ, that is the typical error associated with our EWs measurements as we

[4] http://www.eso.org/sci/software/pipelines/skytools/molecfit
[5] Available at: http://kurucz.harvard.edu/.

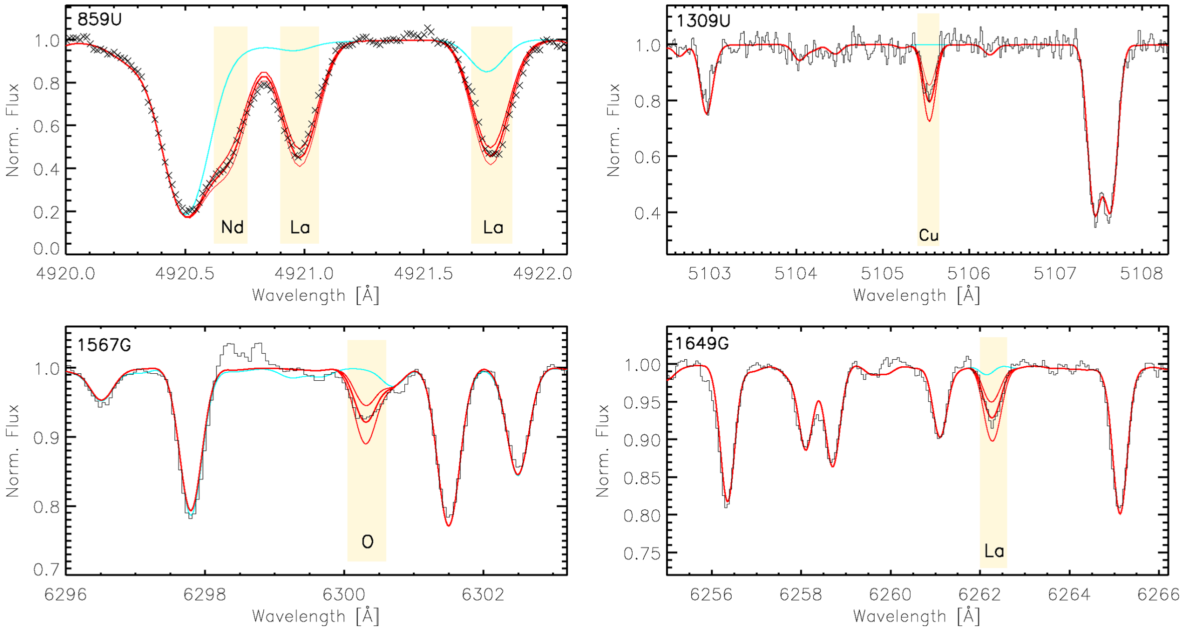

Figure 3. Observed and synthetic spectra around some analysed transitions for two stars observed with UVES (upper panels), and two stars observed with GIRAFFE (lower panels). In each panel, the observed spectrum has been represented in black. The cyan spectra have been computed with no contribution from La and Nd, and Cu for stars 859U and 1309U, respectively, and no contribution from O and La for stars 1567G and 1649G, respectively. The thick red line is the best-fitting synthesis; while the red thin lines are the syntheses computed with abundances altered by ±0.2 dex from the best value.

have verified by comparing Fe lines for stars with similar atmospheric parameters (e.g. #1219U and #579U). The variations in the abundances obtained by varying the EWs have been then divided by the square root of the number of available spectral lines minus one. Since the EWs measurement errors are random, the error associated with those elements with a larger number of lines is lower. For the other elements, we have a lower number of lines, so the error contribution introduced by EWs uncertainties is higher.

For GIRAFFE data, we derived EWs only for the Ba line at 6141 Å. To evaluate the error affecting this measurement, we re-derive EWs from single (not combined) exposures for three stars observed with GIRAFFE, and derived the error associated with the mean EW obtained for each star. The derived error in EW for this Ba line is ∼5 mÅ. The impact of this uncertainty to the Ba abundance has been derived in the same manner as for the UVES data, e.g. by changing the EWs of the Ba line by this quantity and re-determining the abundances. The mean difference in [Ba/Fe] due to a change by 5 mÅ in the EWs of the Ba transition is 0.04 dex (see Table 7).

To estimate the uncertainties introduced by the limited S/N in the fitting procedure used in the spectral synthesis, we computed a set of 100 synthetic spectra for two stars representative of the UVES sample (1439U and 859U) and two stars representative of the GIRAFFE sample (527G and 1077G). These set of synthetic spectra were calculated by using the best-fitting inferred abundances, and were then degraded to the S/N of the observed spectra. We then analysed the chemical abundances of all these synthetic spectra in the same manner as the observed spectra. The scatter that we obtain from the abundances from each spectral line for a set of synthetic spectra corresponding to a given star, represents a fair estimate of the uncertainty introduced by the fitting procedure, due to the S/N, the pixel size and the continuum estimate. These uncertainties strongly depend on the S/N, and are higher for less luminous stars. Indeed, our set of synthetic spectra has been computed at two different S/N values, e.g. S/N = 80 and 200, representing the lower and higher S/N of our spectra. These errors are listed as $\sigma_{\rm fit}$ in Tables 7 and 6, for GIRAFFE and UVES, respectively. Double entries in these errors correspond to the different values obtained at the two different S/N values. Similarly to the discussion for EWs, these errors are random, and the corresponding uncertainty in chemical abundances is lower for those elements with a large number of lines (e.g. Fe).

All the contributions both from atmospheric parameters and S/N are included in the total uncertainty values $\sigma_{\rm total}$ listed in the last columns of Tables 7 and 6. These total uncertainties have been obtained following the formalism given in Johnson (2002), and also account for correlations in the atmospheric parameters determination. For GIRAFFE, correlations between $T_{\rm eff}$ and log*g* are small, and we considered only covariance terms including $\xi_{\rm t}$.

We remark here that we are interested in star-to-star abundance variations. For this reason, we are only marginally interested in external sources of error which are systematic and much more difficult to evaluate. Later in the paper, we will discuss mostly internal uncertainties affecting our abundances, while systematic effects will be discussed only when relevant, e.g. when comparing abundances inferred from two the different analysed data sets (GIRAFFE and UVES).

5 THE CHEMICAL COMPOSITION OF NGC 5286

From our abundance analysis NGC 5286 is a metal-poor GC, with the typical enhancements in α-elements (Si, Ca, Ti). The mean metallicity obtained from our sample of GIRAFFE probable NGC 5286 members, composed of 55 stars, is [Fe/H] = −1.72 ± 0.01 dex, with a dispersion σ = 0.11 dex. From the UVES sample, composed of only seven stars, we obtain a mean [Fe/H] = −1.80 ± 0.05 dex, with a similar dispersion, e.g. σ = 0.12 dex. The systematically lower Fe abundances inferred from UVES can be easily explained by systematic differences in atmospheric parameters, which have been derived in a different manner for the two sets of data. Indeed, as discussed in Section 3,

Table 4. Adopted atmospheric parameters and chemical abundances derived for the NGC 5286 stars observed with GIRAFFE. For sodium, we list both the LTE ([Na/Fe]$_{LTE}$) and the NLTE ([Na/Fe]$_{NLTE}$) abundances. Line-to-line scatter is listed when more than one line has been analysed. The last column lists the status of *s*-rich or *s*-poor assigned to each star.

ID	T_{eff} (K)	log*g* (cgs)	ξ_t (km s^{-1})	[Fe/H]	±	[O/Fe]	[Na/Fe] NLTE	±	[Na/Fe] LTE	±	[Si/Fe]	±	[Ca/Fe]	±	[Sc/Fe]	±	[Ti/Fe]	[Ni/Fe]	±	[Ba/Fe]	[La/Fe]	±	group
N5286-667G	5181	2.47	1.60	−1.66	0.07	–	–	–	–	–	0.54	–	0.30	0.04	−0.14	–	–	–	–	0.12	–	–	*s*-poor
N5286-527G	4429	1.00	1.95	−1.75	0.03	0.39	0.20	0.08	0.26	0.09	0.36	0.02	0.32	0.06	0.06	0.00	0.37	0.15	0.19	0.51	0.30	–	*s*-poor
N5286-1117G	4520	1.20	1.91	−1.87	0.03	0.51	−0.21	–	−0.17	–	0.36	0.04	0.32	0.10	0.05	0.09	0.31	0.16	0.10	0.15	0.11	0.02	*s*-poor
N5286-757G	4432	0.99	1.94	−1.66	0.04	0.53	0.10	0.12	0.14	0.13	0.51	0.10	0.37	0.07	0.00	0.17	0.57	0.19	0.33	0.87	0.84	–	*s*-rich
N5286-697G	4958	2.15	1.67	−1.79	0.04	0.35	0.12	–	0.20	–	0.26	0.18	0.26	0.13	−0.08	–	0.20	0.02	–	−0.07	–	–	*s*-poor
N5286-779G	5102	2.31	1.61	−1.56	0.04	–	–	–	–	–	0.24	0.13	0.17	0.09	−0.17	–	–	0.16	–	0.92	–	–	*s*-rich
N5286-399G	4965	2.00	1.69	−1.60	0.03	–	0.50	–	0.58	–	0.33	0.06	0.39	0.13	−0.03	–	0.32	0.03	–	0.98	0.96	–	*s*-rich
N5286-989G	5147	2.48	1.58	−1.60	0.04	–	–	–	–	–	0.34	–	0.31	0.06	−0.12	–	0.40	–	–	0.91	–	–	*s*-rich
N5286-1297G	4350	0.90	1.99	−1.84	0.03	0.64	−0.19	–	−0.15	–	0.32	0.04	0.26	0.10	0.13	0.08	0.29	0.06	0.18	0.56	0.12	0.01	*s*-poor
N5286-1767G	5021	2.31	1.63	−1.71	0.03	–	0.29	–	0.38	–	0.55	0.12	0.46	0.13	0.26	–	0.48	–	–	0.16	–	–	*s*-poor
N5286-1269G	4988	2.24	1.63	−1.65	0.01	0.20	0.57	0.15	0.65	0.16	0.47	0.02	0.44	0.13	−0.02	–	0.23	0.08	–	1.14	1.03	–	*s*-rich
N5286-939G	4972	2.27	1.63	−1.70	0.04	–	0.28	–	0.36	–	0.45	0.08	0.44	0.13	0.03	–	0.30	–	–	0.61	0.56	–	*s*-rich
N5286-1197G	5043	2.36	1.63	−1.80	0.03	0.76	–	–	–	–	0.49	0.22	0.50	0.14	−0.04	–	–	–	–	0.46	–	–	*s*-poor
N5286-1057G	4974	2.10	1.70	−1.87	0.03	0.60	–	–	–	–	0.23	–	0.36	0.16	−0.04	–	–	–	–	−0.01	–	–	*s*-poor
N5286-1547G	4838	2.00	1.70	−1.75	0.02	0.58	–	–	–	–	0.44	0.14	0.41	0.13	0.03	–	0.33	0.10	0.06	0.05	–	–	*s*-poor
N5286-1077G	5017	2.21	1.66	−1.74	0.03	–	0.21	–	0.29	–	0.35	0.23	0.34	0.12	−0.09	–	0.22	0.16	–	0.18	–	–	*s*-poor
N5286-5441G	5104	2.08	1.68	−1.62	0.04	0.72	–	–	–	–	0.33	0.04	0.39	0.20	0.02	–	–	0.12	0.03	0.28	–	–	*s*-poor
N5286-1607G	5123	2.34	1.62	−1.62	0.03	–	0.57	–	0.66	–	0.53	0.16	0.60	0.26	0.06	–	–	–	–	0.06	–	–	*s*-poor
N5286-969G	5055	2.39	1.60	−1.63	0.08	–	0.45	–	0.54	–	0.42	0.07	0.41	0.21	−0.01	–	–	–	–	0.74	–	–	*s*-rich
N5286-1729G	4881	2.08	1.68	−1.71	0.03	0.32	0.43	0.36	0.51	0.36	0.59	0.03	0.47	0.09	−0.01	–	0.47	–	–	0.88	1.00	0.05	*s*-rich
N5286-1687G	4441	1.14	1.92	−1.84	0.03	0.15	0.36	0.06	0.41	0.07	0.31	0.03	0.29	0.07	0.07	0.04	0.24	0.04	0.13	0.15	0.13	0.08	*s*-poor
N5286-5541G	4596	1.39	1.85	−1.81	0.03	0.48	−0.12	–	−0.07	–	0.29	0.04	0.35	0.12	0.00	0.03	0.33	0.11	0.05	0.33	0.11	–	*s*-poor
N5286-1737G	4688	1.62	1.80	−1.88	0.03	0.18	0.43	0.12	0.50	0.12	0.39	0.02	0.37	0.11	0.03	0.04	0.33	0.13	0.06	0.02	0.25	–	*s*-poor
N5286-1537G	4963	2.16	1.68	−1.90	0.04	–	–	–	–	–	0.49	0.07	0.43	0.13	0.10	–	–	0.29	–	0.12	–	–	*s*-poor
N5286-5191G	5196	2.12	1.70	−1.81	0.04	0.68	0.37	–	0.46	–	0.25	–	0.64	–	0.00	–	0.29	–	–	0.58	–	–	*s*-poor
N5286-1567G	4421	1.06	1.94	−1.83	0.04	0.41	0.11	0.11	0.15	0.13	0.32	0.07	0.28	0.08	0.02	0.06	0.29	0.10	0.14	0.07	0.14	0.01	*s*-poor
N5286-1147G	4660	1.54	1.82	−1.84	0.03	–	0.20	0.12	0.26	0.13	0.32	0.03	0.37	0.12	0.03	0.00	0.34	0.12	0.03	−0.16	0.14	0.04	*s*-poor
N5286-1659G	5019	2.19	1.65	−1.65	0.02	0.29	0.36	–	0.45	–	0.35	0.08	0.47	0.15	−0.05	–	0.29	–	–	1.02	0.82	–	*s*-rich
N5286-1047G	4840	1.81	1.75	−1.76	0.03	0.23	0.21	–	0.28	–	0.33	0.06	0.40	0.16	0.00	–	0.24	0.04	0.11	−0.02	–	–	*s*-poor
N5286-1557G	5088	2.43	1.61	−1.77	0.03	–	–	–	–	–	0.48	–	0.46	0.12	−0.14	–	0.22	–	–	0.54	–	–	*s*-poor
N5286-1227G	5092	2.32	1.64	−1.78	0.06	–	–	–	–	–	0.45	–	0.43	0.14	−0.17	–	0.41	–	–	0.37	–	–	*s*-poor
N5286-1599G	5020	2.17	1.65	−1.61	0.03	–	0.50	0.06	0.58	0.05	0.52	0.04	0.48	0.15	−0.06	–	–	0.21	–	1.03	0.92	–	*s*-rich
N5286-1369G	4813	1.77	1.73	−1.59	0.03	–	0.42	0.31	0.49	0.32	0.41	0.07	0.50	0.11	−0.08	–	0.34	0.14	0.00	1.20	1.13	0.15	*s*-rich
N5286-1529G	5140	2.46	1.58	−1.53	0.05	–	0.56	–	0.65	–	0.48	0.02	0.60	0.18	−0.09	–	0.42	–	–	1.35	1.07	–	*s*-rich
N5286-947G	4921	2.15	1.68	−1.88	0.03	–	−0.01	–	0.06	–	0.36	–	0.56	0.35	0.22	–	0.42	–	–	0.15	–	–	*s*-poor
N5286-1237G	5042	2.27	1.66	−1.88	0.02	0.79	–	–	–	–	0.67	–	0.54	0.15	0.11	–	0.45	–	–	0.29	–	–	*s*-poor
N5286-827G	5075	2.43	1.60	−1.65	0.03	–	–	–	–	–	0.59	–	0.31	0.12	−0.22	–	0.13	–	–	0.03	–	–	*s*-poor
N5286-1017G	5100	2.26	1.62	−1.56	0.04	–	0.32	–	0.41	–	0.48	0.13	0.28	0.33	−0.06	–	0.19	–	–	−0.03	–	–	*s*-poor
N5286-1747G	4897	1.89	1.73	−1.73	0.03	0.43	0.37	0.27	0.45	0.29	0.38	0.10	0.38	0.13	0.04	–	0.37	0.12	0.08	0.09	–	–	*s*-poor
N5286-996G	4959	2.08	1.69	−1.82	0.03	–	0.50	–	0.59	–	0.32	0.02	0.42	0.16	−0.02	–	0.28	–	–	0.25	–	–	*s*-poor
N5286-1649G	4777	1.52	1.81	−1.62	0.03	0.06	0.34	0.00	0.41	0.00	0.34	0.04	0.39	0.12	−0.09	–	0.43	0.11	0.06	0.54	0.60	0.07	*s*-rich
N5286-587G	4714	1.51	1.81	−1.64	0.03	0.40	−0.31	–	−0.26	–	0.34	0.10	0.34	0.16	−0.05	–	0.25	0.02	0.01	0.60	0.43	–	*s*-rich
N5286-29G	4963	2.22	1.64	−1.65	0.02	–	–	–	–	–	0.36	0.06	0.43	0.14	−0.14	–	0.41	–	–	1.09	–	–	*s*-rich

Table 4 – *continued*

ID	T_{eff} (K)	log*g* (cgs)	ξ_t (km s^{-1})	[Fe/H]	±	[O/Fe]	[Na/Fe] NLTE	±	[Na/Fe] LTE	±	[Si/Fe]	±	[Ca/Fe]	±	[Sc/Fe]	±	[Ti/Fe]	[Ni/Fe]	±	[Ba/Fe]	[La/Fe]	±	group
N5286-437G	5063	2.26	1.63	−1.64	0.02	0.65	0.08	–	0.16	–	0.40	0.10	0.42	0.20	−0.10	–	0.22	–	–	0.27	–	–	*s*-poor
N5286-17G	4966	2.16	1.67	−1.76	0.03	–	0.24	–	0.32	–	0.52	–	0.41	0.18	−0.13	–	0.31	0.29	–	−0.07	–	–	*s*-poor
N5286-719G	4978	2.14	1.67	−1.71	0.03	0.80	0.21	–	0.29	–	0.41	0.23	0.41	0.14	0.05	–	0.46	–	–	1.19	–	–	*s*-rich
N5286-169G	4990	2.24	1.64	−1.72	0.03	–	0.19	–	0.27	–	0.42	0.06	0.45	0.13	−0.05	–	0.49	–	–	0.71	–	–	*s*-rich
N5286-07G	4978	2.15	1.68	−1.83	0.04	0.33	–	–	–	–	0.47	0.34	0.28	0.12	0.03	–	0.19	–	–	0.07	–	–	*s*-poor
N5286-289G	5158	2.30	1.60	−1.47	0.04	0.18	0.21	–	0.30	–	0.45	0.08	0.48	0.25	−0.01	–	0.34	–	–	0.63	–	–	*s*-rich
N5286-379G	4887	1.93	1.70	−1.58	0.03	0.05	0.31	–	0.39	–	0.36	0.07	0.42	0.12	−0.08	–	0.37	0.13	0.02	1.26	1.20	0.09	*s*-rich
N5286-509G	4881	1.94	1.71	−1.69	0.03	0.52	−0.06	–	0.01	–	0.36	0.07	0.42	0.12	−0.02	–	0.33	0.18	0.01	0.85	0.87	–	*s*-rich
N5286-157G	5118	2.42	1.62	−1.79	0.04	–	–	–	–	–	–	–	0.47	0.15	−0.14	–	–	–	–	0.14	–	–	*s*-poor
N5286-707G	5153	2.42	1.61	−1.71	0.04	–	0.34	–	0.43	–	–	–	0.46	0.17	−0.11	–	0.34	–	–	0.10	–	–	*s*-poor
N5286-537G	4838	1.85	1.74	−1.79	0.02	–	0.32	–	0.40	–	0.29	0.05	0.37	0.13	0.06	–	0.22	0.17	–	0.33	–	–	*s*-poor
N5286-207G	5177	2.45	1.59	−1.59	0.04	–	–	–	–	–	0.39	–	0.42	0.30	–	–	–	–	–	0.16	–	–	*s*-poor

spectroscopic T_{eff} and log*g* are lower than the photometric ones. Neutral iron abundances are more sensitive to temperature variations (see Tables 6 and 7); so a systematic difference of ∼100 K, such as that estimated in Section 3, can explain the difference found in the mean Fe abundances from GIRAFFE and UVES data. We remark here that we are mostly interested in the internal variations in chemical abundances present in the cluster. We are aware of systematics in the abundances derived from GIRAFFE and UVES, which are due in part to the systematics in atmospheric parameters, but also to the different transitions used for the two data sets, as UVES spectra span a significantly wider range in wavelength.

A summary of our elemental abundance results is shown in Figs 4 and 5 for GIRAFFE and UVES, respectively. We anticipate here that in these plots, our abundance results are best represented by dividing the two samples of stars into different groups, having different abundance patterns in *n*-capture elements and overall metallicity. In the next few subsections, we consider and discuss all the abundance trends we observe in NGC 5286, starting with the *n*-capture process elements.

5.1 The overall metallicity and neutron-capture elements

Fig. 4 clearly suggests that the chemical elements with the largest internal variations in NGC 5286 are the two *n*-capture elements Ba and La (see the box representative of the entire GIRAFFE sample represented in black). Expected observational errors, listed in Table 7, cannot account for the large internal variations observed in both these elements. Although both Ba and La are expected to be produced mostly by *s*-process in the Solar system, their production can be influenced by the *r*-process at low metallicity (e.g. Sneden, Cowan & Gallino 2008). However, we will refer to them as *s*-process elements because results from UVES suggest that the enrichment in this object has been due primarily to material that has undergone *s*-process nucleosynthesis (see the discussion below in this section).

The abundance patterns of Ba and La are clearer when we consider how they vary with the overall metallicity. Indeed, a visual inspection of [Ba/Fe] and [La/Fe] as a function of [Fe/H], represented in Fig. 6, immediately suggests a complex chemical pattern: overall there is an increase in [Ba/Fe] and [La/Fe] as a function of [Fe/H], with one group of stars showing higher Ba and Fe; stars with lower [Ba/Fe] appear to span a larger range in metallicity.

On the basis of the position of our stars analysed with GIRAFFE in the [Ba/Fe] versus [Fe/H] plane, we selected two different groups of stars (as plotted in Fig. 6). Because of the observed variations in Ba (and other *s*-elements as discussed below) and Fe we will refer to our populations as: (i) *s*-rich/Fe-rich for the stars with both higher *s* and Fe, selected as the stars with [Fe/H] > -1.73 and [Ba/Fe] > 0.50 (red triangles); (ii) *s*-poor/Fe-poor are all the other stars, having lower *s* and, on average, lower Fe content (blue circles). The difference in the chemical composition of these identified stellar groups can be evaluated by their mean abundances listed in Table 8. The mean [Ba/Fe] of the *s*-rich/Fe-rich group is a factor of 5 higher. Lanthanum abundances confirm the presence of both a *s*-poor/Fe-poor and a *s*-rich/Fe-rich group of stars in NGC 5286, with the second having an overabundance in [La/Fe], similar to that present in [Ba/Fe].

The *s*-rich/Fe-rich stars show larger dispersions in both Ba and La. As listed in Table 8, the rms values for the *s*-poor/Fe-poor stars are $\sigma_{[Ba/Fe]} = 0.19$ dex and $\sigma_{[La/Fe]} = 0.03$ dex, both significantly lower than those of the *s*-rich/Fe-rich stars, that are $\sigma_{[Ba/Fe]} =$

Table 5. Adopted temperatures ($T_{\rm eff}$ [K]), surface gravities (log$g$ [cgs]), microturbolences ($\xi_{\rm t}$ [km s^{-1}]), metallicities (Fe I) and chemical abundances ratios for the stars observed with UVES.

ID	$T_{\rm eff}$	log$g$	$\xi_{\rm t}$	Fe I	±	Fe II	±	O	Na	±	Mg	±	Al	±	Si	±
1219	4600	1.20	1.90	−1.93	0.02	−1.87	0.02	+0.47	0.33	0.04	0.68	0.26	0.52	0.05	0.36	0.05
1439	4750	1.70	1.71	−1.70	0.02	−1.66	0.05	+0.55	0.22	0.04	0.47	0.19	0.30	0.00	0.50	0.00
859	4300	0.85	1.98	−1.67	0.02	−1.62	0.03	+0.40	0.53	0.04	0.52	0.25	0.77	0.05	0.66	0.20
1309	4690	1.50	1.71	−1.73	0.02	−1.68	0.02	+0.30	0.34	0.03	0.37	0.17	0.88	0.07	0.22	0.16
579	4570	1.05	1.85	−1.92	0.03	−1.88	0.04	–	0.30	0.01	0.59	0.25	0.50	0.00	0.50	0.00
1339	4660	1.50	1.90	−1.72	0.02	−1.68	0.03	+0.29	0.58	0.02	0.63	0.22	0.65	0.10	0.40	0.09
177	4590	1.25	2.00	−1.92	0.02	−1.88	0.03	+0.68	−0.08	0.05	0.63	0.26	0.15	0.30	0.25	0.09

ID	Ca	±	Sc II	±	Ti I	±	Ti II	±	V	±	Cr	±
1219	0.34	0.04	0.06	0.07	0.30	0.04	0.27	0.10	0.01	0.02	−0.06	0.12
1439	0.29	0.04	0.13	0.05	0.46	0.15	0.21	0.10	0.25	0.00	−0.17	0.09
859	0.40	0.02	0.18	0.09	0.58	0.18	0.15	0.23	0.14	0.06	0.39	0.16
1309	0.27	0.04	0.14	0.08	0.24	0.03	0.37	0.20	−0.12	–	−0.12	0.06
579	0.29	0.05	−0.01	0.06	0.34	0.06	0.13	0.18	–	–	−0.17	0.00
1339	0.38	0.04	0.11	0.07	0.37	0.06	0.21	0.01	–	–	−0.01	0.08
177	0.24	0.04	0.06	0.04	0.22	0.07	0.20	0.11	0.17	0.27	−0.20	0.01

ID	Mn	±	Co	±	Ni	±	Cu	±	Zn	±	Y II	±	Zr II	±
1219	−0.40	0.04	−0.08	0.15	0.00	0.04	−0.57	–	0.11	–	0.01	0.12	0.10	–
1439	−0.48	0.05	0.25	–	−0.02	0.05	−0.55	–	0.13	–	0.70	0.06	0.55	–
859	−0.45	0.04	0.07	0.06	0.04	0.05	−0.36	0.07	0.30	–	0.42	0.05	0.41	–
1309	−0.43	0.04	0.21	0.18	−0.05	0.04	−0.67	–	0.07	–	0.06	0.11	0.25	–
579	−0.45	0.04	–	–	−0.04	0.04	−0.64	–	0.37	–	−0.07	0.08	0.20	–
1339	−0.40	0.05	0.06	0.07	0.02	0.04	−0.35	0.11	0.56	–	0.58	0.07	0.73	–
177	−0.45	0.06	0.04	–	−0.05	0.04	−0.58	–	0.10	–	−0.07	0.06	0.20	–

ID	Ba II	±	La II	±	Ce II	±	Pr II	±	Nd II	±	Eu II	±
1219	0.06	0.06	0.30	0.00	0.20	–	0.40	–	0.24	–	0.42	–
1439	0.74	0.06	0.72	0.04	0.54	–	0.50	–	0.54	–	–	–
859	0.73	0.09	0.82	0.07	0.65	0.01	0.59	0.02	0.72	0.02	0.25	0.10
1309	0.22	0.05	0.43	0.04	0.07	–	–	–	0.30	–	0.29	–
579	0.02	0.05	0.25	0.10	–	–	–	–	0.11	–	0.36	0.07
1339	0.88	0.03	1.01	0.07	0.93	0.06	0.78	0.08	0.89	0.04	0.28	–
177	0.02	0.01	0.32	0.05	0.28	–	0.35	–	0.25	–	0.30	–

0.24 dex and $\sigma_{\rm [La/Fe]} = 0.23$ dex. We note that the chemical content of La has been inferred only for a subsample of stars (eight *s*-poor/Fe-poor and 13 *s*-rich/Fe-rich as selected in the [Ba/Fe]-[Fe/H] plane) due to the fact that La lines are much weaker than the Ba line, and has been possible only for the higher S/N spectra. In particular, the mean and rms values of the La content for the eight GIRAFFE *s*-poor/Fe-poor stars may not be representative, as we cannot exclude stars with lower contents difficult to be inferred from our limited S/N data.

The mean difference in Fe between the *s*-rich and the *s*-poor stars is $\overline{\rm [Fe/H]}_{s-\rm rich} - \overline{\rm [Fe/H]}_{s-\rm poor} = +0.14 \pm 0.03$ dex, i.e. a difference of a factor of ∼1.4, with a significance at the $\sim 4.5\sigma$ level (Table 8). *s*-poor/Fe-poor stars have a larger scatter in [Fe/H], that is $\sigma_{\rm [Fe/H]} = 0.09$, to be compared with the value obtained for the *s*-rich/Fe-rich stars $\sigma_{\rm [Fe/H]} = 0.06$ dex. Fig. 4 summarizes the chemical abundances in the various analysed elements obtained from GIRAFFE data for the total (black), *s*-poor/Fe-poor and *s*-rich/Fe-rich stellar components of NGC 5286. We note that the two AGB observed with GIRAFFE both belong to the *s*-poor/Fe-poor group.

Having identified the main stellar groups by means of the large sample available from GIRAFFE data, we were able to better chemically characterize them by using the higher-resolution and larger spectral range of the UVES sample. Indeed, although the UVES sample is composed of only seven RGBs, all these stars are probable cluster members, as suggested both by RVs and proper motions (see Sections 2.1 and 2.2). The UVES sample was carefully chosen to ensure that stars on both RGBs were selected to allow us to conduct a more detailed chemical characterization.

From UVES, we infer chemical abundances of many *n*-capture elements, including Y, Zr, Ba, La, Ce, Pr, Nd, and Eu. Fig. 5 suggests that these elements, excluding Eu, are those displaying the higher dispersions. From the UVES results the separation between the *s*-poor stars and the *s*-rich stars is clearer, making the identification of the two *s*-groups straightforward.

In Fig. 7, we show the abundances of all *n*-capture elements relative to iron as a function of [Fe/H] for the UVES sample. The UVES stars appear to cluster around two different values in all these plots: at a lower and at a higher level of Fe and *n*-capture element contents. One star in our UVES sample has relatively high Fe, but lower content in *n*-capture elements. Summarizing, the UVES sample comprises of three *s*-poor/Fe-poor stars (blue in Fig. 7), three *s*-rich/Fe-rich stars (red in Fig. 7) and one star that apparently stands away from the two main component, being *s*-poor, but higher Fe relatively to the *s*-poor/Fe-poor group. The presence of one UVES star with low *s*-elements, and relatively Fe-rich may suggest that a minor stellar component, that is Fe-rich and *s*-poor may be present in NGC 5286. We note that this would confirm the higher dispersion in [Fe/H] that we found for the *s*-poor/Fe-poor group in the GIRAFFE sample. The possible presence of this minor stellar component will be discussed in more details in Section 5.5.

Table 6. Sensitivity of the derived UVES abundances to the uncertainties in atmospheric parameters and uncertainties due to the errors in the EWs measurements or in the χ-square fitting procedure. The total internal uncertainty ($\sigma_{\rm total}$) has been obtained by considering the errors in atmospheric parameters, the covariance terms, and the EWs/fit terms.

	$\Delta T_{\rm eff}$ $\pm$ 50 K	Δlog$g$ $\pm$0.16	$\Delta\xi_{\rm t}$ $\pm$0.11 km s^{-1}	Δ[A/H] $\pm$0.05 dex	$\sigma_{\rm EWs/fit}$	$\sigma_{\rm total}$
[O/Fe]	∓0.03	±0.07	±0.04	∓0.00	±0.01/ ±0.03	±0.05/ ±0.06
[Na/Fe]	∓0.01	∓0.01	±0.03	∓0.01	±0.01/ ±0.02	±0.04
[Mg/Fe]	∓0.02	∓0.01	±0.01	∓0.01	±0.06	±0.06
[Al/Fe]	∓0.01	±0.00	±0.04	∓0.01	±0.03/ ±0.07	±0.05/ ±0.08
[Si/Fe]	∓0.05	±0.02	±0.04	∓0.00	±0.07	±0.08
[Ca/Fe]	±0.00	∓0.01	±0.00	∓0.01	±0.02	±0.02
[Sc/Fe] II	∓0.06	±0.07	±0.02	±0.01	±0.04	±0.03
[Ti/Fe] I	±0.03	∓0.01	±0.02	∓0.01	±0.03	±0.05
[Ti/Fe] II	∓0.07	±0.07	±0.01	±0.01	±0.04	±0.03
[V/Fe]	±0.00	±0.00	±0.04	±0.00	±0.08	±0.09
[Cr/Fe]	±0.03	∓0.01	±0.00	∓0.01	±0.06	±0.06
[Mn/Fe]	±0.05	∓0.01	±0.04	∓0.02	±0.01/±0.02	±0.07
[Fe/H] I	±0.06	∓0.01	∓0.04	∓0.01	±0.01	±0.05
[Fe/H] II	∓0.03	±0.06	∓0.02	±0.01	±0.03	±0.05
[Co/Fe]	∓0.01	±0.01	±0.04	±0.00	±0.11	±0.12
[Ni/Fe]	±0.00	±0.01	±0.03	±0.00	±0.03	±0.04
[Cu/Fe]	±0.02	±0.00	±0.03	±0.00	±0.01/±0.04	±/0.04±0.06
[Zn/Fe]	∓0.07	±0.04	±0.01	±0.01	±0.08	±0.08
[Y/Fe] II	∓0.05	±0.07	±0.01	±0.01	±0.06	±0.06
[Zr/Fe] II	∓0.05	±0.06	±0.03	±0.01	±0.02/±0.08	±0.02/±0.08
[Ba/Fe] II	∓0.02	±0.03	∓0.08	±0.00	±0.04	±0.09
[La/Fe] II	∓0.02	±0.06	∓0.02	±0.00	±0.01	±0.04
[Ce/Fe] II	∓0.05	±0.02	±0.05	±0.01	±0.09	±0.10
[Pr/Fe] II	∓0.05	±0.06	±0.04	±0.02	±0.02/±0.07	±0.03/±0.07
[Nd/Fe] II	∓0.05	±0.02	±0.05	±0.01	±0.07	±0.08
[Eu/Fe] II	∓0.05	±0.08	±0.04	±0.01	±0.02/±0.08	±0.04/±0.09

Table 7. Sensitivity of the derived GIRAFFE abundances to the uncertainties in atmospheric parameters and uncertainties due to the errors in the χ-square fitting procedure. The total internal uncertainty ($\sigma_{\rm total}$) has been obtained by considering the errors in atmospheric parameters, the covariance terms, and the fit terms.

	$\Delta T_{\rm eff}$ $\pm$50 K	Δlog$g$ $\pm$0.20	$\Delta\xi_{\rm t}$ $\pm$0.20 km s^{-1}	Δ[A/H] $\pm$0.05 dex	$\sigma_{\rm fit}$	$\sigma_{\rm total}$
[O/Fe]	∓0.03	±0.09	±0.04	±0.00	±0.03/±0.06	±0.05/±0.08
[Na/Fe]	∓0.02	∓0.02	±0.04	±0.03	±0.05/±0.09	±0.07/±0.10
[Si/Fe]	∓0.02	±0.02	±0.06	±0.01	±0.02/±0.03	±0.04/±0.05
[Ca/Fe]	±0.00	∓0.04	∓0.03	∓0.01	±0.02	±0.02
[Sc/Fe] II	∓0.03	±0.07	±0.05	±0.03	±0.02/±0.04	±0.04/±0.05
[Ti/Fe]	±0.02	∓0.03	±0.03	∓0.01	±0.03/±0.04	±0.04/±0.05
[Fe/H]	±0.07	±0.02	∓0.02	±0.01	±0.01/±0.02	±0.07/±0.08
[Ni/Fe]	±0.00	∓0.01	±0.03	±0.00	±0.03/±0.04	±0.04/±0.05
[Ba/Fe] II	∓0.04	±0.03	∓0.10	±0.01	±0.07	±0.15
[La/Fe] II	∓0.02	±0.05	±0.04	±0.00	±0.04/±0.07	±0.06/±0.09

The average UVES abundances obtained for the *s*-poor/Fe-poor and the *s*-rich/Fe-rich group, excluding the *s*-poor star with relatively high Fe, are listed in Table 9. The differences between the mean content in *n*-capture elements between the *s*-poor/Fe-poor and the *s*-rich/Fe-rich exceed a 3σ level for the abundance ratios of Y ($\gtrsim$4.5σ), Ba ($\gtrsim$9σ), La ($\gtrsim$4σ). The mean abundance of Zr, Ce and Nd over Fe are also higher for the *s*-rich/Fe-rich stars at a level of $\sim$2.5σ. Praseodymium is mildly enhanced in the *s*-rich/Fe-rich stars too, but the difference with the *s*-poor/Fe-poor group is at an $\sim$1.7σ level. [Eu/Fe] reverses the general trend displayed by the other *n*-capture elements, as it is slightly lower in the *s*-rich/Fe-rich stars. However, the difference in [Eu/Fe] is only <0.10 dex, and it is significant at an $\sim$1.5σ level. To detect a possible small difference in this element (if any) higher quality data (in terms of resolution and S/N) is required. We note here that a similar (low significance) small difference in Eu in the same sense has been observed in M 22 (Marino et al. 2011b). For the moment, we assume that, at odds with the other *n*-capture elements, Eu does not show any strong evidence for internal increase in NGC 5286.

From UVES data, the [Ba/Fe] abundance is almost a factor of 6 higher in the *s*-rich/Fe-rich stars, similarly to that inferred from GIRAFFE data. Lanthanum abundance is a factor of

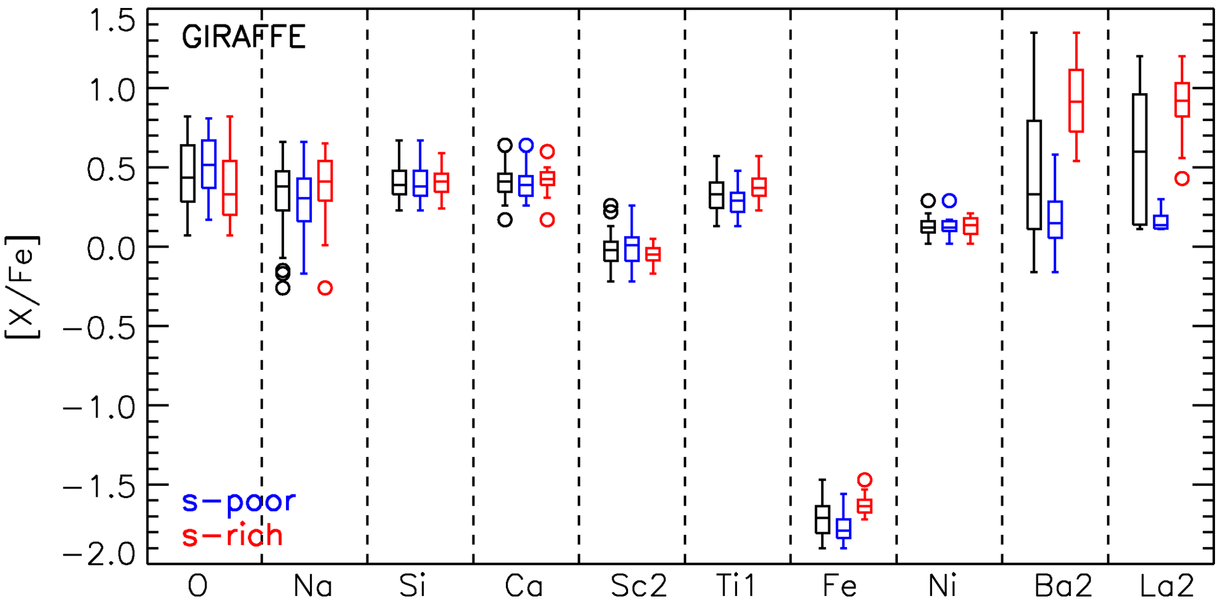

Figure 4. Box and whisker plot of the Fe-poor/*s*-poor (blue) and the Fe-rich/*s*-rich (red) abundances observed with GIRAFFE. The black box includes all the stars of NGC 5286 stars analysed with GIRAFFE. For the non-Fe species, their [X/Fe] relative abundances are shown, for Fe we plotted [Fe/H]. For a given elements, the box represents the interquartile range (middle 50 per cent of the data) and the median is indicated by the horizontal line. The vertical tails extending from the boxes indicate the total range of abundances determined for each element, excluding outliers. Outliers (those 1.5 times the interquartile range) are denoted by open circles.

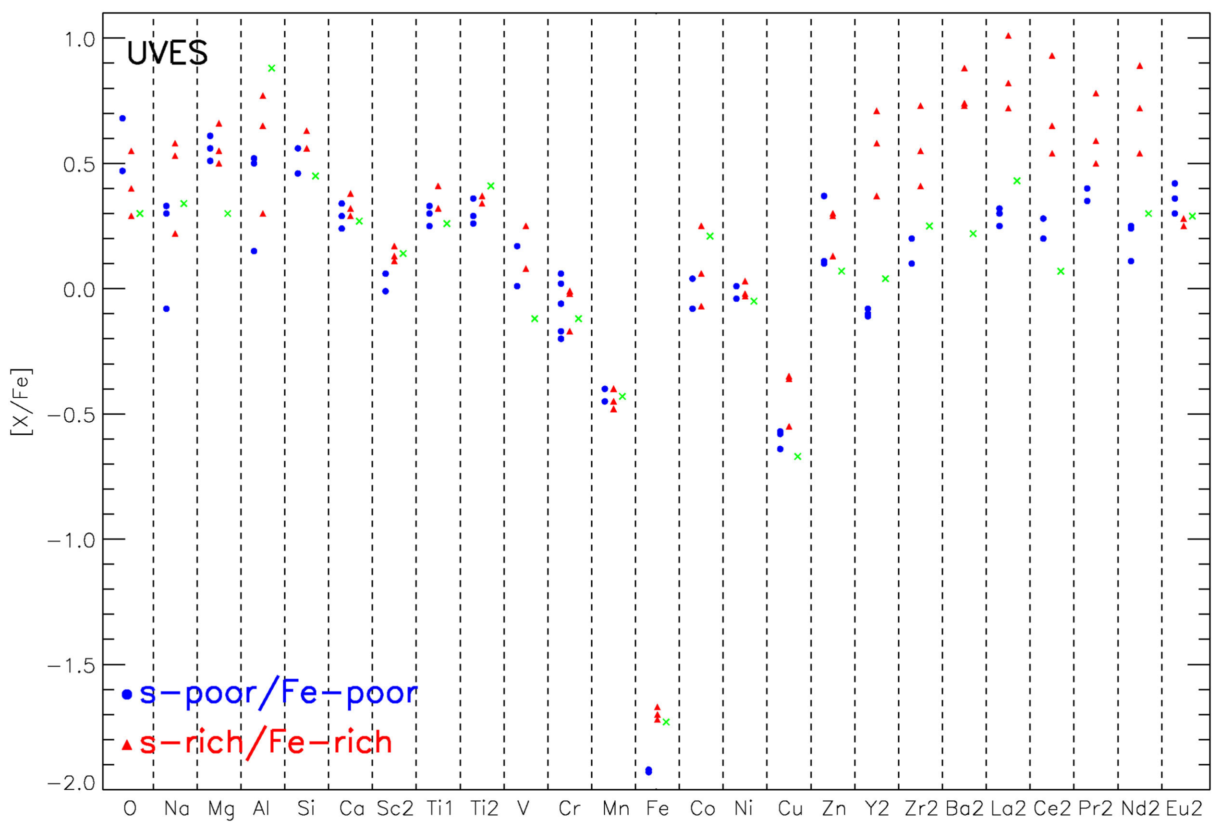

Figure 5. Summary of the abundance results obtained from UVES spectra. For the non-Fe species, their [X/Fe] relative abundances are plotted, for Fe we plotted [Fe/H]. Filled red triangles are used for stars with *s*-process and Fe enhancements, filled blue circles are for stars without such enhancements, while the green cross shows the abundances for the star 1309U, with Fe-rich/*s*-poor composition (see Section 5 for definitions of these stellar groups).

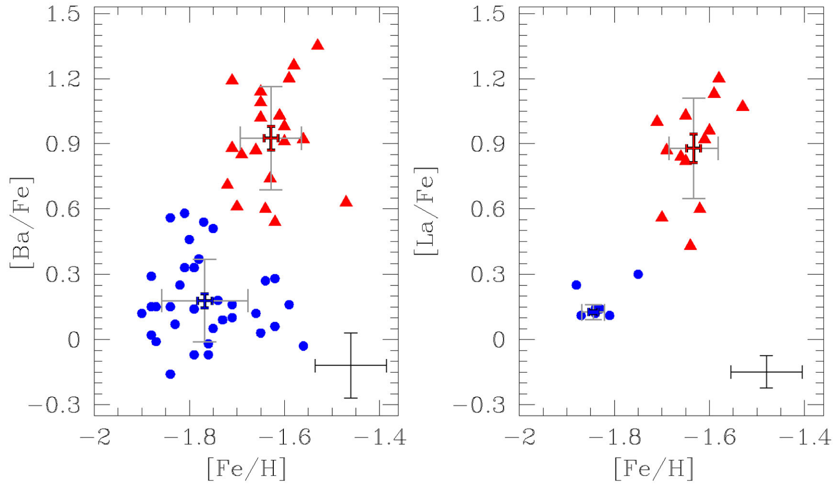

Figure 6. Abundance ratios [Ba/Fe] and [La/Fe] as functions of [Fe/H] derived from the GIRAFFE sample. In each panel, blue circles represent *s*-poor/Fe-poor stars, red triangles represent *s*-rich/Fe-rich stars. For each stellar group we show the average values, with associated dispersions (grey bars) and errors (blue and red bars). The typical uncertainty (from Table 7) associated with single measurements is plotted on the bottom-right corner.

Table 8. Mean GIRAFFE abundances for the total number of analysed stars, the *s*-rich, the *s*-poor groups. The averaged and rms values and the associated errors, have been computed by excluding values deviating more than 3 × 68th percentile from the median. The total number of analysed stars for each group is also listed.

Abundance	Mean	±	σ	#	Mean	±	σ	#	Mean	±	σ	#
	All GIRAFFE stars				*s*-poor				*s*-rich			
[O/Fe]	+0.44	0.04	0.22	28	+0.49	0.05	0.20	18	+0.34	0.08	0.23	10
[Na/Fe]	+0.34	0.04	0.21	39	+0.29	0.05	0.22	22	+0.41	0.05	0.18	17
[Si/Fe]	+0.40	0.01	0.09	53	+0.40	0.02	0.11	33	+0.41	0.02	0.08	20
[Ca/Fe]	+0.41	0.01	0.09	55	+0.40	0.02	0.10	35	+0.42	0.01	0.05	20
[Sc/Fe]	−0.03	0.01	0.08	54	−0.01	0.02	0.11	34	−0.04	0.01	0.05	20
[Ti/Fe] I	+0.33	0.02	0.10	44	+0.30	0.02	0.09	27	+0.38	0.02	0.09	17
[Fe/H]	−1.72	0.01	0.11	55	−1.77	0.02	0.09	35	−1.63	0.02	0.06	20
[Ni/Fe]	+0.13	0.01	0.07	27	+0.11	0.01	0.05	17	+0.13	0.02	0.07	10
[Ba/Fe] II	+0.45	0.06	0.42	55	+0.18	0.03	0.19	35	+0.93	0.05	0.24	20
[La/Fe] II	+0.61	0.09	0.40	21	+0.14	0.01	0.03	8	+0.88	0.07	0.23	13

∼4 higher in the *s*-rich/Fe-rich group. UVES data also confirm the difference in metallicity among different stellar groups, with the *s*-rich/Fe-rich stars again being enhanced in Fe by a factor of ∼1.5.

The histogram distribution of the [Fe/H] values obtained from GIRAFFE and UVES data is represented in Fig. 8. These Fe distributions alone suggest the presence of a genuine Fe spread in NGC 5286. The kernel-density distributions corresponding to the observed data strongly differ from the distribution for a mono-metallic GCs expected from our observational errors. The probability that the *s*-poor and *s*-rich stars in the GIRAFFE sample come from the same parent distribution is $\sim10^{-7}$, as verified by computing a Kolmogorov–Smirnov test.

In Fig. 9, we show some Ba, Ce, and Nd transitions in stars with similar atmospheric parameters but very different derived *s*-elements chemical contents. The *s*-rich GIRAFFE star 969G clearly has a much stronger Ba line λ6141 Å than does the *s*-poor GIRAFFE star 1237G, and the same is observed in the pair of UVES stars 1339U and 1219U. Inspection of other contrasting pairs of stars and other spectral lines yields the same conclusion. The average chemical abundances for the *s*-poor and the *s*-rich stellar groups of NGC 5286 are listed in Tables 8 and 9, for GIRAFFE and UVES, respectively.

5.2 The *p*-capture elements and light-elements (anti)correlations

The elements we have inferred that can be affected by proton-capture (*p*-capture) reactions include O and Na analysed from both UVES and GIRAFFE, and Mg and Al, available only for UVES data. All of these elements show internal dispersions larger than those expected from observational errors, suggesting that NGC 5286 shares with the typical Milky Way GCs the presence of light-elements variations (see Tables 8 and 9). For most elements (including O, Na, and Al), internal dispersions remain high even when the sample is separated into *s*-poor and *s*-rich groups.

In Fig. 10, we show [Na/Fe] versus [O/Fe] (left) and versus [Si/Fe] (right) for the GIRAFFE sample. These data suggest that both the *s*-rich/Fe-rich and the *s*-poor/Fe-poor groups independently exhibit an O–Na anticorrelation. Additionally, the *s*-rich/Na-rich stars typically have higher Si content, and a subsample of the *s*-poor/Na-rich stars are also Si-richer. As shown in Fig. 11, no obvious correlations are present between O and Na with *s*-element Ba, although the mean [Na/Fe] and [O/Fe] are, respectively, higher and lower in the *s*-rich stars, but these differences have only a 1σ significance.

The smaller sample of UVES stars confirms the presence of a O–Na anticorrelation, showing also a well-defined Na–Al correlation (Fig. 12), with variations in these elements internally present

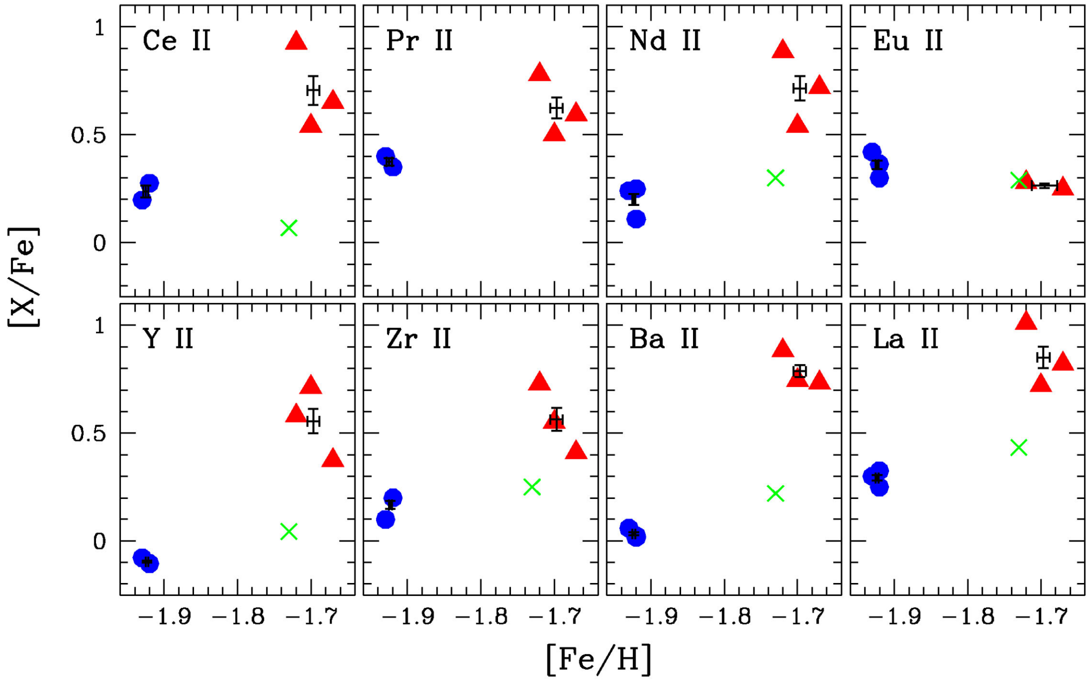

Figure 7. Summary of the abundance results for *n*-capture process elements obtained from the UVES sample. Abundance ratios of *n*-capture elements from Y to Eu relative to Fe are shown as a function of their [Fe/H] metallicities. The horizontal and vertical ranges are identical in all panels. Symbols are as in Fig. 6. For the *s*-poor/Fe-poor and *s*-rich/Fe-rich stellar groups, we show the means and associated error bars.

Table 9. Mean UVES abundances for the total number of analysed stars, the *s*-rich and the *s*-poor group.

Abundance	Mean	±	σ	#	Mean	±	σ	#	Mean	±	σ	#
	All UVES stars				*s*-poor				*s*-rich			
[O/Fe]	+0.45	0.07	0.15	6	+0.58	0.15	0.15	2	+0.41	0.09	0.13	3
[Na/Fe]	+0.32	0.09	0.22	7	+0.18	0.16	0.23	3	+0.44	0.14	0.20	3
[Mg/Fe]	+0.55	0.04	0.11	7	+0.63	0.03	0.05	3	+0.54	0.06	0.08	3
[Al/Fe]	+0.54	0.11	0.26	7	+0.39	0.15	0.21	3	+0.58	0.17	0.25	3
[Si/Fe]	+0.41	0.06	0.16	7	+0.37	0.09	0.13	3	+0.52	0.09	0.13	3
[Ca/Fe]	+0.31	0.02	0.06	7	+0.29	0.04	0.05	3	+0.36	0.04	0.05	3
[Sc2/Fe]	+0.09	0.03	0.06	7	+0.04	0.03	0.04	3	+0.14	0.02	0.03	3
[Ti1/Fe]	+0.36	0.05	0.13	7	+0.29	0.05	0.06	3	+0.47	0.07	0.10	3
[Ti2/Fe]	+0.22	0.03	0.08	7	+0.20	0.05	0.07	3	+0.19	0.02	0.03	3
[V/Fe]	+0.09	0.07	0.15	5	+0.09	0.11	0.11	2	+0.19	0.08	0.08	2
[Cr1/Fe]	−0.05	0.08	0.20	7	−0.15	0.05	0.07	3	+0.07	0.20	0.29	3
[Mn/Fe]	−0.44	0.01	0.03	7	−0.43	0.02	0.03	3	−0.44	0.03	0.04	3
[Fe/H]	−1.80	0.05	0.12	7	−1.92	0.00	0.01	3	−1.70	0.02	0.03	3
[Co/Fe]	+0.09	0.05	0.12	6	−0.02	0.09	0.09	2	+0.13	0.07	0.11	3
[Ni/Fe]	−0.01	0.01	0.04	7	−0.04	0.02	0.03	3	+0.01	0.02	0.03	3
[Cu/Fe]	−0.53	0.05	0.13	7	−0.60	0.03	0.04	3	−0.42	0.08	0.11	3
[Zn/Fe]	+0.24	0.07	0.18	7	+0.19	0.11	0.15	3	+0.33	0.15	0.22	3
[Y2/Fe]	+0.23	0.13	0.32	7	−0.04	0.03	0.05	3	+0.56	0.10	0.14	3
[Zr2/Fe]	+0.35	0.09	0.23	7	+0.17	0.04	0.06	3	+0.56	0.11	0.16	3
[Ba2/Fe]	+0.38	0.16	0.39	7	+0.03	0.02	0.02	3	+0.79	0.06	0.08	3
[La2/Fe]	+0.55	0.12	0.30	7	+0.29	0.03	0.04	3	+0.85	0.10	0.15	3
[Ce2/Fe]	+0.44	0.14	0.32	6	+0.24	0.06	0.06	2	+0.71	0.14	0.20	3
[Pr2/Fe]	+0.52	0.09	0.17	5	+0.38	0.04	0.04	2	+0.62	0.10	0.14	3
[Nd2/Fe]	+0.44	0.12	0.29	7	+0.20	0.06	0.08	3	+0.72	0.12	0.17	3
[Eu2/Fe]	+0.32	0.03	0.06	6	+0.36	0.04	0.06	3	+0.27	0.02	0.02	2

in both the *s*-groups (see upper-right panel in Fig. 12). Despite clear variations in Al, which correlates with Na, also implying a O–Al anticorrelation, there is no strong evidence for a Mg–Al anticorrelation, at least from our relatively small sample of UVES targets. We note, however, that the star with the highest Al also has the lowest Mg and low O, and possibly a larger sample of stars with Al and Mg abundances can reveal the presence of clear Mg–Al anticorrelation. For now, we can say that the possible lack of a clear Mg–Al anticorrelation does not necessarily mean that *p*-captures on Mg are ruled out. Our average abundances, as listed in Table 9, suggests that Mg

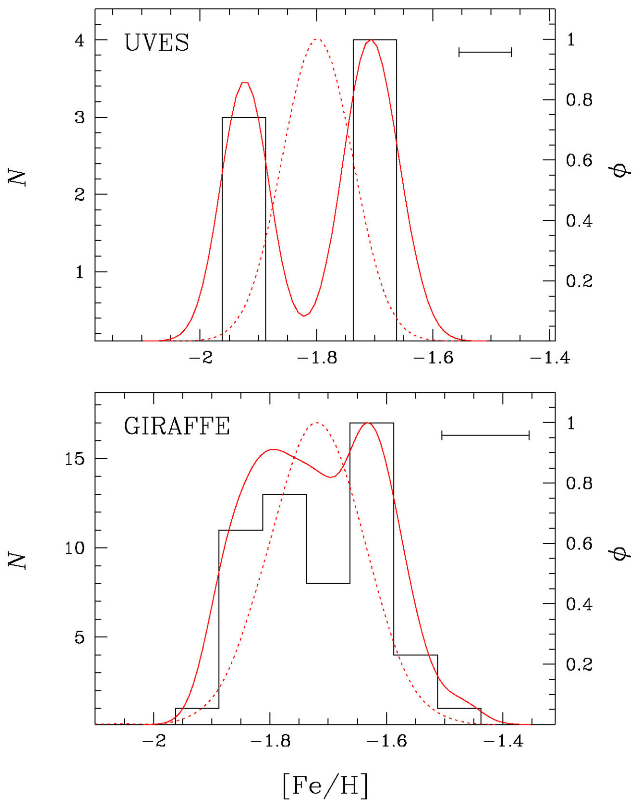

Figure 8. Histograms of [Fe/H] distribution for the GIRAFFE (lower panel) and UVES (upper panel). The measurement error in [Fe/H] is plotted in the upper-left corner. The red continuous lines are the normalized kernel density distributions of the observed metallicities, while the red dotted lines are the normalized kernel-density distributions corresponding to measurement errors only. To derive each kernel density distribution, we used a Gaussian Kernel and a dispersion equal to the measurement error.

is slightly depleted in *s*-rich stars; however we notice that, given the associated errors, this difference is marginal. If we suppose that the higher observed Mg abundances are representative of 'primordial' NGC 5286 material (that is, prior to any *p*-capture synthesis events), and if primordial Al is indicated by the lower observed Al abundances (∼0.2 dex), then for this material [Mg/Al]∼+0.4. Then, if (for example) 10 per cent of this Mg were to be converted to Al by *p*-capture in the primordial material, the resulting Al would go up by a factor of 4, nearly the range covered by our data. The 10 per cent decrease in Mg would be difficult to detect. Additionally, if the ab initio abundance of Mg contains substantial amounts of ^{25}Mg and/or ^{26}Mg, then the final Al abundance would be even larger after *p*-captures. It is worth noticing that similar weak Mg dependence on *p*-capture elements, such as Na and Al, are present also in other 'anomalous' GCs, such as ω Centauri (Norris & Da Costa 1995), M 22 (Marino et al. 2009, 2011b), and M 2 (Yong et al. 2014).

5.3 The Fe-peak elements

Chemical abundances for Fe-peak elements V, Cr, Mn, Co, Ni, and Zn relative to Fe do not show any evidence for internal variations between the two groups, exceeding a 1σ level (see Figs 4 and 5, and values listed in Tables 8 and 9). As is the case with low-metallicity field stars (Sneden, Gratton & Crocker 1991; Mishenina et al. 2002) and GCs (Simmerer et al. (2003), copper is underabundant in NGC 5286. However, [Cu/Fe] may vary slightly in concert with the *s*-process elements, being higher in the *s*-rich than the *s*-poor group by [Cu/Fe] = +0.18 ± 0.09 (Table 9). The difference among the two groups is only at a 2σ level, and, given the

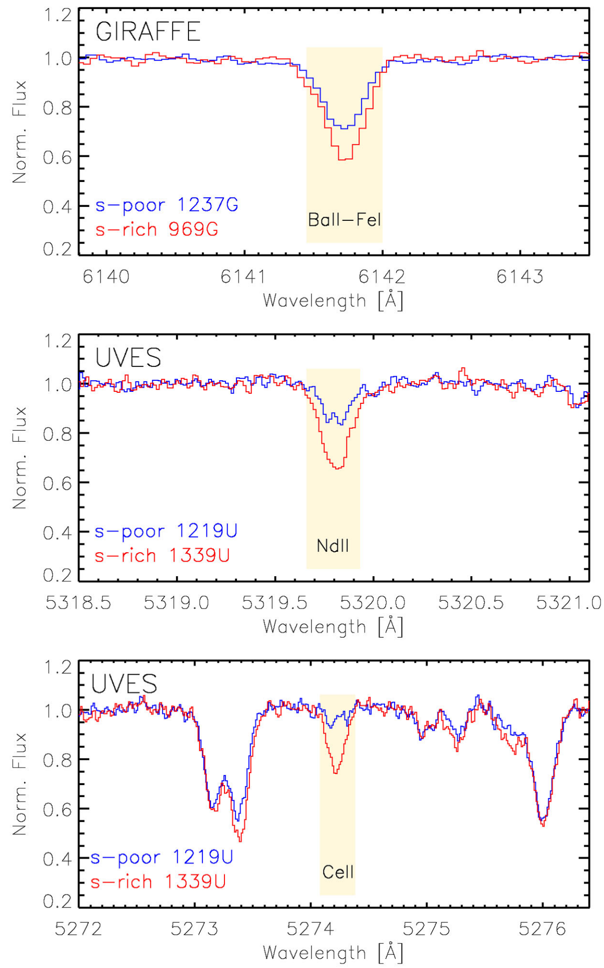

Figure 9. Observed spectra around some analysed *n*-capture transitions for two stars observed with GIRAFFE (upper panel), and two stars observed with UVES (lower panels). In each panel, we represent pairs of stars with similar atmospheric parameters, so that the difference in the represented lines (Ba, Nd, Ce) are due almost entirely to a different chemical content in these elements. The blue spectrum represents a star belonging to the *s*-poor group, the red spectrum to a star belonging to the *s*-rich one.

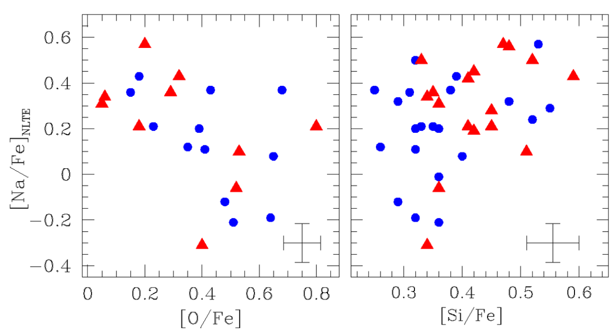

Figure 10. [Na/Fe] abundances corrected for NLTE as a function of [O/Fe] (left-hand panel) and [Si/Fe] (right-hand panel). Symbols and colours are as in Fig. 6.

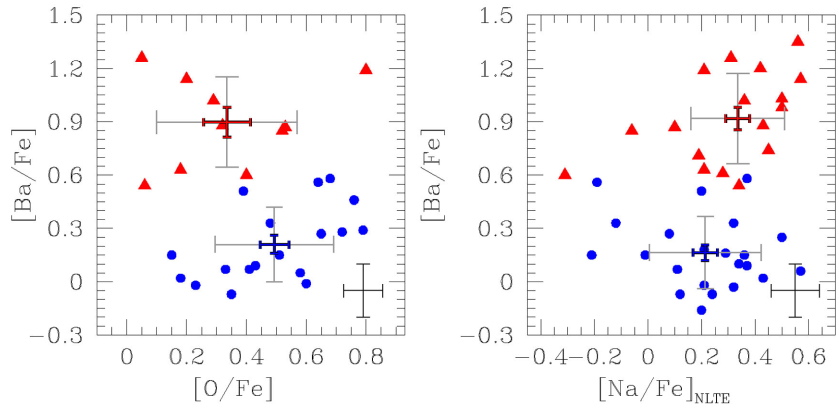

Figure 11. Abundance ratios [Ba/Fe] as functions of [O/Fe] and $[Na/Fe]_{NLTE}$ derived from the GIRAFFE sample. In each panel, blue circles represent *s*-poor/Fe-poor stars, red triangles represent *s*-rich/Fe-rich stars. For each stellar group we show the average values, with associated dispersions (grey bars) and errors (blue and red bars). The typical uncertainty (from Table 7) associated with single measurements is plotted on the bottom-right corner.

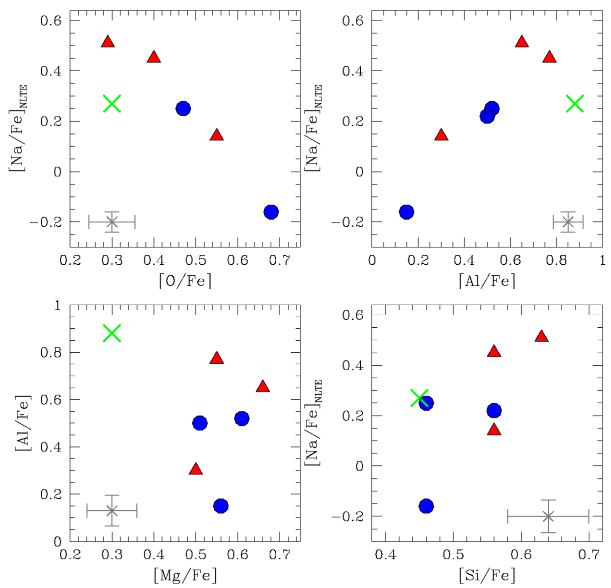

Figure 12. Abundance patterns for elements involved in hot H-burning for stars analysed with UVES spectra. The upper panels show the typical O–Na anticorrelation and a clear Na–Al correlation. Mg and Al do not show any strong evidence for anticorrelation, within observational errors (bottom-left panel); while Si is mildly correlated with Na (bottom-right panel). Error bars in the bottom corners of each panel represent estimated errors for single measurements. Symbols and colours are as in Fig. 6.

uncertainties associated with individual Cu abundance measurements and the low statistics available (three *s*-poor and three *s*-rich stars observed with UVES), interpretation of this difference should be viewed with caution.

5.4 The CMD/chemistry connection

The analysis of our ground-based photometric data shows that multiple branches (both on the RGB and the SGB) are present in the CMD of NGC 5286. Piotto et al. (2012) have used multiwavelength *HST* photometry to demonstrate that NGC 5286 hosts a broad SGB with at least two components that correspond with two main stellar populations. A bright SGB, which hosts about 86 per cent of SGB stars, and a faint-SGB component made of ∼14 per cent of stars. As discussed in Section 2.1, by using the *U* filter, we have identified a split in the RGB in the $(U - V)$ colour. The double RGB seems to merge in the broad SGB of NGC 5286, with the red-RGB connected with the faint part of the SGB, and the blue-RGB associated with the bright SGB, in close analogy with what observed in NGC 1851 and M 22 (Lee et al. 2009; Marino et al. 2011b).

Multiple SGBs and RGBs can be detected in the CMD and two-colour diagrams of most GCs only when appropriate combination of ultraviolet colours and magnitudes are used. In *anomalous* GCs, multiple SGBs are clearly visible in CMDs made with visual filters only. Furthermore, in the *U* versus $(U - V)$ CMD of anomalous GCs, the faint and the bright SGB evolve into the red and blue RGB and are made of metal/*s*-rich and metal/*s*-poor stars, respectively (e.g. Marino et al. 2012).

The location of our spectroscopic sample on the U–$(U - V)$ CMD, suggests that the two identified RGBs are populated by stars belonging to the two groups with different Fe and *s*-elements (left-hand panel of Fig. 13). Among GCs, the same behaviour observed in Fig. 13 for NGC 5286, is seen on the CMD of M 22. Similar to NGC 5286, M 22 also has a similar RGB-SGB split in the U–$(U - V)$ CMD and spectroscopy on the SGB has demonstrated that the faint SGB stars are more enriched in *s*-elements compared to bright SGB stars (Marino et al. 2012). We emphasis that the difference in the *s*-element content does not directly affect the separation of the two RGBs along the U–$(U - V)$ CMD. Additionally, the observed variation in metallicity cannot account for the relatively large separation in colour among the Fe-*s*-rich and the Fe-*s*-poor RGBs. It is tempting to speculate that internal variations in the overall C+N+O abundance, together with iron variations, are responsible for the SGB split as shown by Marino et al. (2012) for the case of M 22. The fact that the faint and the bright SGB of NGC 5286 are consistent with two stellar populations with different C+N+O has been already shown by Piotto et al. (2012) on the basis of their comparison of isochrone and *HST* photometry. Spectroscopic measurement of C, N, O in NGC 5286, together with the iron measurements provided in this paper, are mandatory to understand if the SGB and RGB morphology of this cluster can be entirely explained in terms of metallicty and C+N+O. Here, we can conclude that, as the two RGBs *evolve* from a spread SGB in the U–$(U - V)$ CMD, the SGB morphology of NGC 5286 is indirectly connected with the presence of the two stellar groups with different chemical composition: the bright SGB is composed of *s*-poor stars, and the faint SGB of *s*-rich stars.

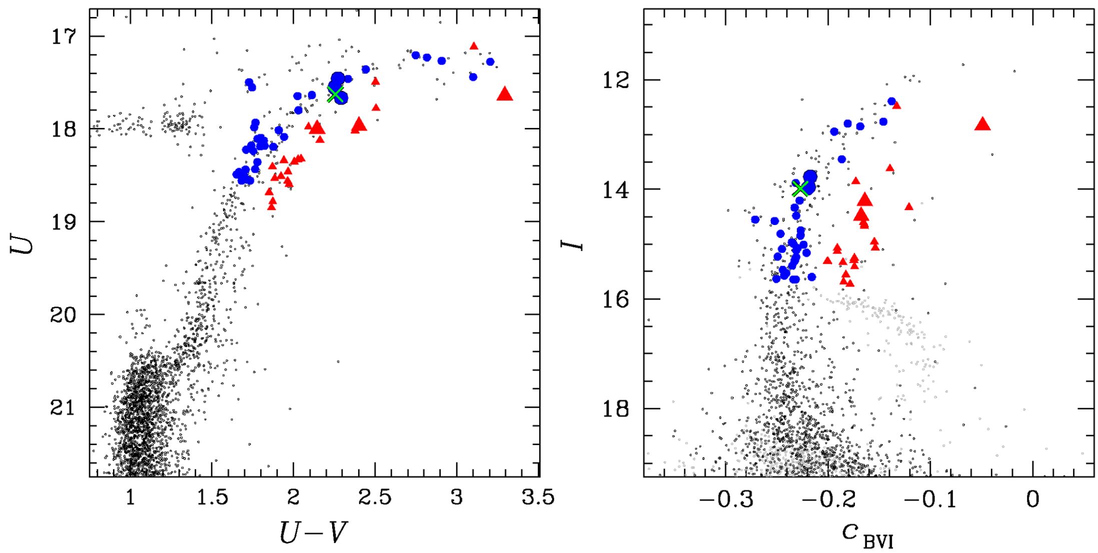

Figure 13. U–$(U-V)$ CMD (left-hand panel) and I–c_{BVI} diagram (right-hand panel) for NGC 5286, corrected for differential reddening. The grey symbols on the right-hand panel represent HB stars. Spectroscopic data are superimposed with *s*-rich/Fe-rich stars represented by red triangles, *s*-poor/Fe-poor stars by blue circles, and the *s*-poor/Fe-rich UVES star by a green cross, according with the other figures.

Previous papers have shown that a number of colours or photometric indices based on ultraviolet and far-ultraviolet photometry are very effective for detecting multiple sequences along the RGB. These include the $(U-B)$ colour (Marino et al. 2008), the Strömgren index $c_y = c_1 - (b-y)$ (Grundahl 1999; Yong et al. 2008), and the $c_{F275W,\,F336W,\,F438W} = (m_{F275W} - m_{F336W}) - (m_{F336W} - m_{F438W})$ and $c_{F336W,\,F438W,\,F814W}$ '(c_{UBI})' $= (m_{F336W} - m_{F438W}) - (m_{F438W} - m_{F814W})$ indices introduced by Milone et al. (2013) by using *HST* filters *F*275*W*, *F*336*W*∼*U*, *F*438*W*∼*B*, and *F*814*W*∼*I*. An appropriate combinations of *U*, *B*, *I* ground-based photometry can efficiently separate multiple populations with different content of nitrogen (through the CN line at ∼3300 Å) and helium (Marino et al. 2008; Milone et al. 2012b, 2013; Monelli et al. 2013).

However, since O–Na–Al (anti)correlations are present among both *s*-rich and *s*-poor stars of NGC 5286, an index that is sensitive to the light-element patterns, like the $c_{U,\,B,\,I}$ index, is not able to provide a clear separation between the two *s* and Fe groups of stars hosted in the cluster. We have defined a new photometric index based on a combination of *B*, *V*, and *I* magnitudes, $c_{BVI} = (B - V) - (V - I)$, that maximizes the separation between the *s*-poor and the *s*-rich groups of NGC 5286 (right-hand panel of Fig. 13). In contrast with the $c_{U,\,B,\,I}$ index, the newly defined $c_{B,\,V,\,I}$ index, is largely insensitive to nitrogen variations on the atmosphere of the stars and provides a clear separation between *s*-rich and *s*-poor stars of NGC 5286. This is similar to what observed in M 22, i.e. the *s*-rich and *s*-poor stars define two RGBs in the *V* versus m_1 diagram (Marino et al. 2011b).

While a difference in age may account for the SGB structure of NGC 5286, it cannot reproduce the large split seen in the c_{BVI} index (Marino et al., in preparation), and also the observed difference in metallicity is too small to cause the wide separation observed on the I–c_{BVI} diagram. As the *s*-process abundances are not directly affecting broad-band colours, this is another indication that the major cause of the observed split in the c_{BVI} is likely to be the presence of metallicity and C+N+O variations among the *s*-poor/Fe-poor and the Fe-rich/*s*-rich. Future spectroscopic investigations may be enlightening in this regard, and should prove if C+N+O variations exist in NGC 5286, further constraining the nature of the polluters.

We note here that the observed variation in the overall metallicity is not able to reproduce such a large split in $(U - V)$ and c_{BVI}. For M 22, we have demonstrated that the observed difference in C+N+O (plus the variation in metallicity) can account for the entire split SGB/RGB without any significant variation in age among the *s*-poor (bright SGB) and the *s*-rich stars (faint SGB). Even if we could not measure abundances of C and N for our stars in NGC 5286, given the similar chemical abundance and photometric patterns shared with M 22, it is tempting to speculate that internal variations in C+N+O are present also in this GC and can account (in part or totally) for its SGB split. We note that, in order to determine relative ages among the two SGB populations in NGC 5286, future studies that measure the total C+N+O of the two *s*-groups is essential.

5.5 On the possible presence of a metallicity spread in the *s*-poor/Fe-poor group

From Fig. 6, we note that although on average, the *s*-poor group is more Fe-poor than the *s*-rich group, there are some *s*-poor stars with [Fe/H] similar to the *s*-rich group. Also in the UVES sample, one star shows a similar behaviour and we preferred not to include this star in either of the two main *s*-groups. The possible presence of a minor third stellar component or a metallicity spread in the *s*-poor group warrants a detailed discussion, and we have performed additional tests to investigate whether this group is present in NGC 5286, or if the spread in [Fe/H] is merely due to observational errors.

First, we have inspected the position of these stars in the CMD. As shown in Fig. 14, we have selected a group of GIRAFFE stars, composed of seven objects, showing lower *s*-content ([Ba/Fe] < 0.40) and higher Fe ([Fe/H] >− 1.70; green crosses in the [Ba/Fe] versus [Fe/H] plane). The position of these stars in the V–$(U-V)$ CMD is shown in the left-hand panel of Fig. 14. Clearly, the main *s*-poor and *s*-rich groups define two different branches on this CMD (as discussed in Section 5.4), but the seven stars with higher Fe and lower *s*-content do not appear to define distinct branches, and their position is consistent with that of the RGB as defined by the *s*-poor stars.

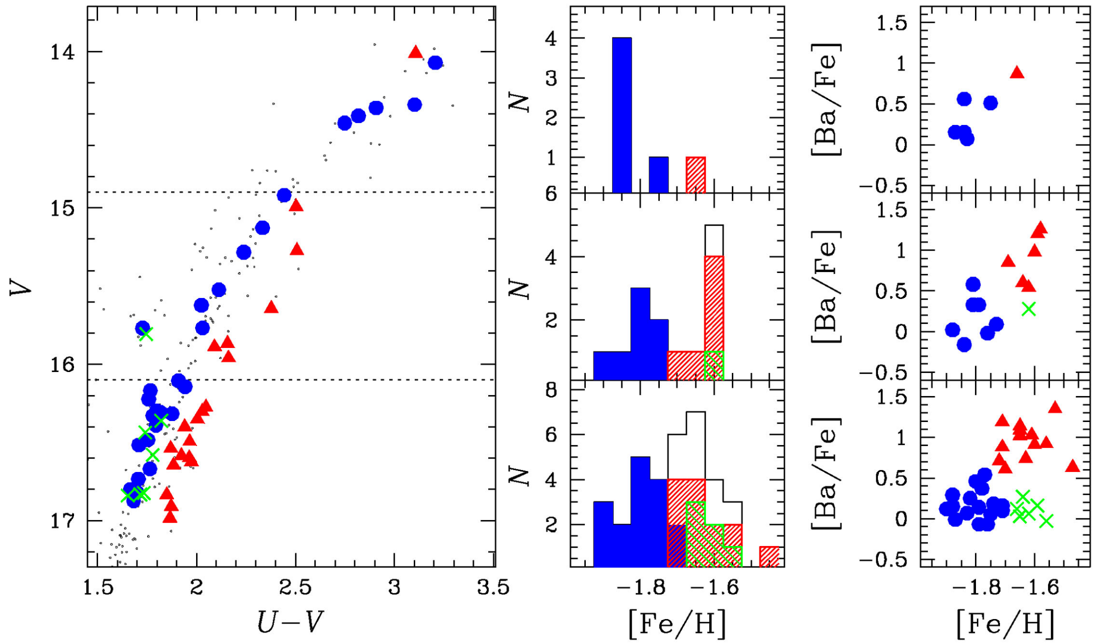

Figure 14. Left-hand panel: *V*–(*U* − *V*) CMD (left) of NGC 5286, corrected for differential reddening. Spectroscopic GIRAFFE targets are superimposed with *s*-rich/Fe-rich stars represented by red triangles, *s*-poor/Fe-poor stars by blue circles, and possible *s*-poor/Fe-rich stars by green crosses. Middle panels: histograms of [Fe/H] for GIRAFFE stars in the three different bins in *V*, represented on the *V*–(*U* − *V*) CMD. Right-hand panels: [Ba/Fe] versus [Fe/H] for stars in the three defined bins in *V* mag. Stars belonging to different Fe/*s*-groups have been represented with different colours. The sources for the photometric data are given in Section 2.1.

All seven GIRAFFE stars are at fainter magnitudes, and none of them is observed in the upper RGB, so it is tempting to state that the higher Fe abundances inferred for these fainter stars could be due to larger observational errors. On the middle and right-hand panels of Fig. 14, we note that in the lowest luminosity bin the dispersions in [Fe/H] are higher than those in the middle bin, both for the *s*-rich and the *s*-poor stars, suggesting that the internal errors are higher, as expected. However, although we expect a larger dispersion due to the lower S/N, it is difficult to explain with just errors the presence of these stars that reside preferentially on one side of the [Fe/H] distribution. On the other hand, as stars with different metallicity populate different RGB sequences, we cannot exclude selection effects in our sample that have selected preferentially stars belonging to the main *s*-rich and *s*-poor RGBs at brighter magnitudes where the separation among them is higher.

We recall that internal errors in atmospheric parameters are not able to produce the large variations we observe in *s*-elements, such as barium, but may be more important for [Fe/H] that shows much smaller variations. To check this possibility, we re-determined Fe and Ba for the entire GIRAFFE and UVES samples of stars by using a different set of atmospheric parameters. Specifically, we used effective temperatures from isochrone fitting, by projecting spectroscopic targets on the isochrone on the *V*–(*V* − *I*) CMD. Surface gravities and microturbulent velocities were determined as explained in Section 3. Results obtained by using parameters based on isochrones are shown in Fig. 15 for GIRAFFE (upper panels) and UVES (lower panels). Overall, for the GIRAFFE sample, we note that by using atmospheric parameters from isochrones we get higher precision. This is not surprising as the internal photometric errors cancel out by projecting on a fiducial or isochrone. On the other hand, in cases like NGC 5286 the use of one single isochrone is not appropriate: it can affect either, or both, of the two populations, e.g. introducing spurious abundance patterns and decreasing the

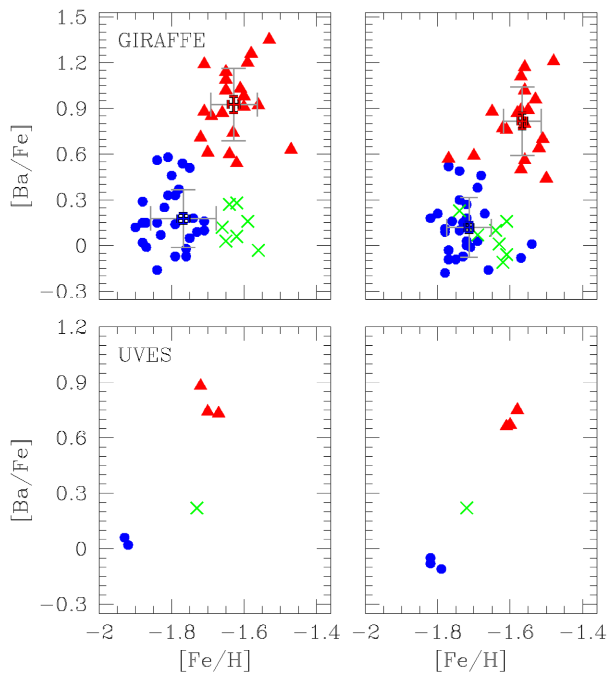

Figure 15. Abundance ratios [Ba/Fe] as functions of [Fe/H] for GIRAFFE (upper panels) and UVES data (lower panels). In each panel, blue circles represent *s*-poor/Fe-poor stars, red triangles represent probable *s*-rich/Fe-rich stars. The assumed abundances, from atmospheric parameters derived as explained in Section 3, are shown on the left-hand panels, while abundances derived by assuming parameters from isochrones are displayed on the right-hand panels. For GIRAFFE we show, for the *s*-poor (including the probable stars with higher Fe) and the *s*-rich groups, the average values, associated dispersions (grey bars) and errors (blue and red bars).

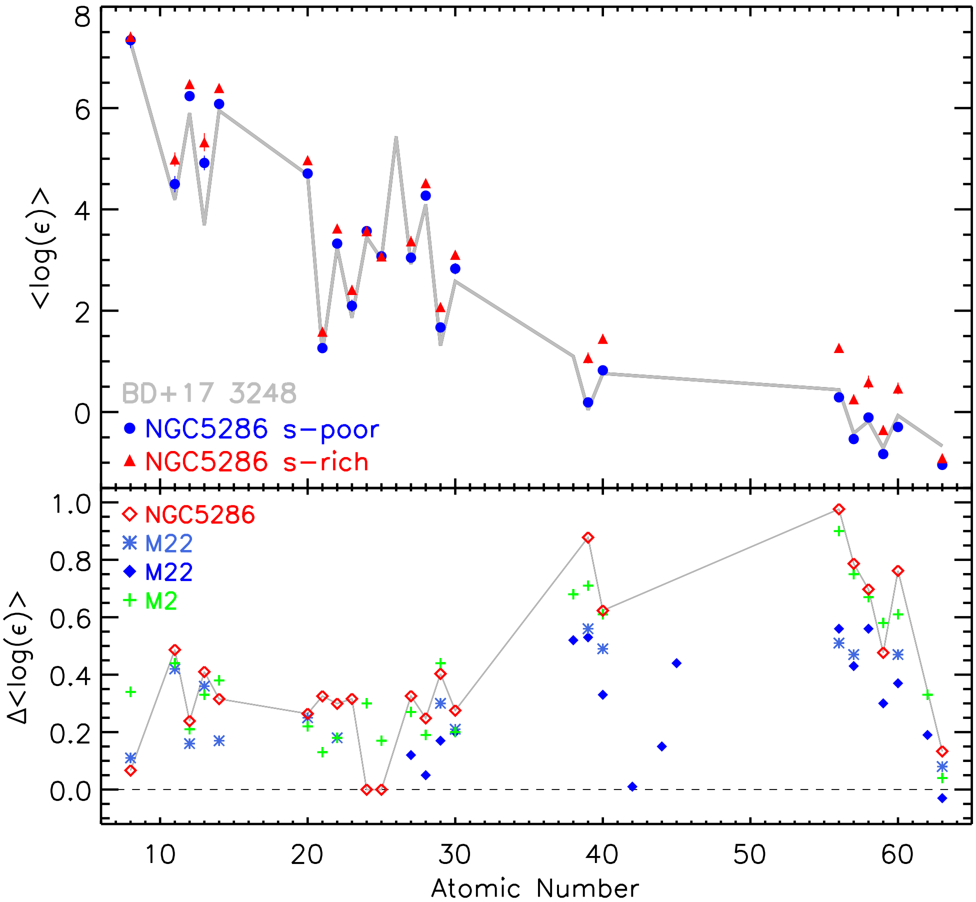

Figure 16. Top panel: mean logarithmic abundances for the three *s*-poor stars (blue circles) and the three *s*-rich stars in NGC 5286 (red triangles). The grey line illustrates the abundances in the *r*-process standard star BD+17° 3248 from Cowan et al. (2002). Bottom panel: differences in these mean abundances for the two *s*-groups (*s*-rich–*s*-poor) in NGC 5286 (red symbols), M 22 (blue stars from Marino et al. 2009, 2011b; filled blue symbols from Roederer et al. 2011), and M 2 (green crosses from Yong et al. 2014). The dashed line indicates zero difference.

accuracy. A few stars, due to observational errors, migrate from one group to the other, but apparently there is still a tail of *s*-poor stars with slightly higher metallicity.

Due to higher resolution and spectral coverage, UVES data provide more precise results. Adopting photometric stellar parameters based on isochrones, instead of purely spectroscopic parameters, we note that the star 1309U (green cross) approaches the metallicity of the *s*-poor stars, but still it is slightly metal rich. Our data set suggest that the *s*-poor group may be not homogenous in metallicity, but since the variation in metals is small, and not coupled with any large variation in other elements, such as the *s*-process elements, larger sample of these stars analysed with high-resolution/S/N data are required to definitively assess this issue.

6 THE CHEMICAL PATTERN OF NGC 5286 AND OTHER ANOMALOUS GCS COMPARED TO FIELD STARS

The dominant feature of the chemical pattern of NGC 5286 is the presence of two main stellar groups with different metallicities and the *n*-capture elements abundances. In Fig. 16, we show the mean logarithmic abundances for the three *s*-rich stars (red) and the three *s*-poor stars (blue) observed with UVES.

If we suppose that the abundances of the *s*-poor group are representative of 'primordial' NGC 5286 *n*-capture element material (that is, prior to any internal *n*-capture synthesis event), then we can compare the abundance patterns of this stellar group with those of BD+17° 3248, that is an *r*-process standard star whose metallicity is only a factor of ∼2 lower than stars in NGC 5286 (Cowan et al. 2002; Roederer, Marino & Sneden 2011). The *s*-poor stars of NGC 5286 (blue circles in Fig. 16) have element abundance patterns very similar to those in BD+17° 3248. The larger differences are in Mg and Al, that appear higher in NGC 5286, and in Eu which is lower.[6] Overall, the chemical pattern of the *s*-poor group in NGC 5286 is well approximated by the *r*-process standard BD+17° 3248.

Larger differences are observed between the abundance pattern of the *s*-rich group and BD+17° 3248. The mean chemical abundances for most of the analysed elements with $Z > 39$ are higher than in the *r*-process standard star, with the most significant differences in the first peak element Y, and the second peak elements Ba and La (see Section 5.1), while Pr shows more modest variations. The exception among these heavy elements is Eu, which does not show evidence for any enrichment in the *s*-rich stars.

The Solar system abundances of *n*-capture elements showing internal variations in NGC 5286 are largely produced by the *s*-process:

[6] Note that each *s*-group has its own internal variations in *p*-capture elements, so only on a first approximation is the *s*-poor composition representative of the primordial material.

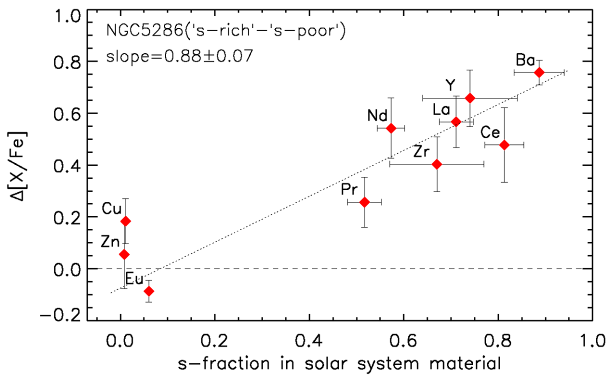

Figure 17. Differences in the mean abundances relative to Fe between the *s*-rich and the *s*-poor group of NGC 5286 as a function of the fraction of each element attributed to an *s*-process origin in solar material (Travaglio et al. 2004; Bisterzo et al. 2011). The dashed line indicates zero difference. We overplot the linear fit to the data and write the slope and associated error.

Y (72 per cent), Zr (81 per cent), La (75 per cent), Ce (81 per cent), and Ba (85 per cent) (e.g. Simmerer et al. 2004; Sneden et al. 2008). The origins of Pr and Nd in the Solar system are attributed to both the *r*- and *s*-processes in similar proportions: 51 per cent *r*-process, 49 per cent *s*-process for Pr, and 42 per cent *r*-process, 58 per cent *s*-process for Nd. We note however that at metallicities significantly lower than solar, as in this case, the relative production of *n*-capture elements by the *r*- or *s*-processes may be different. Among the inferred *n*-capture elements, Eu is the one with the most sharply contrasting Solar system *s*-process/*r*-process origins, as it is only 3 per cent *s*-process. The fact that Eu does not show any strong evidence of internal variation suggests that the chemical enrichment in NGC 5286 has been mostly due to the *s*-process, rather than the *r*-process. The excess of heavy elements found in the *s*-rich group relative to the *s*-poor group exhibits a correlation with the fraction of each element attributed to a *s*-process origin in Solar system material, as shown in Fig. 17. The element with the highest *s*-process fraction in the Solar system is Ba, which is also the most overabundant in the *s*-rich group. The more modest excess of Pr is in line with its smaller *s*-process fraction in the Solar system.

The enrichment in *s*-process elements in NGC 5286 has been accompanied by an enrichment in the overall metallicity. The hints of intrinsic internal dispersions in Fe among the *s*-poor stars, if confirmed by larger samples, would imply that stars with a moderate increase in overall metallicity form continuously, or in discrete bursts, prior to the enrichment in *s*-process elements. Additionally, the *s*-rich stars appear to have larger internal scatters in *s*-elements, favouring the idea of a more prolonged star formation for this stellar group.

The chemical enrichment history of NGC 5286 is made even more complex by the internal variations in *p*-capture elements, including evidence for O–Na anticorrelations and Na–Al correlations present in both groups with different *s*-elements. So, we have to assume either the pollution from high-mass AGB and/or fast-rotating massive stars has occurred before the enrichment in *s*-elements. Alternatively, the variations in light elements are not due to different stellar generations, but to other mechanisms, such as early accretion discs in pre-MS binary systems (Bastian et al. 2013).

NGC 5286 shares many similarities with some of the other *anomalous* GCs, e.g. those with metallicity variations (see Section 1), studied so far. First, it shows a genuine internal variation in the overall metallicity and, for this reason, it can be included among the class of *anomalous* GCs. Secondly, it exhibits large internal variations in *s*-process elements, that have been also detected in other *anomalous* GCs, e.g. ω Centauri, NGC 1851, M 22, and M 2. In these clusters, the *s*-rich population(s) exhibit higher metallicity with respect to the *s*-poor/metal-poor population(s). In the other considered *anomalous* GCs, specifically M 54, Terzan 5, NGC 5824, there is no information on the *s*-process element abundances in populations with different Fe, and we cannot prove or disprove, at the moment, *s*-process enrichment in these objects.

A list of the known *anomalous* GCs, and their chemical properties, is provided in Table 10. The objects exhibiting also *s*-process variations have been classified as *s*-Fe *anomalous*. The class of *s*-Fe *anomalous* has to be intended as a sub-class of the *anomalous* GCs. Of the eight *anomalous* GCs, five are *s*-Fe *anomalous*. The *s*-process enrichment is observed in a significant fraction of *anomalous* GCs, suggesting that, even if the range in metallicity variations is different in these objects, they have experienced some contribution from low-mass AGBs. We emphasize that the Fe and the *s* enrichments are very likely due to different mass ranges and polluters, e.g. to high-mass and low-mass first-generation stars, respectively. A possibility is that in these more massive proto-clusters, the star formation proceeded for longer times than in *normal* clusters, giving the possibility to low-mass AGBs to contribute to the enrichment of the proto-cluster. At the time these low-mass stars start to pollute the intracluster medium, material enriched from fast SNe, and previously expelled, may have had the time to be *fall-back* into the cluster. A similar scenario has been proposed by D'Antona et al. (2011) for ω Centauri.

All the known *s*-Fe *anomalous* GCs also have internal variations in light elements (such as a Na–O anticorrelation) within stars with different metallicity and *s*-content (see Table 10). For the objects in which a mono-metallic group can be defined (e.g. M 22 *s*-Fe-poor, M 22 *s*-Fe-rich), they resemble a *normal* GC.

The comparison of the chemical properties of NGC 5286 with other *anomalous* GCs may shed some light on the origin of these objects. Specifically, M 22 and M 2 are more suitable for comparison with NGC 5286 because they have a similar metallicity, and comparable variations in the [Fe/H] between the *s*-poor and *s*-rich stars. Note that M 2 also shows a third group with much higher metallicity and no *s*-element enrichment. It is tempting to speculate that this third group in M 2 is the counterpart of the few stars with low *s*-elements and relatively high Fe possibly present in NGC 5286. However, for simplicity, we consider just the *s*-poor and the *s*-rich stars of M 2 to be compared with the stellar groups of NGC 5286

In Fig. 16, we compare the abundance pattern inferred here for NGC 5286 with those of M 22 and M 2, considering the mean abundance differences between the *s*-rich and *s*-poor (*s*-rich−*s*-poor) stars observed in each of these clusters. We note that for elements with $Z > 27$ the chemical variations observed in the two stellar groups of NGC 5286 are very similar to those observed in M 2. Yttrium ($Z = 39$) variations appear to be larger in NGC 5286. Among the *p*-capture elements the most notable difference is in O, which varies more between the *s*-poor and the *s*-rich groups of M 2 than in those of NGC 5286. Note however that since light elements vary in each single *s*-group, the total observed variation in these elements may not be representative of the entire variations in these elements due to small-number statistics.

More distinctive differences are seen with respect to M 22. For this cluster, we plotted both abundances from Marino et al. (2009, 2011b, blue stars) and from Roederer et al. (2011, blue diamonds). Both data sets for M 22 suggest that it has more moderate variations

Table 10. List of confirmed *anomalous* GCs, e.g. those with known metallicity variations, and their chemical properties. A subsample of these GCs have been classified as *s*-Fe *anomalous*, as they show also variations in *s*-process elements. For each object, and chemical property, we list the literature source.

GC	Metallicity	Literature source	Chemical abundance variations						Proposed class
			s-elements	Literature source	*p*-capture elements in each Fe group	Literature source	C+N+O	Literature source	
ω Centauri	Yes	Norris et al. (1996); Suntzeff & Kraft (1996)	Yes	Norris & Da Costa (1995); Smith et al. (2000); Johnson & Pilachowski (2010); Marino et al. (2011b); D'Orazi et al. (2011)	Yes	Johnson & Pilachowski (2010); Marino et al. (2011b)	Yes	Marino et al. (2012)	*s*-Fe anomalous
M 22	Yes	Marino et al. (2009); Da Costa et al. (2009)	Yes	Marino et al. (2009, 2011a, 2012)	Yes	Marino et al. (2009, 2011a)	Yes	Marino et al. (2011a); Alves-Brito et al. (2012)	*s*-Fe anomalous
NGC 1851	Possible small	Carretta et al. (2010a); Gratton et al. (2013); Marino et al. (2014)	Yes	Yong & Grundahl (2008); Villanova et al. (2010)	Yes	Carretta et al. (2010a); Villanova et al. (2010)	Yes	Yong et al. (2014)	*s*-Fe anomalous
Terzan 5	Yes	Ferraro et al. (2009); Origlia et al. (2011); Massari et al. (2014)	Not studied		Not studied		Not studied		Anomalous
M 54	Yes	Carretta et al. (2010b)	Not studied		Yes	Carretta et al. (2010b)	Not studied		Anomalous
M 2	Yes	Yong et al. (2014)	Yes	Lardo et al. (2013); Yong et al. (2014)	Yes	Yong et al. (2014)	Not studied		*s*-Fe anomalous
NGC 5824	Yes	Da Costa et al. (2014)	Not studied		Not studied		Not studied		Anomalous
NGC 5286	Yes	This work	Yes	This work	Yes	This work	Not studied		*s*-Fe anomalous

in all the *s*-elements than in M 2 and NGC 5286. A common feature displayed by NGC 5286, M 22, and M 2 is the apparent constancy of [Eu/Fe] suggesting that in all of these GCs the chemical enrichment was due to pollution of material that has undergone *s*-processing, rather than *r*-processing.

As already discussed, the most commonly discussed stellar site where *s*-neutron capture occurs is AGB stars. Recently, Shingles et al. (2014) and Straniero, Cristallo & Piersanti (2014), suggested that both AGB stars with a ^{22}Ne source and lower-mass AGB stars with ^{13}C pockets are required to account for the *s*-elements enrichment in M 22 and to explain the large *s*-process elements abundances in M 4 (relative to clusters with same metallicity like M 5). The contribution from stars with masses as low as 2.75–4.5 $M_{\odot}$ may be required to explain the enrichment, with the precise lower limit depending on which assumptions are made about ^{13}C-pocket formation in AGB models (Shingles et al. 2014; Straniero et al. 2014). We may think that similar mechanisms have worked also in NGC 5286, but future proper analysis for this specific case would be enlightening to understand the higher *s*-enrichment.

Fig. 18 reproduces fig. 3 from Roederer et al. (2010). It shows the logarithmic abundance ratios of La/Eu as a function of the metallicity for metal-poor stars, including C-enriched metal-poor stars with overabundances of *s*-process material (CEMP/*s*). Many CEMP/*s* stars are known binary systems, indeed all of them may be in binaries (e.g. McClure, Fletcher & Nemec 1980; McClure 1983; Lucatello et al. 2005). The approximate minimum La/Eu ratio expected from AGB pollution is shown in Fig. 18 as a dashed cyan line. Superimposed on to the field stars are the average abundances for the *s*-poor and *s*-rich stars in NGC 5286 together with those for M 2 (Yong et al. 2014), and M 22 (Marino et al. 2009, 2011b). We note that the two groups of M 22, besides showing the smaller difference, also lie below the expected minimum *s*-process enrichment. On the other hand, *s*-rich stars in NGC 5286 and M 2 are well above this minimum, with La/Eu ratios being higher by ∼0.2 dex in both the *s*-groups of NGC 5286. The differences on the La/Eu variations present in these clusters may indicate different degrees of intracluster pollution. While starting abundance levels may be affected by systematics between different studies, it is clear that *s*-rich stars of NGC 5286 and M 2 lie in a region very close to that occupied by CEMP/*s* field stars. CEMP/*s* stars are well fitted by AGB models of low-mass indicating that ^{13}C neutron source is dominant (Bisterzo et al. 2012; Lugaro et al. 2012). The fact that NGC 5286 and M 2 stars are closer to the CEMP/*s* stars in the La/Eu-Fe diagram hints to a similar pollution source.

Assuming that in all these GCs low-mass AGB stars have contributed, possibly at different degrees, to the chemical self-enrichment, we emphasize that the real situation is more complex. Two observables make the situation much more difficult to understand: (i) the light-element variations within each *s*-group; and (ii) the increase in the overall metallicity in the *s*-rich stars. We thus require the operation of at least two different nucleosynthetic processes during the formation and evolution of these GCs, e.g. higher mass AGB/fast-rotating massive stars for the light-element variations and supernovae for the metallicity increase.

The higher relative variations in the *s*-process elements in NGC 5286 and M 2, relative to M 22, occur despite the very similar variation in metallicity between the *s*-poor and the *s*-rich stars. Quantitatively, the variations (*s*-rich−*s*-poor) in [Fe/H] and [Ba/Fe] in the three GCs are listed in Table 11. From these values, we see that the total range in *s*-process elements in NGC 5286 is about twice as large as it is in M 22, and it is similar to M 2. This may suggest that there may be some differences in the polluters that

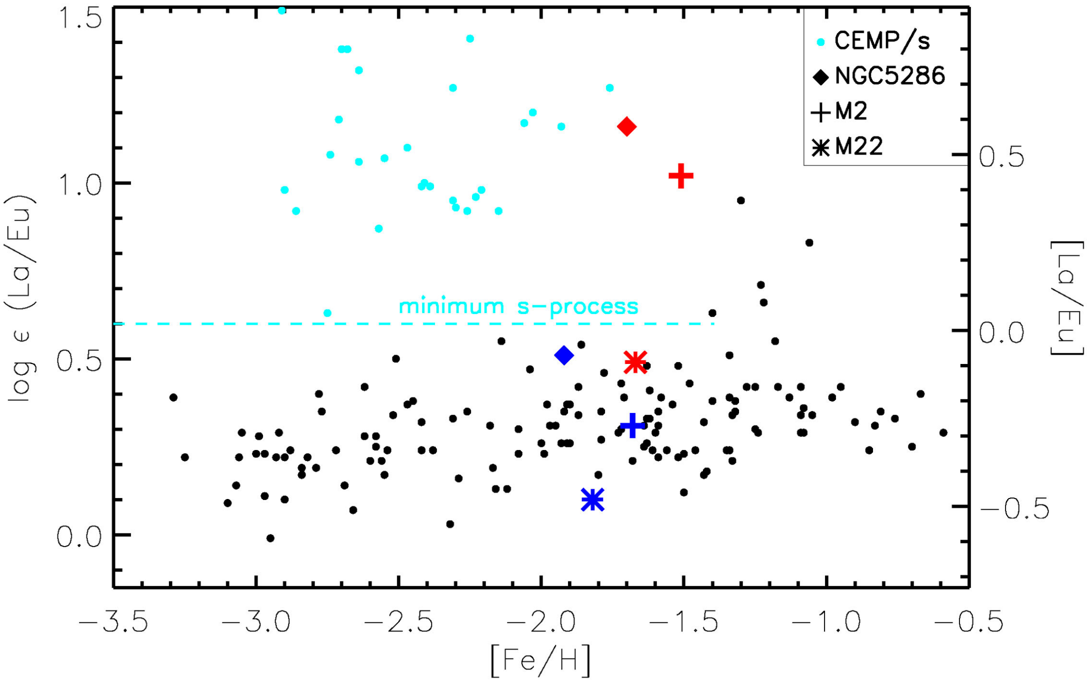

Figure 18. Logarithmic abundance ratios of La/Eu as a function of [Fe/H] for metal-poor halo stars. All measurements for field stars are indicated by small black and cyan circles, with cyan circles denoting stars enriched in *s*-process material. The literature sources of these data are Roederer et al. (2010a), Aoki et al. (2001, 2002), Barbuy et al. (2005), Cohen et al. (2003, 2006), Goswami et al. (2006), Ivans et al. (2005), Johnson & Bolte (2004), Jonsell et al. (2006), Preston & Sneden (2001), Roederer et al. (2010b), Simmerer et al. (2004), and Thompson et al. (2008). The dashed line indicates log (La/Eu)≤+0.6, the approximate minimum ratios expected from AGB pollution (appropriate for [Fe/H]<−1.4 dex). Superimposed on to the field stars are the average abundances for the *s*-poor (blue) and *s*-rich stars (red) in NGC 5286 (diamonds), M 2 (plus; Yong et al. 2014), and M 22 (stars; Marino et al 2009, 2011b).

Table 11. Mean Fe and Ba abundance differences for the *anomalous* GCs M 22, M 2, and NGC 5286. We list the differences among the *s*-poor and *s*-rich stars in M 22 from Marino et al. 2009, 2011b, M 2 from Yong et al. (2014).

Abundance difference (*s*-rich−*s*-poor)	M 22	M 2	NGC 5286
Δ[Fe/H]	+0.15 ± 0.02	+0.17 ± 0.04	+0.17 ± 0.01
Δ[Ba/Fe]	+0.36 ± 0.05	+0.73 ± 0.14	+0.74 ± 0.06
Δ[Ba/Fe]/Δ[Fe/H]	+2.4 ± 0.5	+4.3 ± 1.3	+4.4 ± 0.5

enriched the intracluster medium in NGC 5286 and M 2 relatively to M 22. The *s*-process nucleosynthesis per increase in Fe varies between the clusters, and this must eventually tell us something useful about time-scales, mass functions, or maybe dilution with pristine gas.

7 ANOMALOUS GCs AND MILKY WAY SATELLITES

Apart from the chemical/photometric features discussed above, comparing *s*-Fe-*anomalous* GCs with *anomalous* (non-*s*) GCs or with those clusters not identified as *anomalous* there is no evidence (to date) for different global/non-global parameters, except that *anomalous* and *s*-Fe *anomalous* GCs are among the most massive in the Milky Way. In Fig. 19, we show the Ba and La abundances relative to Fe as a function of [Fe/H] for *s*-Fe-*anomalous* GCs and field stars taken from this study and the literature. For NGC 5286, we used the larger sample observed with GIRAFFE. In these plots, it is clear that there is a common rise of *s*-elements with metallicity in the common metallicity regime. The data for *ω* Centauri suggest that in this case there is a significant extension towards higher [Fe/H], but above [Fe/H] ∼− 1.5 there is a plateau in *s*-elements. In the common metallicity regime there is a similar rise in *s* in NGC 5286 and M 2.

Internal variations in metallicity are intriguing because, assumed that they arise from internal chemical evolution, they suggest that material ejected at fast velocities from supernovae (SNII) could has been retained by these GCs at their early stages of evolution. This would imply that their initial masses were much higher. The idea that the very extreme GC *ω* Centauri is the nucleus of a dwarf galaxy was first suggested by Bekki & Freeman (2003). The discovery of more objects with similar properties, although less extreme, may suggest that these objects may also be surviving nuclei of dwarf galaxies. This scenario would provide eight more candidates to alleviate the missing satellites problem, i.e. the lack of observed MW satellites compared to the numbers expected from theoretical simulations (e.g. Kauffmann, White & Guiderdoni 1993; Klypin et al. 1999; Moore et al. 1999).

Additional support for the idea that the *anomalous* GCs may constitute the central remnants of dwarf galaxies after the outer layers have been stripped away come from other observations. The position of the GC M 54 coincides with the nucleus of the

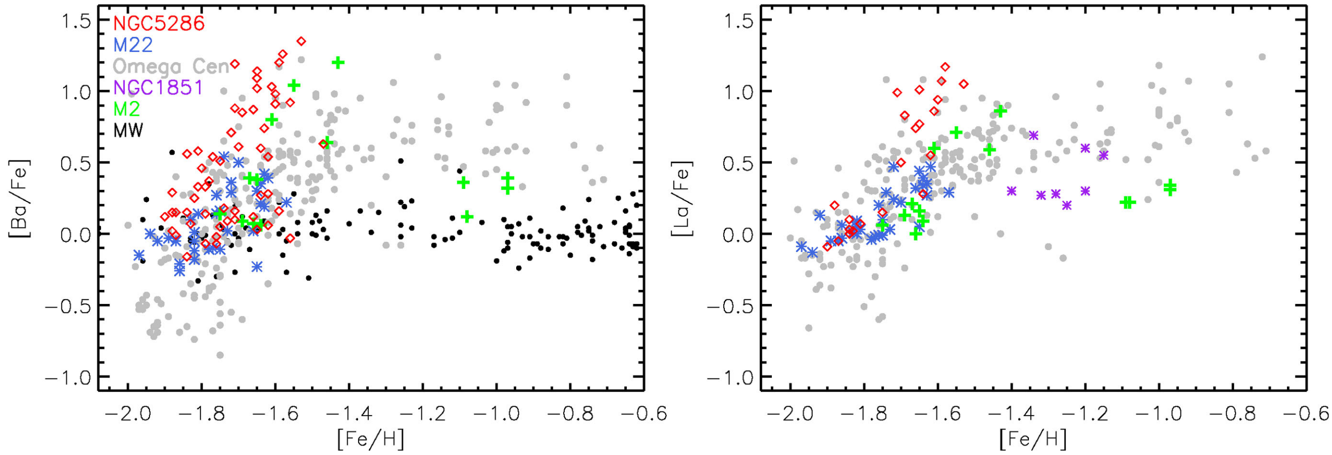

Figure 19. [Ba/Fe] and [La/Fe] as a function of [Fe/H] for anomalous GCs and field stars. Different symbols and colours are used for different GCs, as shown in the legend. The literature sources of the plotted abundances are: this paper for NGC 5286; Marino et al. (2009; 2011b) for M 22; Marino et al. (2011a) for ω Centauri; Yong et al. (2008) for NGC 1851; Yong et al. (2014) for M 2; and Fulbright (2000) for the Milky Way field stars.

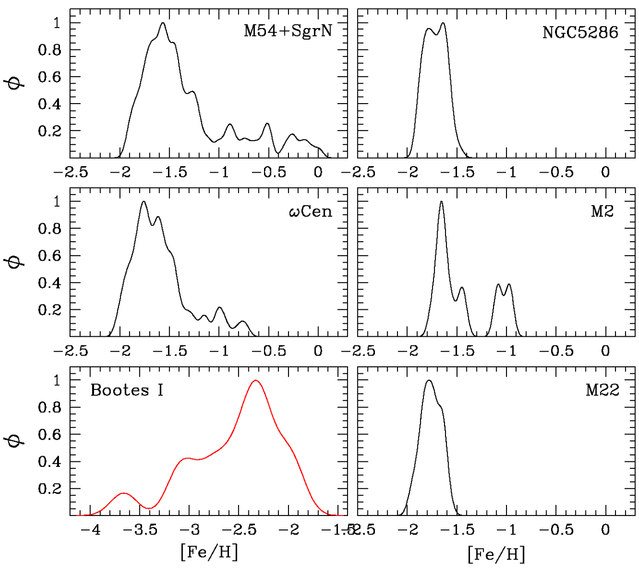

Figure 20. Metallicity histograms for the GCs with detected internal variations in metallicity plus *s*-process elements. The literature sources of these data are: Marino et al (2009, 2011b) for M 22, Marino et al. (2011a) for ω Centauri and Yong et al. (2014) for M 2. As a comparison, we also show the metallicity distribution for the UFD galaxy Bootes I (data from Norris et al. 2010) and the GC M 54+SgrN (data from Carretta et al. 2010b).

Sagittarius dwarf galaxy (Layden & Sarajedini 2000) and has metallicity variations (Carretta et al. 2010a). Also, a low-density halo of stars surrounding NGC 1851 has been discovered by Olszewski et al. (2009), whose chemistry is compatible with the *s*-poor group observed in this cluster (Marino et al. 2014). The absence of *s*-rich stars in this halo may suggest either that this GC is preferentially losing *s*-poor stars into the field, or that this sparse structure is the remnant of a dwarf galaxy, as its composition is compatible with field stars at similar metallicity (Marino et al. 2014).

The lower-left panel of Fig. 20 shows the metallicity distribution function (MDF) for 16 stars in the ultrafaint dwarf galaxy (UFD) Bootes I (from Norris et al. 2010). Norris and collaborators noted that Bootes I, similarly to that observed in dwarf spheroidals, exhibits a slow increase from lowest abundance to the MDF peak, while, by contrast, ω Centauri shows a steep rise. In the other panels of Fig. 20, we compare the [Fe/H] kernel-density distributions for the *anomalous* GCs studied through high-resolution spectroscopy, including ω Centauri and the M 54 plus the Sagittarius nucleus (SgrN) system. An inspection of these distributions reveals that a sharp rise in metallicity to the metal-poorer peak[7] is a common feature among *anomalous* GCs.

Another difference among *anomalous* GCs and dwarf galaxies is the lack, in the latter, of typical (anti)correlation patterns among light elements (e.g. Norris et al. in preparation for Carina). We note however that, if the hypothesis of the origin of *anomalous* GCs as nuclei of disrupted dwarf galaxies will be confirmed, the chemistry of the dwarfs does not have to necessarily resemble the GCs' one, as the latter would constitute just their nuclear regions. In *anomalous* GCs, the variations in light elements within each *s*/Fe-group (such as the individual Na–O anticorrelation) is difficult to understand within a self-pollution scenario, even in the hypothesis that the *anomalous* GCs are the nuclear remnants of more massive systems. As individual *s*-groups appear similar to mono-metallic GCs, with their own Fe content and their own Na–O anticorrelation, it has been proposed that they can result from mergers between different clusters (e.g. Bekki & Yong 2012). If this scenario will apply to every anomalous GC, we will need to understand why in almost all the GCs with internal metallicity variations found so far the increase in metals is coupled with a *s*-enrichment. In other words, we should find an explanation for the very similar properties of these objects, while in the hypothesis of a merger of two (or more) GCs one would expect a much more heterogenous observational scenario.

It is worth noticing that nearby dwarf and irregular galaxies host their more massive GCs in their central regions, these GCs being *nuclear* star clusters (e.g. Georgiev et al. 2009). We do not have, at the moment, any evidence for these nuclear GCs to share the same Fe distribution of the parent galaxies, or they show instead Fe distributions and chemical patterns more similar to the Galactic *anomalous* GCs.

To explore further a possible galaxies-*anomalous* GCs connection, we plotted the position of various stellar systems in the half-light radius (log (r_h/pc)) versus absolute-mag (M_V) plane (Fig. 21).

[7] We note that the distributions shown in Fig. 20 for the *anomalous* GCs are biased in the number of metal-richer stars for NGC 5286, M 2, and M 54+SgrN because metal-richer stars have been preferentially selected.

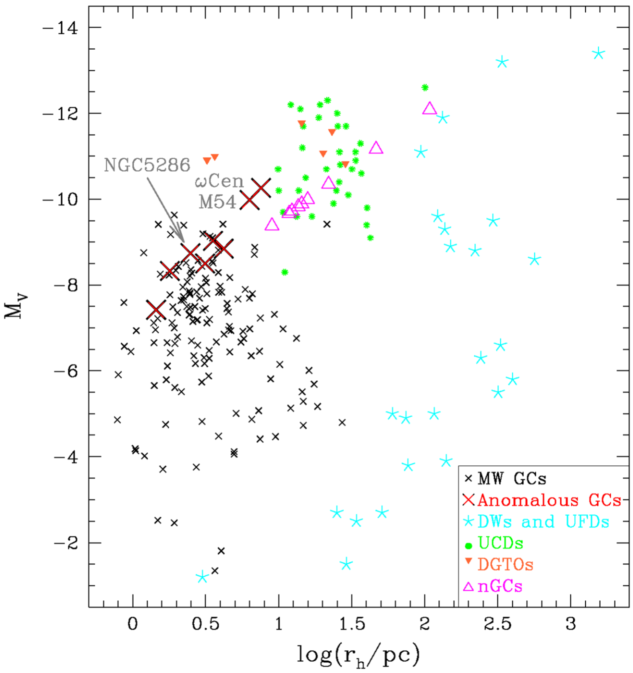

Figure 21. Absolute magnitude as a function of the half-light radius (r_h). Different colours and symbols represent different class of objects: Milky Way GCs (black crosses; Harris 2010), Milky Way satellites including dwarf (DW; Irwin & Hatzidimitriou 1995; Mateo 1998), ultrafaint dwarf galaxies (UFDs) and all the objects discovered by the SDSS (Willman et al. 2005, 2006; Belokurov et al. 2006, 2007; Zucker et al. 2006; Jerjen 2010), ultra-compact dwarf galaxies (UCDs; Brodie et al. 2011), nucleated GCs (nGCs; Georgiev et al. 2009), dwarf-globular transition objects (DGTOs; Haşegan et al. 2005). Anomalous GCs, here considered as all the objects with internal metallicity and/or heavy-elements variations, have been marked with red crosses.

We include the position of Milky Way GCs, classical dwarfs and UFDs, ultracompact dwarfs (UCDs), dwarf-globular transition objects (DGTOs), nucleated GCs (nGCs). The position of GCs with internal variations in the overall metallicity (including those with not-investigated *s*-element abundances) shows that they are in general among the most massive GCs. Furthermore, various stellar systems appear to clump in different regions of the M_V–log (r_h/pc) plane, with GCs with metallicity variations interestingly falling in regions abutting (or *evolving*) UCDs, DGTOs, nGCs.

It is worth noticing that the mean [Fe/H] is very similar between NGC 5286, M 22, and M 2. Is this due to some selection effects or could this similarity in metallicity coincide with a particular phase in the MW or galaxies' evolution? For example, if these objects formed as dwarf galaxies' nuclei, we may suppose that the accreted dwarfs had nuclei with similar metallicities. This would imply that these nuclei formed out chemically similar clouds, probably at similar evolutionary phases of their host galaxies. On the other hand, if we suppose that these objects are the result of mergers, their similar metallicities may indicate a phase of abundant mergers in early galaxies.

8 CONCLUSION

We have found genuine metallicity and *s*-process abundance variations in the Galactic GC NGC 5286. To date large Fe variations have been confirmed to be present in eight GCs, including M 22 and M 2, which have a similar mean metallicity as NGC 5286. As the mono-metallicity is a typical feature of Galactic GCs, we classify all the GCs with internal variations in metals as *anomalous* GCs. A sub-class of *anomalous* GCs, 5/8, that we define *s*-Fe *anomalous* have confirmed variations in *s*-elements. The class of *s*-Fe *anomalous* GCs show common observational features:

(i) Photometrically:

(a) On the CMD, the most striking feature of all these GCs is a split in the SGB in visual bands. This split can be considered as an indication of *s*-elements+(C+N+O)+Fe variations, and can guide future spectroscopic observations aimed at the identification of other 'anomalous' GCs;

(b) large separations in the different *s*-populations along the RGBs, evolving from multiple SGBs, in the U–(U − V) CMDs, and a maximum separation obtained using our new defined photometric index c_{BVI};

(ii) Spectroscopically:

(a) by definition, internal variations and/or multimodalities in the *s*-process elements;

(b) by definition, different degrees of variations in the main metallicity, but in all cases the Fe content is higher in the *s*-richer stars.

(c) no variations in the *r*-process elements detectable within observational errors. More specifically, for a given element, the degree of the abundance difference between the two stellar groups is strongly correlated with the fraction attributed to the *s*-process in Solar system material;

(d) variations in light elements (e.g. Na, O) often present in each main stellar group with different *s*-elements abundance;

NGC 5286 shows internal variations in metals similar to those present between the two groups of *s*-rich and *s*-poor stars of M 22 and M 2, and *s*-abundance variations much higher than in M 22, but similar to M 2. Among field stars, the stars that show largest similarities with the *s*-rich stars of NGC 5286 and M 2 are the CEMP/*s* stars (while M 22 appears to have undergone lower levels of *s*-enrichments).

We conclude that the observational scenario for the *anomalous* GCs is not compatible with an origin of these objects as *normal* GCs, with typical initial masses in the range observed today. It is intriguing to think, that these objects, much more massive at their birth, may be nuclei of dwarfs tidally disrupted through interactions with the Milky Way, just as the *anomalous* GC M 54 lies at the central region of Sagittarius. If this hypothesis will be confirmed, the eight *anomalous* GCs should count as Milky Way satellites, with the number of those being substantially enhanced with respect to the number of the 27 confirmed known satellites (McConnachie 2012).

ACKNOWLEDGEMENTS

This research has been supported in part by the Australian Research Council through grants FL110100012, DP120100991, and DP120101237. APM acknowledges support by the Australian Research Council through Discovery Early Career Researcher Award DE150101816.

REFERENCES

Alonso A., Arribas S., Martínez-Roger C., 1999, A&AS, 140, 261
Alves-Brito A., Yong D., Meléndez J., Vásquez S., Karakas A. I., 2012, A&A, 540, A3

Anderson J., King I. R., 2003, AJ, 126, 772
Anderson J., van der Marel R. P., 2010, ApJ, 710, 1032
Anderson J., Bedin L. R., Piotto G., Yadav R. S., Bellini A., 2006, A&A, 454, 1029
Aoki W. et al., 2001, ApJ, 561, 346
Aoki W., Ryan S. G., Norris J. E., Beers T. C., Ando H., Tsangarides S., 2002, ApJ, 580, 1149
Asplund M., Grevesse N., Sauval A. J., Scott P., 2009, ARA&A, 47, 481
Barbuy B., Spite M., Spite F., Hill V., Cayrel R., Plez B., Petitjean P., 2005, A&A, 429, 1031
Bastian N., Lamers H. J. G. L. M., de Mink S. E., Longmore S. N., Goodwin S. P., Gieles M., 2013, MNRAS, 436, 2398
Bedin L. R., Piotto G., Carraro G., King I. R., Anderson J., 2006, A&A, 460, L27
Bekki K., Freeman K. C., 2003, MNRAS, 346, L11
Bekki K., Norris J. E., 2006, ApJ, 637, L109
Bekki K., Yong D., 2012, MNRAS, 419, 2063
Bellini A., Bedin L. R., Piotto G., Milone A. P., Marino A. F., Villanova S., 2010, AJ, 140, 631
Belokurov V. et al., 2006, ApJ, 647, L111
Belokurov V. et al., 2007, ApJ, 654, 897
Bergemann M., Lind K., Collet R., Magic Z., Asplund M., 2012, MNRAS, 427, 27
Bielski A., 1975, J. Quant. Spectrosc. Radiat. Transfer, 15, 463
Biemont E., Grevesse N., Hannaford P., Lowe R. M., 1981, ApJ, 248, 867
Bisterzo S., Gallino R., Straniero O., Cristallo S., Käppeler F., 2011, MNRAS, 418, 284
Bisterzo S., Gallino R., Straniero O., Cristallo S., Käppeler F., 2012, MNRAS, 422, 849
Brodie J. P., Romanowsky A. J., Strader J., Forbes D. A., 2011, AJ, 142, 199
Burris D. L., Pilachowski C. A., Armandroff T. E., Sneden C., Cowan J. J., Roe H., 2000, ApJ, 544, 302
Cannon R. D., Croke B. F. W., Bell R. A., Hesser J. E., Stathakis R. A., 1998, MNRAS, 298, 601
Carretta E., Bragaglia A., Gratton R., Lucatello S., 2009, A&A, 505, 139
Carretta E. et al., 2010a, A&A, 520, A95
Carretta E. et al., 2010b, ApJ, 722, L1
Casagrande L., Ramírez I., Meléndez J., Bessell M., Asplund M., 2010, A&A, 512, A54
Casagrande L. et al., 2014, MNRAS, 439, 2060
Cassisi S., Salaris M., Pietrinferni A., Piotto G., Milone A. P., Bedin L. R., Anderson J., 2008, ApJ, 672, L115
Castelli F., Kurucz R. L., 2004, preprint (astro-ph/0405087)
Clement C. M. et al., 2001, AJ, 122, 2587
Cohen J. G., Christlieb N., Qian Y.-Z., Wasserburg G. J., 2003, ApJ, 588, 1082
Cohen J. G. et al., 2006, AJ, 132, 137
Cowan J. J. et al., 2002, ApJ, 572, 861
D'Antona F., D'Ercole A., Marino A. F., Milone A. P., Ventura P., Vesperini E., 2011, ApJ, 736, 5
D'Orazi V., Gratton R. G., Pancino E., Bragaglia A., Carretta E., Lucatello S., Sneden C., 2011, A&A, 534, AA29
Da Costa G. S., Held E. V., Saviane I., Gullieuszik M., 2009, ApJ, 705, 1481
Da Costa G. S., Held E. V., Saviane I., 2014, MNRAS, 438, 3507
Dotter A., Chaboyer B., Jevremović D., Kostov V., Baron E., Ferguson J. W., 2008, ApJS, 178, 89
Ferraro F. R. et al., 2009, Nature, 462, 483
Fuhr J. R., Wiese W. L., 2009, in Lide D. R., ed., CRC Handbook of Chemistry and Physics, 90th edn.CRC Press, Boca Raton, FL, p. 10
Fulbright J. P., 2000, AJ, 120, 1841
Gallagher A., 1967, Phys. Rev., 157, 24
Georgiev I. Y., Hilker M., Puzia T. H., Goudfrooij P., Baumgardt H., 2009, MNRAS, 396, 1075
Gilmore G. et al., 2012, The Messenger, 147, 25
Goswami A., Aoki W., Beers T. C., Christlieb N., Norris J. E., Ryan S. G., Tsangarides S., 2006, MNRAS, 372, 343
Gratton R. G. et al., 2001, A&A, 369, 87
Gratton R., Sneden C., Carretta E., 2004, ARA&A, 42, 385
Gratton R. G. et al., 2013, A&A, 549, AA41
Grundahl F., 1999, Spectrophotometric Dating of Stars and Galaxies, 192, 223
Hannaford P., Lowe R. M., Grevesse N., Biemont E., Whaling W., 1982, ApJ, 261, 736
Harris W. E., 1996, AJ, 112, 1487
Harris W. E., 2010, preprint (arXiv:1012.3224)
Haşegan M. et al., 2005, ApJ, 627, 203
Irwin M., Hatzidimitriou D., 1995, MNRAS, 277, 1354
Ivans I. I., Sneden C., Gallino R., Cowan J. J., Preston G. W., 2005, ApJ, 627, L145
Ivarsson S., Litzen U., Wahlgren G. M., 2001, Phys. Scr., 64, 455
Jerjen H., 2010, in Moitinho A., Amores E., Arsenijevic V., Ascenso J., Azevedo R., eds, Joint European and National Astronomy Meeting, the European week of astronomy and space science, Lisbon, Portugal, p.. 170
Johnson J. A., 2002, ApJS, 139, 219
Johnson J. A., Bolte M., 2004, ApJ, 605, 462
Johnson C. I., Pilachowski C. A., 2010, ApJ, 722, 1373
Jonsell K., Barklem P. S., Gustafsson B., Christlieb N., Hill V., Beers T. C., Holmberg J., 2006, A&A, 451, 651
Kauffmann G., White S. D. M., Guiderdoni B., 1993, MNRAS, 264, 201
Kausch W. et al., 2014, in Manset N., Forshay P., eds, ASP Conf. Ser. Vol. 485, Astronomical Data Analysis Software and Systems XXIII. Astron. Soc. Pac., San Francisco, p. 403
Klypin A., Kravtsov A. V., Valenzuela O., Prada F., 1999, ApJ, 522, 82
Kraft R. P., 1994, PASP, 106, 553
Kurucz R. L., 2009, in Hubeny I., Stone J. M., MacGregor K., Werner K., eds, AIP Conf. Proc. Vol. 1171, Recent Directions in Astrophysical Quantitative Spectroscopy and Radiation Hydrodynamics. Am. Inst. Phys., New York, p. 43
Kurucz R. L., Bell B., 1995, Kurucz CD-ROM. Smithsonian Astrophysical Observatory, Cambridge, MA
Lardo C. et al., 2013, MNRAS, 433, 1941
Lawler J. E., Bonvallet G., Sneden C., 2001a, ApJ, 556, 452
Lawler J. E., Wickliffe M. E., den Hartog E. A., Sneden C., 2001b, ApJ, 563, 1075
Layden A. C., Sarajedini A., 2000, AJ, 119, 1760
Lee J.-W., Kang Y.-W., Lee J., Lee Y.-W., 2009, Nature, 462, 480
Li R., Chatelain R., Holt R. A., Rehse S. J., Rosner S. D., Scholl T. J., 2007, Phys. Scr., 76, 577
Lind K., Asplund M., Barklem P. S., Belyaev A. K., 2011, A&A, 528, AA103
Lind K., Bergemann M., Asplund M., 2012, MNRAS, 427, 50
Lucatello S., Tsangarides S., Beers T. C., Carretta E., Gratton R. G., Ryan S. G., 2005, ApJ, 625, 825
Lugaro M., Karakas A. I., Stancliffe R. J., Rijs C., 2012, ApJ, 747, 2
McClure R. D., 1983, ApJ, 268, 264
McClure R. D., Fletcher J. M., Nemec J. M., 1980, ApJ, 238, L35
McConnachie A. W., 2012, AJ, 144, 4
McLaughlin D. E., van der Marel R. P., 2005, ApJS, 161, 304
Marino A. F., Villanova S., Piotto G., Milone A. P., Momany Y., Bedin L. R., Medling A. M., 2008, A&A, 490, 625
Marino A. F., Milone A. P., Piotto G., Villanova S., Bedin L. R., Bellini A., Renzini A., 2009, A&A, 505, 1099
Marino A. F. et al., 2011a, A&A, 532, A8
Marino A. F. et al., 2011b, ApJ, 731, 64
Marino A. F. et al., 2012, A&A, 541, A15
Marino A. F. et al., 2014, MNRAS, 442, 3044
Massari D. et al., 2014, ApJ, 795, 22
Mateo M. L., 1998, ARA&A, 36, 435
Meléndez J., Barbuy B., 2009, A&A, 497, 611
Milone A. P. et al., 2008, ApJ, 673, 241
Milone A. P., Bedin L. R., Piotto G., Anderson J., 2009, A&A, 497, 755
Milone A. P. et al., 2012a, A&A, 540, A16
Milone A. P. et al., 2012b, ApJ, 744, 58
Milone A. P. et al., 2013, ApJ, 767, 120

Milone A. P. et al., 2014, ApJ, 785, 21
Milone A. P. et al., 2015, MNRAS, 447, 927
Mishenina T. V., Kovtyukh V. V., Soubiran C., Travaglio C., Busso M., 2002, A&A, 396, 189
Monelli M. et al., 2013, MNRAS, 431, 2126
Moore B., Ghigna S., Governato F., Lake G., Quinn T., Stadel J., Tozzi P., 1999, ApJ, 524, L19
Muñoz C., Geisler D., Villanova S., 2013, MNRAS, 433, 2006
Norris J. E., Da Costa G. S., 1995, ApJ, 441, L81
Norris J. E., Freeman K. C., Mighell K. J., 1996, ApJ, 462, 241
Norris J. E., Wyse R. F. G., Gilmore G., Yong D., Frebel A., Wilkinson M. I., Belokurov V., Zucker D. B., 2010, ApJ, 723, 1632
Olszewski E. W., Saha A., Knezek P., Subramaniam A., de Boer T., Seitzer P., 2009, AJ, 138, 1570
Origlia L. et al., 2011, ApJ, 726, LL20
Pasquini L. et al., 2002, The Messenger, 110, 1
Piotto G. et al., 2012, ApJ, 760, 39
Preston G. W., Sneden C., 2001, AJ, 122, 1545
Roederer I. U., Cowan J. J., Karakas A. I., Kratz K.-L., Lugaro M., Simmerer J., Farouqi K., Sneden C., 2010, ApJ, 724, 975
Roederer I. U., Marino A. F., Sneden C., 2011, ApJ, 742, 37
Shingles L. J., Karakas A. I., Hirschi R., Fishlock C. K., Yong D., Da Costa G. S., Marino A. F., 2014, ApJ, 795, 34
Simmerer J., Sneden C., Ivans I. I., Kraft R. P., Shetrone M. D., Smith V. V., 2003, AJ, 125, 2018
Simmerer J., Sneden C., Cowan J. J., Collier J., Woolf V. M., Lawler J. E., 2004, ApJ, 617, 1091
Simmerer J., Ivans I. I., Filler D., Francois P., Charbonnel C., Monier R., James G., 2013, ApJ, 764, L7
Smette A. et al., 2015, preprint (arXiv:1501.07239)
Smith V. V., Suntzeff N. B., Cunha K., Gallino R., Busso M., Lambert D. L., Straniero O., 2000, AJ, 119, 1239
Sneden C. A., 1973, PhD thesis, The University of Texas at Austin
Sneden C., Gratton R. G., Crocker D. A., 1991, A&A, 246, 354
Sneden C., McWilliam A., Preston G. W., Cowan J. J., Burris D. L., Armosky B. J., 1996, ApJ, 467, 819
Sneden C., Pilachowski C. A., Kraft R. P., 2000, AJ, 120, 1351
Sneden C., Cowan J. J., Gallino R., 2008, ARA&A, 46, 241
Sneden C., Lawler J. E., Cowan J. J., Ivans I. I., Den Hartog E. A., 2009, ApJS, 182, 80
Stetson P. B., 2000, PASP, 112, 925
Straniero O., Cristallo S., Piersanti L., 2014, ApJ, 785, 77
Suntzeff N. B., Kraft R. P., 1996, AJ, 111, 1913
Thompson I. B. et al., 2008, ApJ, 677, 556
Travaglio C., Gallino R., Arnone E., Cowan J., Jordan F., Sneden C., 2004, ApJ, 601, 864
Villanova S., Geisler D., Piotto G., 2010, ApJ, 722, L18
Willman B. et al., 2005, ApJ, 626, L85
Willman B. et al., 2006, preprint (astro-ph/0603486)
Yong D., Grundahl F., 2008, ApJ, 672, L29
Yong D., Grundahl F., Johnson J. A., Asplund M., 2008, ApJ, 684, 1159
Yong D., Grundahl F., D'Antona F., Karakas A. I., Lattanzio J. C., Norris J. E., 2009, ApJ, 695, L62
Yong D. et al., 2013, MNRAS, 434, 3542
Yong D. et al., 2014, MNRAS, 441, 3396
Zorotovic M. et al., 2010, AJ, 139, 357
Zucker D. B. et al., 2006, ApJ, 643, L103

SUPPORTING INFORMATION

Additional Supporting Information may be found in the online version of this article:

Table 2. Coordinates, basic photometric data and RVs for the stars in the field of view of NGC 5286.
Table 3. Line list for the program stars.
Table 4. Adopted atmospheric parameters and chemical abundances derived for the NGC 5286 stars observed with GIRAFFE.
(http://mnras.oxfordjournals.org/lookup/suppl/doi:10.1093/mnras/stv420/-/DC1).

Please note: Oxford University Press is not responsible for the content or functionality of any supporting materials supplied by the authors. Any queries (other than missing material) should be directed to the corresponding author for the paper.

This paper has been typeset from a TEX/LATEX file prepared by the author.